



AD A113065

UNCLASSIFIED March 1982

SECURITY CLASSIFICATION OF THIS PAGE (When Data Entered)

REPORT DOCUMENTATION PAGE		READ INSTRUCTIONS BEFORE COMPLETING FORM
1. REPORT NUMBER WHOI-82-11	2. GOVT ACCESSION NO. AD-A113565	3. RECIPIENT'S CATALOG NUMBER
4. TITLE (and Subtitle) OBSERVATIONS OF VERTICALLY PROPAGATING EQUATORIALLY-TRAPPED WAVES IN THE DEEP WESTERN INDIAN OCEAN	5. TYPE OF REPORT & PERIOD COVERED Technical	
	6. PERFORMING ORG. REPORT NUMBER	
7. AUTHOR(s) Kathlee O'Neill	8. CONTRACT OR GRANT NUMBER(s) N00014-75-C-0700 N00014-76-C-01840 N00014-76-C-0197; NR 083-400	
9. PERFORMING ORGANIZATION NAME AND ADDRESS Woods Hole Oceanographic Institution Woods Hole, Massachusetts 02543	10. PROGRAM ELEMENT, PROJECT, TASK AREA & WORK UNIT NUMBERS NR 083-400	
11. CONTROLLING OFFICE NAME AND ADDRESS NORDA/National Space Technology Laboratory Bay St. Louis, MS 39529	12. REPORT DATE March 1982	
	13. NUMBER OF PAGES	
14. MONITORING AGENCY NAME & ADDRESS (if different from Controlling Office)	15. SECURITY CLASS. (of this report) Unclassified	
	15a. DECLASSIFICATION/DOWNGRADING SCHEDULE	
16. DISTRIBUTION STATEMENT (of this Report) Approved for public release; distribution unlimited.		
17. DISTRIBUTION STATEMENT (of the abstract entered in Block 20, if different from Report)		
18. SUPPLEMENTARY NOTES A dissertation submitted to The John Hopkins University in conformity with the requirements for the degree of Doctor of Philosophy. Partially funded by Grant from NSF, ATM76-04050-A1, ATH7604050, OCE-79-21786; for NASA with Grants NGS-5090, NSG-5161, NAS6-2706 and from ONR as listed above.		
19. KEY WORDS (Continue on reverse side if necessary and identify by block number) 1. Equatorial Indian Ocean 2. Vertically propagating waves 3. Acoustic dropsonde		
20. ABSTRACT (Continue on reverse side if necessary and identify by block number) See reverse side.		

DD FORM 1473  
1 JAN 73

EDITION OF 1 NOV 65 IS OBSOLETE  
S/N 0102-014-6601

UNCLASSIFIED March 1982  
SECURITY CLASSIFICATION OF THIS PAGE (When Data Entered)

UNCLASSIFIED MARCH 1982

*keeps*

SECURITY CLASSIFICATION OF THIS PAGE(When Data Entered)

20.

An hypothesis of equatorially-trapped waves is found to be consistent with time series of vertical profiles of horizontal velocity and CTD data from the western Indian Ocean. The profiles were collected using an acoustic dropsonde, the White Horse, along the 53°E meridian. The temporal coverage is a month-long period spanning the onset of the southwest monsoon in 1976; the latitudinal coverage is 3/4°S to 5°N.

To examine the composition of the velocity field, a WKB stretching procedure was applied to the depth and a WKB normalizing procedure to the velocity. Autospectral estimates reveal equatorial intensification that varies with vertical wavenumber. To examine vertical propagation, dropped lagged coherences have been computed. The results indicate the presence of a mixed Rossby-gravity wave of 60-77 day period with phase propagation downward at a vertical wavelength of 1200 in the stretched coordinate, which is equivalent to approximately three wavelengths between the thermocline and the bottom. Vertical propagation is indicated in other wavenumber bands as well, also corresponding to autospectral peaks.

↑

UNCLASSIFIED MARCH 1982

SECURITY CLASSIFICATION OF THIS PAGE(When Data Entered)

WHOI-82-11

OBSERVATIONS OF VERTICAL PROPAGATING EQUATORIALLY-TRAPPED  
WAVES IN THE DEEP WESTERN INDIAN OCEAN

By

Kathleen O'Neill

WOODS HOLE OCEANOGRAPHIC INSTITUTION  
Woods Hole, Massachusetts 02543

March 1982



Accession For	
NTIS GRA&I	<input checked="" type="checkbox"/>
DTIC TAB	<input type="checkbox"/>
Unannounced	<input type="checkbox"/>
Justification	
By _____	
Distribution/	
Availability Codes	
Dist	Avail and/or Special
A	

TECHNICAL REPORT

Prepared for the National Science Foundation under Grants  
ATM76--04050-A1, ATH7604050, OCE-79-21786; for NASA under  
Grants NGS-5090, NSG-5161, NAS6-2706 and for the Office of  
Naval Research under Contracts N00014-76-C-0197; NR 083-400,  
N00014-75-C-0700, N00014-76-C-01840.

Reproduction in whole or in part is permitted for any pur-  
pose of the United States Government. This report should  
be cited as: Woods Hole Oceanog. Inst. Tech. Rept. WHOI-  
82-11.

Approved for public release; distribution unlimited.

Approved for Distribution:

N.P. Fofonoff  
N.P. Fofonoff, Chairman  
Department of Physical Oceanography

Observations of Vertically Propagating  
Equatorially-Trapped Waves  
in the Deep Western Indian Ocean

By

Kathleen O'Neill

A dissertation submitted to The John Hopkins  
University in conformity with the requirements  
for the degree of Doctor of Philosophy

Baltimore, Maryland

1982

Observations of Vertically Propagating, Equatorially-trapped  
Waves in the Deep Western Indian Ocean

ABSTRACT

An hypothesis of equatorially-trapped waves is found to be consistent with time series of vertical profiles of horizontal velocity and CTD data from the western Indian Ocean. The profiles were collected using an acoustic dropsonde, the White Horse, along the 53°E meridian. The temporal coverage is a month-long period spanning the onset of the southwest monsoon in 1976; the latitudinal coverage is 3/4°S to 5°N.

To examine the composition of the velocity field, a WKB stretching procedure was applied to the depth and a WKB normalizing procedure to the velocity. An average buoyancy frequency profile was used to reduce each velocity profile to the form which would have been observed in a uniformly stratified ocean. Removal of the variations of amplitude and scale resulting from the background density stratification makes it possible to discuss vertical wavenumbers throughout the temporal and spatial array, rather than merely local vertical wavenumbers.

Autospectral estimates reveal equatorial intensification that varies with vertical wavenumber. The hypothesis is that equatorially-trapped waves of one kind or another are the basis for the observed motion. To examine vertical propagation, dropped lagged coherences have been computed. Pairs of drops separated by the same

temporal lag were grouped together to estimate cross-spectra. The results indicate the presence of a mixed Rossby-gravity wave of 60-77 day period with phase propagation downward at a vertical wavelength of 1200 in the stretched coordinate, which is equivalent to approximately three wavelengths between the thermocline and the bottom. Vertical propagation is indicated in other wavenumber bands as well, also corresponding to autospectral peaks.

If linear equatorial wave theory is applicable, zonal wavelengths can be determined from the dispersion relation, and possible forcing mechanisms can then be examined. Linear theory gives a zonal wavelength of 300-400 km for the 1200 stretched meter (sm) oscillation. The rms velocity is the same order as the phase speed, however, so that nonlinearities may not be completely negligible. Indications are of multiple processes within the same wavenumber band, a longer-period Kelvin or Rossby wave coexisting with the above-mentioned mixed Rossby-gravity wave.



## ACKNOWLEDGMENTS

I am grateful to my advisors, Owen M. Phillips at the Johns Hopkins University and James R. Luyten at the Woods Hole Oceanographic Institution, for critical guidance and encouragement. Owen Phillips allowed me to enroll at Johns Hopkins as a special student with a dream but no science background in 1975. Jim Luyten gave me the opportunity to work with his White Horse data from the 1976 Indian Ocean Expedition. Doug Luther, Charles Eriksen and Joe Pedlosky provided fruitful discussion and useful comments and witticisms during the progress of this work.

Monetary support for this research was provided in part through the Johns Hopkins University by National Science Foundation grants ATM76-04050-A1 and ATH76-04050, NASA grants NGS-5090, NSG-5161 and NAS6-2706, and Office of Naval Research contracts N00014-75-C-0700 and N00014-76-C-01840; and in part through the Woods Hole Oceanographic Institution by NSF grant OCE79-21786 and ONR contract N00014-76-C-0197, NR 083-400.

## TABLE OF CONTENTS

Abstract . . . . .	ii
Acknowledgements . . . . .	iv
List of Figures . . . . .	vii
List of Tables . . . . .	ix
 Chapter I. Organization and Theory	
A. Introduction . . . . .	1
1. Description of the data: time series of depth profiles . . . . .	1
2. Organization of dissertation . . . . .	11
B. Theory	
1. General linear equatorial wave theory and solutions . . . . .	12
a. Vertical structure equation . . . . .	13
b. Meridional structure equation . . . . .	14
2. Particular solutions and discussion . . . . .	16
a. Kelvin waves . . . . .	17
b. Mixed Rossby-gravity waves . . . . .	18
c. Rossby and inertia-gravity waves . . . . .	19
d. Symmetry and antisymmetry . . . . .	25
 Chapter II. Data Acquisition and Reduction Procedures . . . . .	
26	
A. Initial Data Processing	
1. Description of the instrument and its deployment . . . . .	26
2. Conversion of travel times to velocity components . . . . .	28
B. Calculations from the CTD Data	
1. Buoyancy frequency . . . . .	37
2. Vertical displacement . . . . .	37
C. WKB Stretching and Normalizing Procedures . . . . .	40
D. Spectral Analysis Methods . . . . .	44
1. Auto- and cross-spectra . . . . .	48
2. Dropped lagged coherence (DLC) and its interpretation . . . . .	49
 Chapter III. Zonal Velocity	
A. Latitudinal Distribution of Zonal Velocity	
1. Latitudinal energy density . . . . .	54
2. Latitudinal profile sections . . . . .	58
3. Variance-preserving net autospectra . . . . .	63
B. Relationships Between Zonal Velocity and Other Variables	
1. General cross-spectral results . . . . .	65
2. 400sm wavelength cross-spectra . . . . .	68
C. Dropped Lagged Coherence Results	
1. General . . . . .	68
2. Particular wavelength bands . . . . .	70
D. Interpretation and Examination in Terms of Linear Theory	
1. Equatorial trapping . . . . .	70
2. Evaluation of latitudinal symmetry/antisymmetry . . . . .	72

TABLE OF CONTENTS (continued)

Chapter IV. Meridional Velocity . . . . .	79
A. Latitudinal Distribution of Meridional Velocity	
1. Latitudinal energy density . . . . .	79
2. Latitudinal profile sections . . . . .	81
3. Variance-preserving net autospectra . . . . .	83
B. Relationships Between Meridional Velocity and Other Variables	
1. General cross-spectral results . . . . .	85
2. 1200sm wavelength cross-spectra . . . . .	87
3. 450sm wavelength cross-spectra . . . . .	88
C. Dropped Lagged Coherence Results	
1. General . . . . .	89
2. 1200sm wavelength . . . . .	90
3. 450sm wavelength . . . . .	94
4. 720sm wavelength . . . . .	96
D. Interpretation and Examination in Terms of Linear Theory	
1. Equatorial Trapping . . . . .	98
2. Interpretation of spectral behavior for 1200sm band . . . . .	101
3. Interpretation of spectral behavior for 450sm band . . . . .	107
Chapter V. Conclusion . . . . .	111
Appendix A. Latitudinal Profile Transects . . . . .	120
Appendix B. Temporal Series at Each Profiling Station . . . . .	138
Appendix C. Tables of Cross-spectral Coherence and Phase . . . . .	153
References . . . . .	158
Vita . . . . .	161

## List of Figures

I-1.	Bathymetric map of western equatorial Indian Ocean . . . . .	3
I-2.	Cruise track of Atlantis-II . . . . .	4
I-3.	1976 White Horse velocity profiles presented in isometric projection . . . . .	5
I-4.	Original velocity component profiles at 0°, 53°E . . . . .	7
I-5.	Same velocity profiles as I-4 after WKB stretching and normalizing . . . . .	9
I-6.	Dispersion relation plotted in zonal wavenumber-frequency space for a vertical wavelength of 1200sm . . . . .	22
II-1.	Photograph of White Horse on crane, prior to launch . . . . .	27
II-2.	Transponder survey pattern and network layout . . . . .	31
II-3.	White Horse profile # 607 in plan view . . . . .	33
II-4.	Plot of average buoyancy frequency profile against depth . . . . .	38
II-5.	Illustration of calculation of vertical isopycnal displacement . . . . .	40
II-6.	Example of displacement profiles, from 0°, 53°N . . . . .	41
II-7.	Plot of z versus z*, illustrating WKB mapping . . . . .	45
II-8.	Examples of profiles along latitudinal transect #4, a) original profiles . . . . .	46
	b) stretched and normalized profiles . . . . .	47
II-9.	Idealized representations of models for dropped lagged coherence interpretation . . . . .	51
III-1.	Autospectral estimates by latitude, averaged over five wavenumber bands: a) $u^*$ . . . . .	55
	b) $\zeta^*$ . . . . .	57

List of Figures (continued)

III-2.	Zonal velocity and vertical displacement profiles from latitudinal transect #3: a) original form . . . . .	59
	b) stretched and normalized . . . . .	60
III-3.	Variance-preserving autospectral estimates for $u^*$ , by net .	64
III-4.	Superposition of dropped lagged coherence and phase for all temporal lags resolvable at $0^\circ, 53^\circ E$ , for $u^*$ . . . . .	69
III-5.	Zonal and meridional DLC for 400sm at $0^\circ$ and $3/4^\circ N$ , $53^\circ E$ .	71
III-6.	Comparison of pairs of zonal velocity profiles from the equator, $50^\circ 30' E$ and $53^\circ E$ . . . . .	76
IV-1.	Autospectral estimates of $v^*$ by latitude, averaged over five vertical wavenumber bands . . . . .	80
IV-2.	Meridional velocity profiles from latitudinal transect #4, presented in original form and after WKB stretching and normalizing . . . . .	82
IV-3.	Variance-preserving autospectral estimates for $v^*$ , by net .	84
IV-4.	Superposition of dropped lagged coherence and phase for all temporal lags resolvable at $0^\circ, 53^\circ E$ , for $v^*$ . . . . .	91
IV-5.	Zonal and meridional DLC for 1200sm at $0^\circ$ and $3/4^\circ N$ , $53^\circ E$ .	92
IV-6.	Same as Figure IV-5, for 450sm wavelength band . . . . .	95
IV-7.	Same as Figure IV-5, for 720sm wavelength band . . . . .	97
IV-8.	Comparison of pairs of meridional velocity profiles from the equator, $50^\circ 30' E$ and $53^\circ E$ . . . . .	108

## List of Tables

I-1.	Equivalent depth, separation constant, equatorial Rossby radius of deformation, and characteristic time scale for vertical wavelengths resolvable from these observations . .	20
I-2.	Range of periods by vertical wavelength where only Kelvin and mixed Rossby-gravity waves can exist, from linear theory, i.e., maximum inertia-gravity periods, minimum Rossby periods . . . . .	21
II-1.	Transponder net survey data: location, date, net coordinates (m), absolute orientation of net baseline, indicated as degrees of clockwise rotation to align net east-west, horizontal dimensions of net (km) . . . . .	29
II-2.	Summary of information about each profile . . . . .	34
III-1.	Quantification of symmetry/antisymmetry of zonal velocity profiles with latitude . . . . .	62
III-2.	Coherence and phase for all three variables, by vertical wavenumber . . . . .	67
III-3.	Equatorial trapping scales for particular wavelength bands, for the zonal kinetic energy estimates . . . . .	72
III-4.	Theoretical structure of first meridional mode long Rossby wave, for comparison to data . . . . .	75
IV-1.	Same as Figure III-2 . . . . .	86
IV-2.	Equatorial trapping scales for particular wavelength bands, for the meridional kinetic energy estimates . . . . .	99
IV-3.	Cross-spectra between velocity components at 0° and 3/4°N, 53°E, presented as a function of time . . . . .	104

## Chapter I. Introduction and Theory

### Section A. Introduction

A unique set of data was collected during May and June of 1976: vertical profiles of horizontal velocity between the surface and the bottom of the western equatorial Indian Ocean. The discovery that the equatorial current structure was energetic to great depths was the initial result from these observations. Instead of merely adding to our knowledge of the generation and temporal structure of the undercurrent in the Indian Ocean, Luyten and Swallow (1976) documented the first evidence of deep vertical structure in both horizontal velocity components. Previous observations at the equator had indicated that the zonal velocity field had variability below the undercurrent, but profile measurements had only penetrated to a maximum depth of 1500m (Rual, 1969). The type of measurement, i.e., direct and to the bottom, possible with the White Horse, a freely falling acoustic dropsonde developed at Woods Hole, represented a technological and logistical breakthrough.

A.1. Brief description of the data. The White Horse was deployed forty-one times at seven stations in the region between 50°30'E and 53°E, 3/4°S and 5°N. The data collected were unique in that they provided the first detailed snapshots of the equatorial water column and because of the complex vertical structure they revealed. They remain unique because, although the instrument and others resembling it have been used since then, there is still no comparable time series, in

quality and in latitudinal coverage over time.

Figure I-1 shows the location of the profiling stations. The three-dimensional position of the instrument was determined approximately every twenty meters of depth, in a manner described below, and horizontal velocities were calculated from the positions. The resulting vertical profiles of horizontal velocity between the surface and the bottom are non-uniformly separated in time. (See Figure I-2, ship's track.)

Figure I-3 displays most of the velocity data. The drops were primarily along the 53°E meridian, and ranged latitudinally from 3/4°S to 5°N. The temporal coverage is from May 14 to June 18, 1976. The longest time series at a single location is at the equator, with ten profiles at 0°, 53°E. The figure shows perspective plots of the velocity vectors from the surface to the bottom, and reveals that the vertical structure is complex at the equator and becomes simpler away from it. The velocity vectors rotate with depth, but not with any regularity.

Part of the instrumentation package of the White Horse is a Neil Brown conductivity, temperature and depth recorder (CTD), so concurrent density profiles were taken from the surface to the bottom. The profiler data are supplemented with data from current meters and temperature/pressure recorders, moored in the same region where the White Horse was deployed. Additional data were collected during two INDEX cruises in the spring and summer of 1979. Reference to results from those experiments will be made where appropriate.



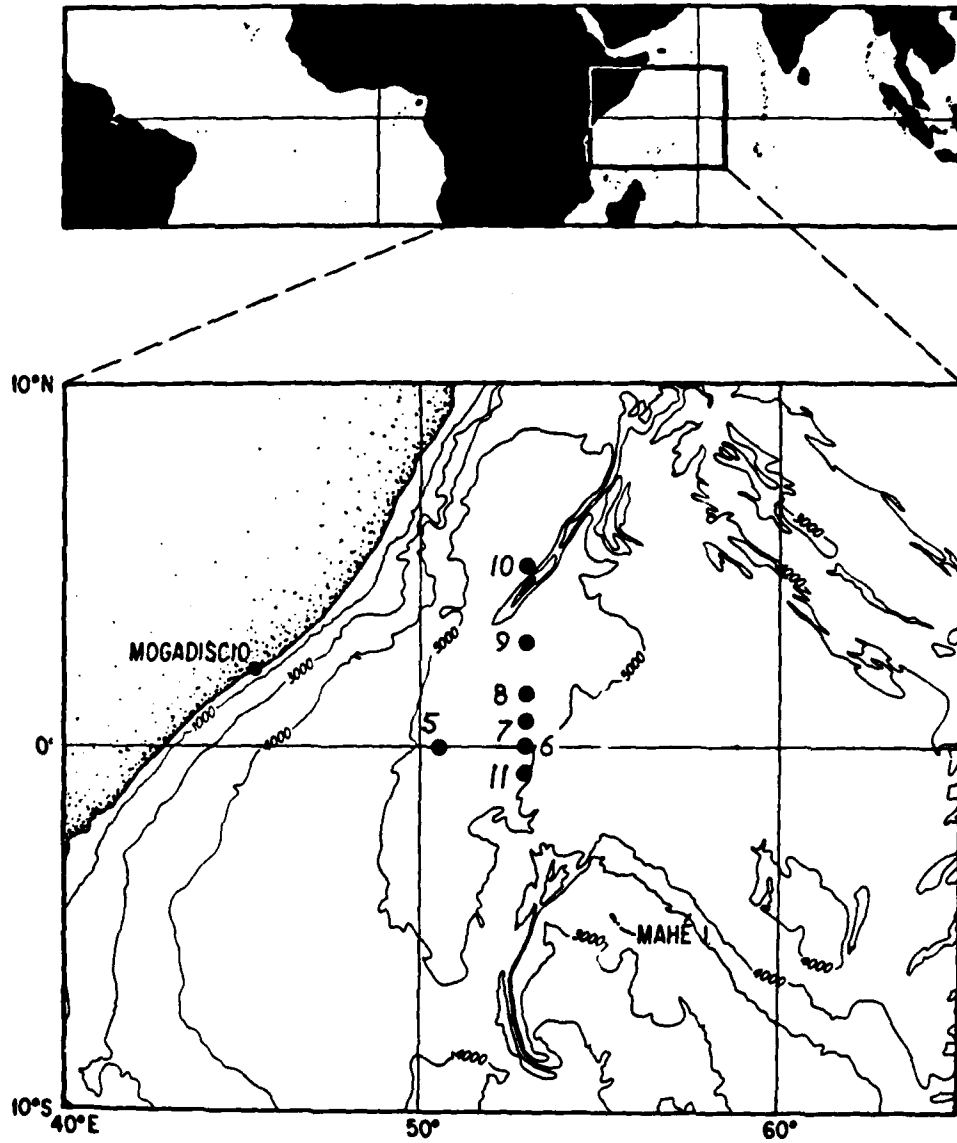


FIGURE I-1

Bathymetric map of western equatorial Indian Ocean, showing location of 1976 White Horse profiling stations.

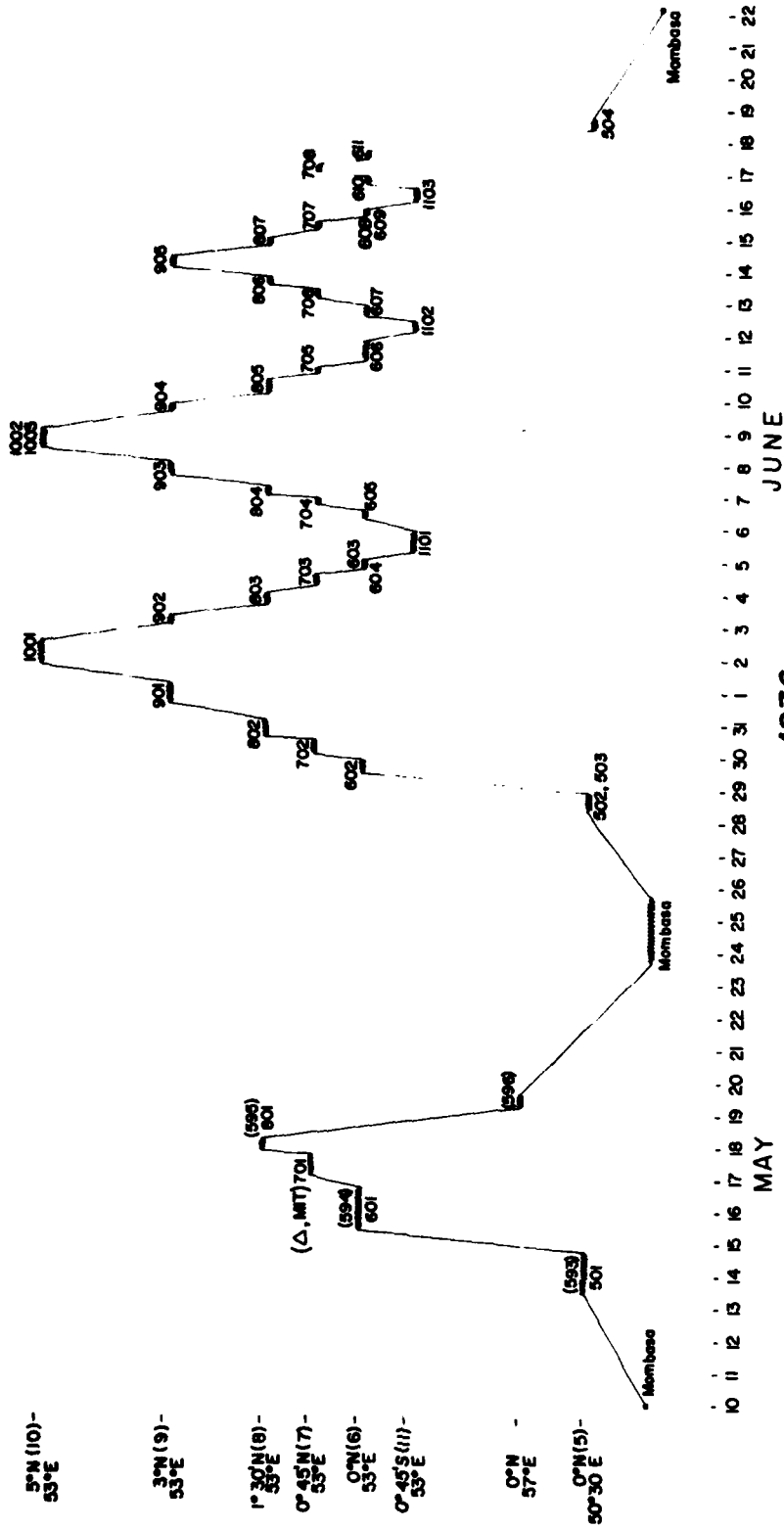


FIGURE I-2

Cruise track of Atlantis-II in May and June of 1976. Ordinate indicates latitude (and the longitudinal exception, net 5 at 50°30'E), and White Horse profile stations are labelled with the net number followed by two sequential digits.

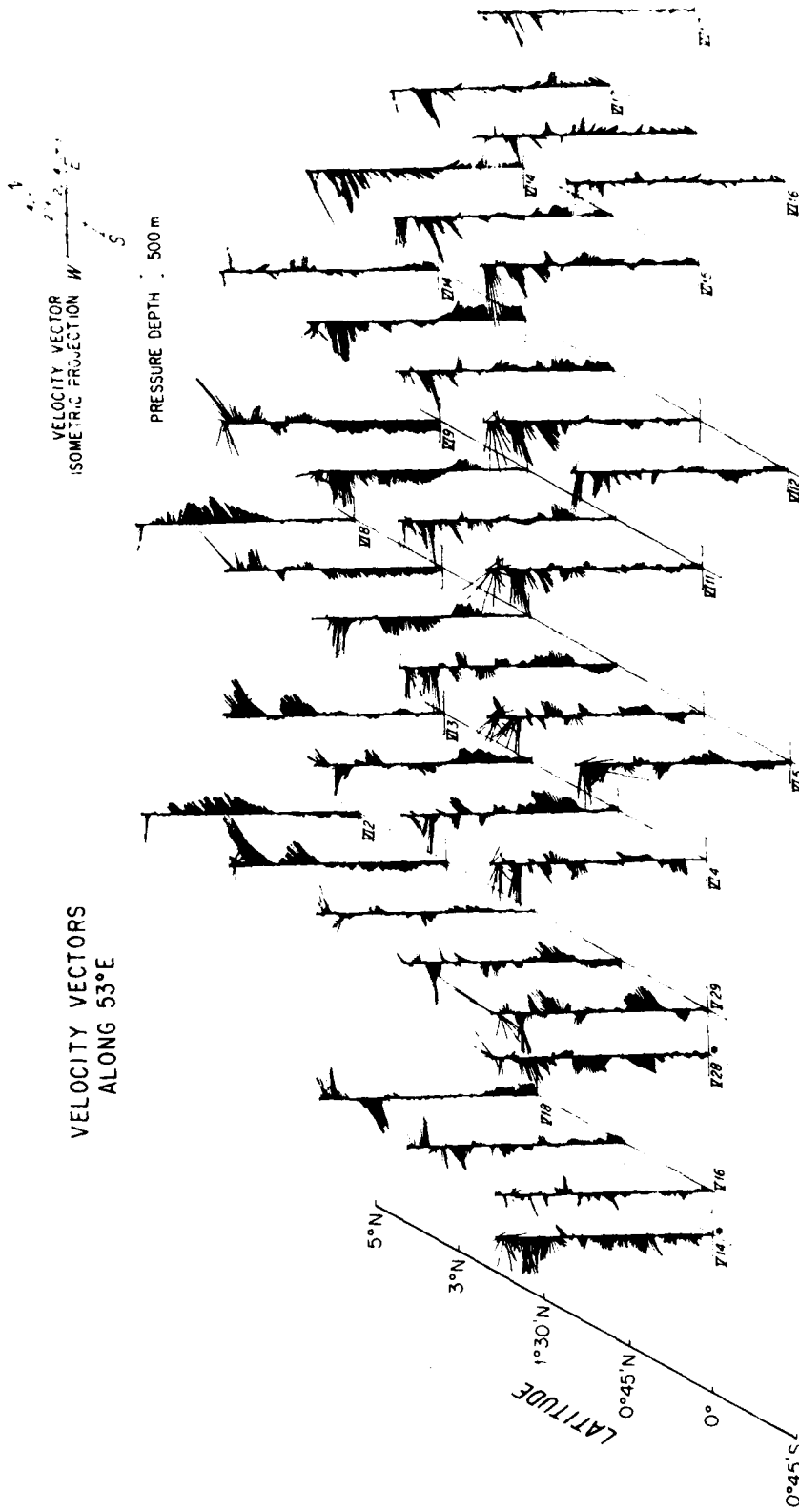
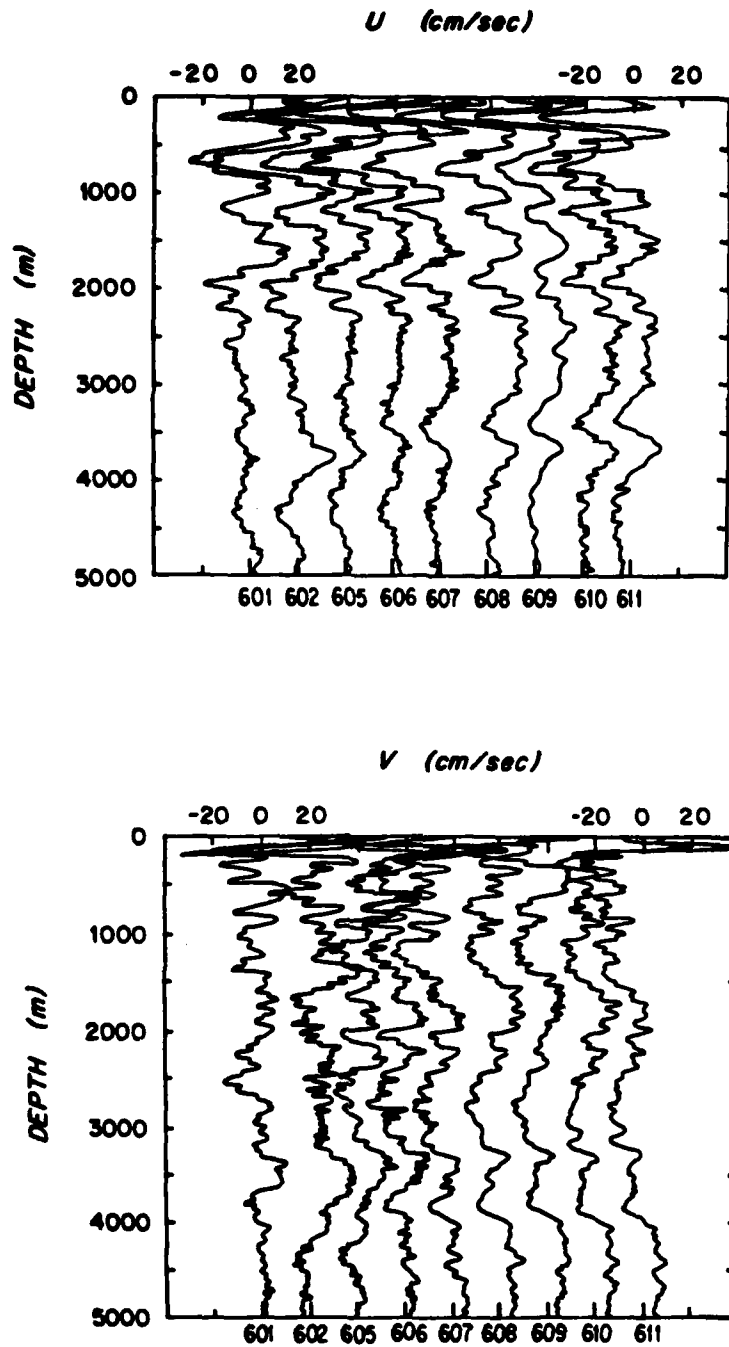


FIGURE I-3  
 White Horse profiles presented as three-dimensional perspective plots of the velocity vector from the surface to the bottom. Latitude is indicated on the lefthand portion of the figure.

Several features are obvious in the data. The vertical structure of the velocity field at the equator is complex, whereas the vertical structure at 5°N is similar to a first baroclinic mode, i.e., the complex vertical structure is equatorially confined. The large scale structures in the zonal velocity profiles persist with time, indicating that long-period processes dominate the east-west component. The velocity components,  $u$  and  $v$ , are of the same order, rather than being overwhelmingly zonal, as was found in the western Pacific, for example (Eriksen, 1981). A dominance of clockwise or counterclockwise rotation occurs in bands, and is not uniform from the surface to the bottom.

When the velocity profiles are examined in component form, rather than in the vector form shown in Figure I-3, a dichotomy can be seen in both the vertical and the temporal scales of the motion. The meridional component displays shorter scales in both dimensions. Figure I-4a shows the east-west velocity component at the equator in original form. Time is increasing to the right. The first impression is one of a wavy structure, with higher amplitudes and shorter vertical scales in the upper part of the water column. The same pattern holds for the meridional component (Figure I-4b). A background dependence upon the buoyancy frequency, which is indicated very clearly in the current meter analysis done by Luyten (1982), seems to be affecting both velocity amplitudes and vertical length scales.

In an attempt to remove this background dependence and to reduce each velocity profile to the form which might have been observed in a



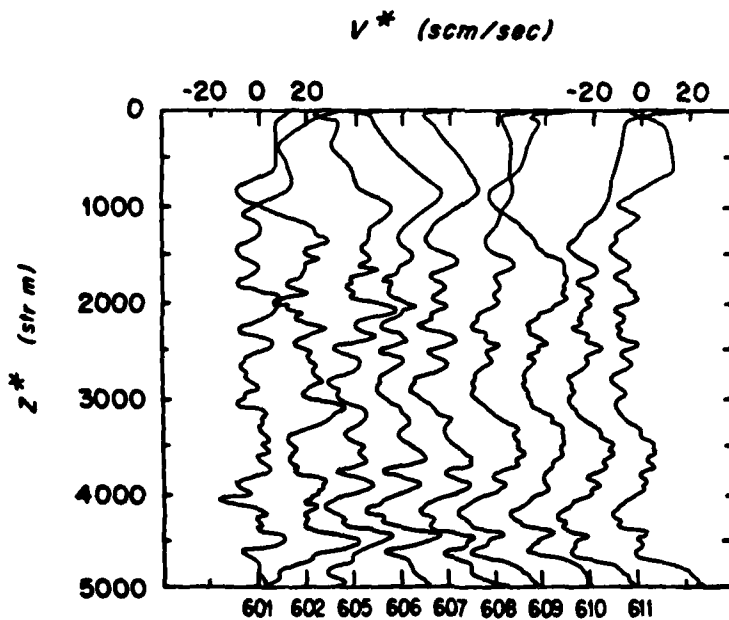
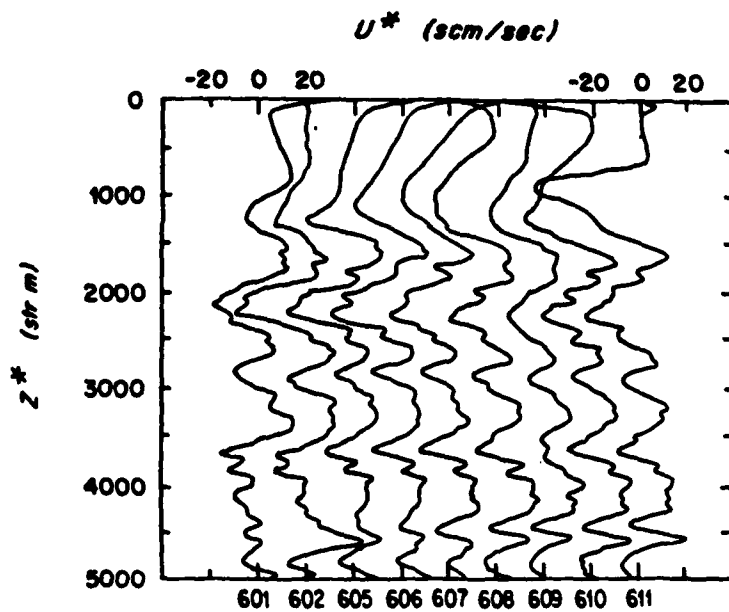
BEFORE

FIGURE I-4

Zonal (a) and meridional (b) velocity profiles at the equator, 53°E. Time increases to the right, but the spacing between profiles is not adjusted for the actual time interval between them.

uniformly stratified ocean, the average buoyancy frequency profile was used to scale both velocity and depth. The "after" picture in Figure I-5 shows the  $u$ - and  $v$ -components after this WKB stretching and normalizing procedure. These are relabelled  $u^*$  and  $v^*$ , and plotted against  $z^*$ . The oscillations are much more uniform, except in the top 1400 scaled meters, which correspond to the top 275m of the ocean. The upper portion of the water column will in general not be considered in the following analysis.

One can now discuss vertical wavenumbers throughout the temporal and spatial array rather than merely local vertical wavenumbers. The data in this form are the inputs to the spectral analysis discussed in Chapter II-C and D and interpreted in Chapters III and IV. Variations of the cross-spectra computed from the profiles at a particular vertical wavenumber should then depend only on the time differences between profiles. An analysis can be done using all coverings separated by the same time lag. [Hayes (1975) analyzed temperature profiles in this fashion.] For each temporal lag considered, coherence and phase can be examined as a function of vertical wavenumber,  $m$ . One can expect coherence to drop as  $m$  increases, since the data collection method operates as a low-pass filter by averaging the velocity vector over 20-second intervals (Hendricks and Rodenbusch, 1981), and since smaller wavelengths should be less correlated as the band-width increases (Munk and Phillips, 1968). The coincidence of zero phase with strong coherence would indicate no phase propagation at that wavenumber. Phase change for a particular wavenumber with longer



AFTER

FIGURE I-5

The same zonal (a) and meridional (b) velocity profiles as in Figure I-4, after a WKB stretching and normalizing procedure was applied.

temporal lags, from which vertical propagation can be inferred, is discussed in Chapter II-D.2.

The purpose of this dissertation is to examine observations of long-period motion in the equatorial zone and to infer from these observations the governing dynamics. The primary emphasis will be on analysis of the profiling data. The hypothesis is that long-period equatorially-trapped waves of one kind or another are the basis for the observed motion. There is a presumption against the existence of vertical modes, based on the arguments of Wunsch (1977), summarized as follows. Theoretically, a wave of long period propagates energy from the surface at only a shallow angle to the horizontal and would take several years to reach the ocean floor. Dissipation would substantially reduce the energy of the wave before normal modes could be set up, even if the wave were perfectly reflected from the bottom and from meridional boundaries. On the other hand, vertical propagation is not visually evident. If there were a dominant semi-annual signal, for example, a  $60^\circ$  phase change could be observed over the month-long time domain involved, yet this is not the case.

It is possible to imagine generation mechanisms for the White Horse profiles other than vertically-propagating linear equatorial waves, but one feature of the data that must be explained is equatorial intensification, a highly characteristic feature of such waves. Any discrepancies between linear theory and observations which have been clearly and accurately identified are pursued as far as possible here and will motivate further theoretical research.



A.2. Organization. The basic approach outlined above leads to the following structure for the dissertation. The remainder of Chapter I presents a review of linear equatorial wave theory. Chapter II describes the methods used in analyzing the data, and presents some interpretative guidelines. Because of their differences in dominant frequencies and vertical wavenumbers, the velocity components are handled in separate chapters. Chapter III presents the results from analysis of the zonal velocity component, Chapter IV the meridional. Chapter V contains a comparison with other results and recapitulates the primary conclusions from this research.

## Section B. Linear Equatorial Wave Theory - Review

B.1. General linear theory and solutions. The linear Boussinesq equations for inviscid, incompressible, unforced rotating flow on an unbounded equatorial beta-plane are:

$$u_t - \beta y v = -p_x \quad (1a)$$

$$v_t + \beta y u = -p_y \quad (1b)$$

$$0 = -p_z - \frac{g \rho'}{\rho_0} \quad (1c)$$

$$\rho'_t + w \bar{\rho}_z = 0 \quad (1d)$$

$$u_x + v_y + w_z = 0 \quad (1e)$$

where the subscript denotes differentiation,  $p$  is reduced perturbation pressure ( $p = p' \rho_0$ ), and  $\hat{\rho} = \bar{\rho} + \rho'$ ;  $\rho_0$  is the constant reference density and  $\hat{\rho}$  is the observed density field, composed of mean ( $\bar{\rho}$ ) and fluctuating ( $\rho'$ ) components. By cross-differentiation and using  $N^2 = -\frac{g}{\rho_0} \frac{\partial \bar{\rho}}{\partial z}$ , equations 1c and 1d reduce to  $p_{zt} + N^2 w = 0$ .

Following the notation of Eriksen (1982), let

$$\begin{bmatrix} u \\ v \\ p \\ w \end{bmatrix} = A_{nm} e^{i(kx - \omega t)} \begin{bmatrix} U_n(y/y_m^*) G_m'(z) \\ i V_n(y/y_m^*) G_m'(z) \\ c_m P_n(y/y_m^*) G_m'(z) \\ -\omega c_m^{-1} P_n(y/y_m^*) G_m(z) \\ c_m^{-1} P_n(y/y_m^*) G_m(z) \end{bmatrix} \quad (2)$$

where  $c_m = \sqrt{gh_m}$  [ $= N_0 / |m|$ ] is a separation constant, with units of

speed;  $h_m$  is defined as the equivalent depth;  $N_0$  is a reference buoyancy frequency;  $y_m^* = [c_m/\beta]^{1/2}$  is a characteristic meridional length scale, the equatorial radius of deformation; and  $\int$  is the vertical displacement of isopycnals, measured upward (see Chapter II-B for derivation from the conservation of mass equation, Equation-1d). The dependent variables are assumed to be simply periodic in  $x$  and  $t$ , and some as-yet-undefined functions of  $y$  [ $U_n, V_n$  or  $P_n(y/y^*)$ ] and  $z$  [ $G$  or  $G'(z)$ ].

B.1.a. Vertical structure equation. The equations are separable, and reduce to a vertical and a meridional structure equation. The horizontal structure equation is similar to that derived in shallow water wave theory from the Laplace Tidal Equations, where here the depth parameter is  $h_m$  ( $\equiv$  equivalent depth) rather than  $H$  (= total water depth). The vertical structure equation is

$$G_{zz} + \frac{N^2(z)G}{c_m^2} = 0, \quad (3)$$

which admits first-order WKB solutions of the form

$$G(z) \approx \frac{1}{\left[\frac{N}{c_m}\right]^{1/2}} \exp(\pm i \int \frac{N}{c_m} dz),$$

where  $\bar{N}(z)/c_m = |m|$  is the local vertical wavenumber (Philander, 1978) and the choice of sign depends upon the direction of propagation [plus (minus) indicates phase propagation upward (downward)]. If we let  $m^* = N_0/c_m$  then the approximate solution becomes

$$G(z) \approx \frac{1}{|m^*|^{1/2}} \left\{ \frac{N_0}{N(z)} \right\}^{1/2} \exp(\text{sgn } m^* i \int |m^*| \frac{N(z)}{N_0} dz). \quad (4)$$

A new variable  $z^*$  can then be defined:

$$dz^* = \bar{N}(z)/N_0 dz.$$

Thus 
$$z^* = \int \bar{N}(z)/N_0 dz$$

and 
$$G(z) = [N_0/\bar{N}(z)]^{1/2} G(z^*);$$

$$G'(z) = \text{sgn } m [\bar{N}(z)/N_0]^{1/2} G'(z^*).$$

Thus  $u, v, p \propto [\bar{N}(z)/N_0]^{1/2} G'(z^*); w, \zeta \propto [N_0/\bar{N}(z)]^{1/2} G(z^*).$  (5)

The WKB-scaled variables are:

$$\begin{bmatrix} u^* \\ v^* \\ p^* \end{bmatrix} = \begin{bmatrix} N_0 \\ \bar{N}(z) \end{bmatrix}^{1/2} \begin{bmatrix} u \\ v \\ p \end{bmatrix} \quad \begin{array}{l} \text{WKB} \\ \text{Scaling} \end{array} \quad (6a)$$

and

$$\begin{bmatrix} w^* \\ \zeta^* \end{bmatrix} = \begin{bmatrix} \bar{N}(z) \\ N_0 \end{bmatrix}^{1/2} \begin{bmatrix} w \\ \zeta \end{bmatrix}, \quad (6b)$$

with a scaled vertical wavenumber  $|m^*(z^*)| = N_0/\sqrt{gh_m}$ , which is no longer dependent upon the local buoyancy frequency, but only upon the reference (scaling) buoyancy frequency. The asterisk will hereinafter be dropped from  $m^*$  but retained for all the other variables.

B.1.b. Meridional structure equation. The meridional structure equation is

$$v_{n_{yy}} + \left[ \frac{\omega^2}{gh_m} - k^2 - \frac{\beta k}{\omega} - \frac{\beta^2 y^2}{gh_m} \right] v_n = 0, \quad (7)$$

a form of Weber's equation. For  $h_m > 0$ , its solutions are bounded at infinity if and only if

$$\left[ \frac{\omega^2}{gh_m} - k^2 - \frac{\beta k}{\omega} \right] = \frac{\beta}{\sqrt{gh_m}} (2n + 1), \quad (8)$$

where  $n = 0, 1, 2, \dots$ . A "turning latitude",  $y_T$ , can then be defined, where the form of the equation changes from elliptic, with oscillatory solutions, to hyperbolic, with solutions which decay exponentially poleward.

$$y_T^2 = \frac{\sqrt{gh_m}}{\beta} (2n + 1) . \quad (9)$$

This critical latitude will be discussed qualitatively later, with respect to particular meridional modes.

With the transformation of variables above, the dispersion relation (Equation-I-8) can be expressed as a function of vertical wavenumber:

$$\frac{m^2 \omega^2}{N_0^2} - k^2 - \frac{\beta k}{\omega} = \frac{\beta |m|}{N_0} (2n + 1) , \quad (10)$$

and the turning latitude is inversely proportional to the square root of the vertical wavenumber:

$$y_T = \left[ \frac{(2n+1)N_0}{|m|\beta} \right]^{1/2} . \quad (11)$$

The meridional structure equation reduces to canonical form with any of the equivalent substitutions:

$$n = \left[ \frac{\beta}{c_m} \right]^{1/2} y = \left[ \frac{\beta}{\sqrt{gh_m}} \right]^{1/2} y = \left[ \frac{\beta |m|}{N_0} \right]^{1/2} y = y/y^* ,$$

where  $y^* = \left[ \frac{N_0}{\beta |m|} \right]^{1/2}$  is the characteristic meridional length scale, also known as the equatorial Rossby radius of deformation. Its solutions are Hermite functions:

$$\begin{aligned}
 V_n(y/y^*) &= A_n \psi_n(y/y^*) \\
 &= A_n \frac{\exp(-y^2/2y^{*2}) H_n(y/y^*)}{(2^n \cdot n! \cdot \pi^{1/2})^{1/2}}, \quad (12)
 \end{aligned}$$

where  $H_n(y/y^*)$  are the Hermite polynomials of order  $n$ . [ $H_0=1$ ,  $H_1=2n$ ,  $H_2=4n^2-2$ ,  $H_3=8n^3-12n$ , ....] The Hermite functions form a complete orthogonal set, and with the above normalization factor,

$$\int_{-\infty}^{\infty} \psi_m \psi_n \, d\eta = \delta_{mn}, \quad \text{the Kronecker delta.}$$

The corresponding solutions for  $U_n$  and  $P_n$ , after substitution into the original set of equations (I-1), are:

$$U_n(y/y^*) = A_n \left[ -\frac{\left(\frac{n}{2}\right)^{1/2} \psi_{n-1}}{\sigma + s} - \frac{\left(\frac{n+1}{2}\right)^{1/2} \psi_{n+1}}{\sigma - s} \right], \quad (13a)$$

$$P_n(y/y^*) = A_n \left[ \frac{\left(\frac{n}{2}\right)^{1/2} \psi_{n-1}}{\sigma + s} - \frac{\left(\frac{n+1}{2}\right)^{1/2} \psi_{n+1}}{\sigma - s} \right], \quad (13b)$$

where, for simplicity of presentation, the meridional structure equation has been non-dimensionalized using  $\sigma = \frac{\omega}{(\beta c_m)^{1/2}}$  and  $s = \left[ \frac{c_m}{\beta} \right]^{1/2} k$ .

as well as  $\eta = y/y^* = \left[ \frac{\beta |m|}{N_0} \right]^{1/2} y$ , to reduce it to a canonical form:

$$V_{nn} + \left[ \sigma^2 - s^2 - \frac{s}{\sigma} - \eta^2 \right] V = 0. \quad (14)$$

B.2. Particular solutions and discussion. The solutions to this equation are of three types, each corresponding to a root of the cubic equation for frequency, the dispersion relation (I-10). These solutions will be discussed following development of a fourth type of solution to

equation (I-1).

B.2.a. Kelvin waves. An equatorially-trapped wave type which does not arise directly out of the above analysis (since  $V = 0$ ), is the Kelvin wave. By convention, it is ascribed a meridional mode number of -1, since for  $n = -1$ ,

$$k = \frac{\omega}{\sqrt{gh_m}} = \frac{\omega |m|}{N_0} \text{ is a solution to the dispersion relation. The}$$

particular wave solutions for the Kelvin wave are

$$U_{-1}(y/y^*) = P_{-1}(y/y^*) = A_{-1} \frac{e^{-y^2/2y^{*2}}}{\pi^{1/4}}$$

so that

$$u_{-1}(x, y/y^*, z, t) = c_m^{-1} P_{-1}(x, y/y^*, z, t)$$

and

$$\begin{aligned} \int_{-1}(x, y/y^*, z, t) &= c_m^{-1} P_{-1}(x, y/y^*, t) G(z) \\ &= c_m^{-1} \left[ \frac{-i}{m} \right] P_{-1}(x, y/y^*, z, t) \\ &= -i m^{-1} u_{-1}(x, y/y^*, z, t) . \end{aligned}$$

The meridional structures of the  $u$  and  $p$  fields are Gaussian in latitude, identical except for an amplitude factor. The displacement field is in quadrature with both of them, leading  $u$  by  $\pi/2$  with depth. The Kelvin wave zonal phase velocity ( $\omega/k$ ) is thus  $c_m = \sqrt{gh_m} = N_0/|m|$ , directed toward the east, and exactly equal to the zonal group velocity ( $\partial\omega/\partial k$ ). The vertical phase velocity ( $\omega/m$ ) depends directly upon the sign of the vertical wavenumber (upward if  $m > 0$ ). Vertical group velocity is equal in magnitude and opposite in sign to the phase velocity.

B.2.b. Mixed Rossby-gravity waves. When  $n = 0$ , the dispersion relation (I-10) can be factored. The solution for which the associated zonal velocity field is not singular is

$$k = \frac{\omega |m|}{N_0} - \frac{\beta}{\omega}. \quad (15)$$

The wave behaves as a gravity wave at high frequencies and as a Rossby wave at low frequencies, and consequently is known as a mixed Rossby-gravity wave (or, by meteorologists, sometimes called a Yanai wave). The particular wave solutions are

$$\begin{aligned} v_0 &= A_0 \psi_0 = \frac{A_0}{\pi^{1/4}} \exp(-y^2/2y_*^2) . \\ u_0 &= p_0 = -\frac{A_0}{\sqrt{2}} \frac{1}{\sigma-s} \\ &= -\frac{A_0}{\pi^{1/4}} \exp(-y^2/2y_*^2) \frac{\omega y |m|}{N_0} . \end{aligned}$$

The zonal/meridional kinetic energy ratio at a given latitude is thus  $u_0^2/v_0^2 = \frac{\omega^2 y_*^2 m^2}{N_0^2}$ . The zonal phase velocity is given by  $\omega^2 N_0 / (\omega^2 |m| - \beta N_0)$ , directed toward the west at low frequencies, toward the east at high frequencies. The zonal group velocity is slower, and always directed to the east:  $\omega^2 N_0 / (\omega^2 |m| + \beta N_0)$ . The direction of the vertical phase velocity is dependent upon the sign of the vertical wavenumber:  $(\text{sgn } m) \omega^3 / (k N_0 \omega + \beta N_0)$ . The vertical group velocity is slower and in the opposite direction:  $(-\text{sgn } m) \omega^3 / (\omega^2 |m| + \beta N_0)$ .

The ratio of zonal to vertical group velocity is easily seen to be  $(-\text{sgn } m) N_0 / \omega$ , for both the Kelvin and the mixed waves. Since the



frequencies of particular interest in the equatorial oceans are always much less than  $N_0$  ( $\sim$  one cycle per hour), the ratio indicates that the path along which energy propagates for these equatorially-trapped waves will always be at only a shallow angle to the horizontal, shallower for longer periods.

The characteristic meridional scale, or  $L_R$ , the equatorial Rossby radius of deformation, defines the e-folding distance from the equator for the kinetic energy in the zonal velocity component of a Kelvin wave and for the meridional component of a mixed Rossby-gravity wave. Note, from Table I-1, that  $L_R$  is less than the distance between the equator and the nearest off-equatorial profiling station ( $3/4^\circ$ N or S) for vertical wavelengths shorter than 514 stretched meters, so that the meridional structure at such wavelengths will be more difficult to observe with the data analyzed here.

B.2.c. Rossby and inertia-gravity waves. There are two classes of equatorially-trapped waves for meridional mode numbers equal to 1 or larger, separated by a frequency range which can be filled only by the Kelvin and mixed waves discussed above. At low frequencies ( $\sigma < 1$ ), these are the planetary or Rossby waves; at high frequencies ( $\sigma > 1$ ), these are the inertia-gravity waves (similar to mid-latitude internal gravity waves but trapped by the beta-effect to the equator). The minimum period at which Rossby waves of specific vertical wavelengths can exist, and the corresponding maximum for inertia-gravity waves, can be determined from the dispersion relation (I-10), by solving for the

TABLE I-1

$\lambda_{z^*}$ (sm)	$m = \frac{2\pi}{\lambda_{z^*}}$ (sm) <sup>-1</sup>	$h_m = \frac{N_0^2}{m^2 g}$ (cm)	$c_m = \sqrt{gh_m}$ (cm/sec)	Length Scale	Time Scale
				$[s = 2\pi] L_R$ (km)	$[\sigma = 2\pi] T$ (days)
3600	1.7 x 10 <sup>-3</sup>	12.18	109	218	2.3
1800		3.04	55	154	3.3
1200	5.2 x 10 <sup>-3</sup>	1.35	36	126	4.0
900	7.0	.76	27	109	4.6
720	8.7	.49	22	98	5.2
600	1.0 x 10 <sup>-2</sup>	.34	18	89	5.7
514		.25	16	83	6.1
450	1.4	.19	14	77	6.5
400	1.6	.15	12	73	6.9
360		.12	11	69	7.3
327		.10	10	66	7.7
300	2.1	.08	9	63	8.0
277				61	8.3
257				58	8.7
240	2.6	.05	7	56	9.0
225				55	9.3
212				53	9.5
200	3.1 x 10 <sup>-2</sup>	.04	6	51	9.8

$$L_R = \left[ \frac{c_m}{\beta} \right]^{1/2} = \left[ \frac{gh_m}{\beta} \right]^{1/2} = \left[ \frac{N_0}{|m|\beta} \right]^{1/2} = (13.24579 \times \lambda_z [m])^{1/2} \text{ km}$$

$$h_m = \frac{c_m^2}{g} = \frac{N_0^2}{m^2 g} = (.93988 \times \lambda_z^2 [km]) \text{ cm}$$

$$T = \left[ \frac{1}{c_m \beta} \right]^{1/2} = \left[ \frac{|m|}{N_0} \right]^{1/2} = \frac{L_R}{c_m}$$

$$\begin{aligned} N_0 &= 1.091464 \text{ cph} \\ &= 26.195 \text{ cpd} \\ &= 164.6 \text{ d}^{-1} \\ &= 1.9049 \times 10^{-3} \text{ s}^{-1} \end{aligned}$$

$$g_0 = 978 \text{ cm sec}^{-2}$$

$$\begin{aligned} \beta_0 &= 2.289 \times 10^{-3} \text{ cm}^{-1} \text{ s}^{-1} \\ &= 1.9777 \times 10^{-6} \text{ m}^{-1} \text{ d}^{-1} \end{aligned}$$

zonal wavenumber and examining the term enclosed under the radical:

$$k = -\frac{\beta}{2\omega} \pm \left[ \frac{\beta^2}{4\omega^2} - \frac{\beta |m|}{N_0} (2n+1) + \frac{m^2 \omega^2}{N_0^2} \right]^{1/2}. \quad (16)$$

For  $n=1$ , the two values of  $\omega$  which make the expression in brackets equal to zero can be determined:

$$\omega = \left\{ \begin{array}{l} 1.707 \\ .293 \end{array} \right\} \left[ \frac{N_0 \beta}{|m|} \right]^{1/2}.$$

The upper factor defines the maximum inertia-gravity wave period (for the first meridional mode); the lower defines the minimum period for the first mode Rossby wave.

TABLE I-2

	<u>Period (days) for the first meridional mode</u>									
Wavelength(sm)	3600	1800	1200	900	720	600	514	450	400	360
Rosby $T_{\min}$	50	70	86	100	111	122	132	141	150	157
Inertia-gravity $T_{\max}$	9	12	15	17	19	21	23	24	26	27

These maximum and minimum periods are shown in Figure I-6 (connected by a dotted line), where the dispersion relation for  $\lambda_z = 1200\text{sm}$  is plotted as a function of frequency and zonal wavelength. The dotted line is defined by:

$$k = -\frac{\beta}{2\omega},$$

which is where the zonal group velocity is exactly zero (since the term under the radical in Equation I-16 is identically zero). The curves

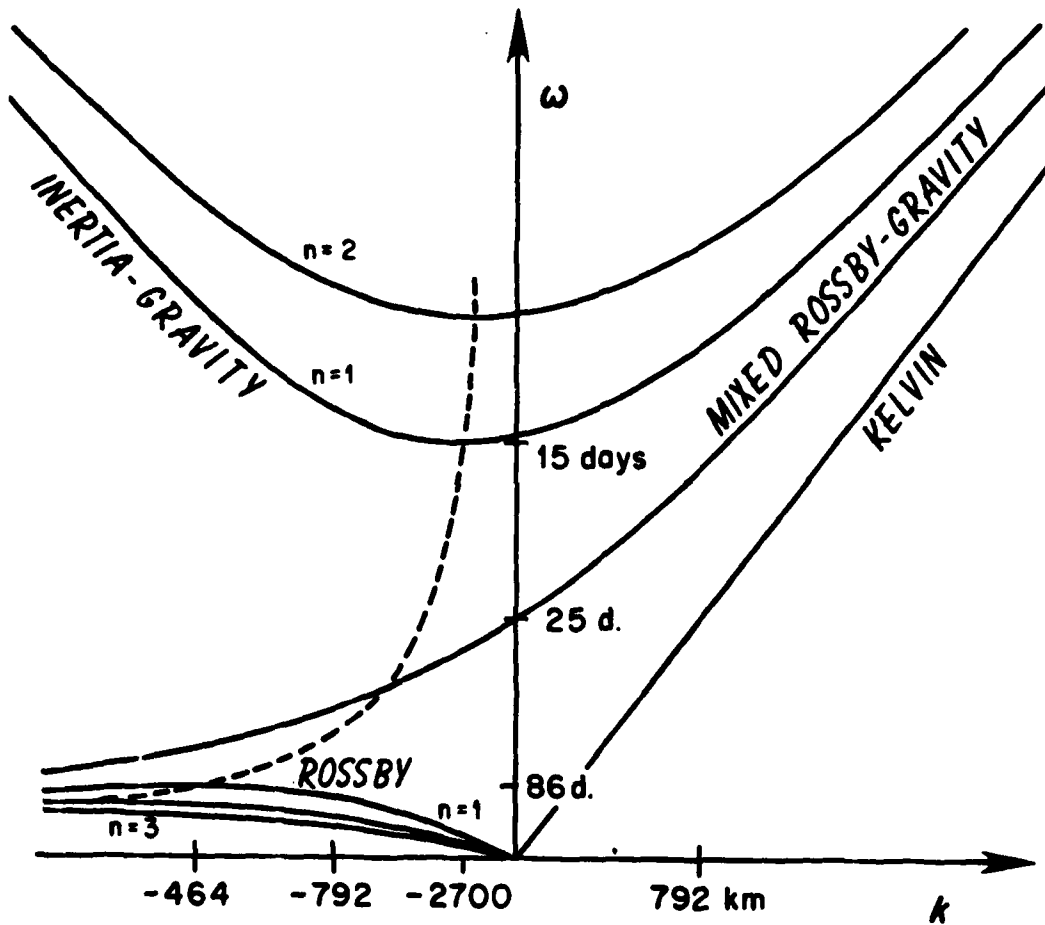


Figure I-6

A cut of the three-dimensional dispersion relation (Equation I-10) at the vertical wavenumber corresponding to a wavelength of 1200m. The curves are labelled by wave type, and critical periods and zonal wavelengths are indicated.

corresponding to Kelvin and mixed Rossby-gravity waves are labelled, as well as those for the Rossby and inertia-gravity waves. The phase velocity of Rossby waves is seen to be always westward, and the zonal group velocity is westward for long zonal wavelengths and eastward for short wavelengths. The dotted line distinguishes the inertia-gravity waves on the right, which propagate energy to the east, and those on the left which propagate energy to the west.

The general forms for zonal and vertical group velocity are:

$$c_g^x = \frac{\partial \omega}{\partial k} = \frac{2\omega k N_0^2 + \beta N_0^2}{3\omega^2 m^2 - k^2 N_0^2 - |m| \beta N_0 (2n+1)}$$

and

$$c_g^z = \frac{\partial \omega}{\partial m} = (\text{sgn } m) \frac{\omega \beta N_0^2 (2n+1) - 2|m|\omega^3}{3\omega^2 m^2 - k^2 N_0^2 - |m| \beta N_0 (2n+1)}$$

Since the denominators are the same, the ratio of the zonal group velocity to the vertical group velocity is simply

$$\frac{c_g^x}{c_g^z} = (\text{sgn } m) \frac{2\omega k N_0^2 + \beta N_0^2}{\omega \beta N_0 (2n+1) - 2|m|\omega^3},$$

which reduces to  $\frac{c_g^x}{c_g^z} = \frac{(\text{sgn } m) N_0}{\omega (2n+1)}$  in the low frequency limit for Rossby waves.

The Gaussian term in the general wave solutions (Equations I-12, 13a, 13b), which dominates the meridional structure of the zonal velocity of the Kelvin waves and the meridional velocity of the mixed waves, acts as a modifying factor rather than an envelope for the

Rossby and inertia-gravity modes. Their structure is better described in terms of the turning latitude (Equation I-11) than in terms of the e-folding distance. The meridional mode number defines the number of nodes in the  $V$  field between the equator and the poles, and thus functions in the place of a meridional wavenumber. The turning latitude defines the location where the wave solutions begin to decay poleward.

For inertia-gravity waves of a particular meridional mode number, the longer the period the more tightly trapped to the equator the waves become, since  $\omega = f$  defines the turning latitude. Equation I-8 can be solved for  $(gh_m)^{1/2}$ :

$$(gh_m)^{1/2} = \frac{-\beta(2n+1) \pm [\beta^2(2n+1)^2 + 4(\frac{\beta k}{\omega} + k^2)\omega^2]^{1/2}}{2(k^2 + \frac{\beta k}{\omega})}, \quad (17)$$

and the inertia-gravity solution corresponds to the choice of the plus sign. This equation reduces to  $\omega^2/\beta(2n+1)$  for large values of  $n$ , so that Equation I-9 becomes

$$y_T = \frac{\omega}{\beta}.$$

On the other hand, the number of Rossby modes which can be excited increases as the frequency decreases. If the equivalent depth ( $h_m^-$ ) is small (i.e., if the vertical length scale is short), the waves are equatorially-trapped, since the turning latitude becomes further from the equator as the equivalent depth increases. For large values of  $h_m^-$  or, equivalently, long vertical length scales, the Rossby waves cannot be adequately described on an equatorial beta-plane. These

limits were pointed out by Philander (1978).

B.2.d. Symmetry and antisymmetry. The meridional symmetry of the problem defined by the differential equation and the boundary conditions implies that the solution will be composed of symmetric or antisymmetric functions. For the meridional velocity field, the meridional mode number is the Hermite polynomial order number. It has odd or even symmetry about the equator depending upon the mode number, because the Hermite polynomials of odd order are sums of odd powers of latitude. The zonal velocity and pressure wave fields have opposite symmetry to the  $v$  field, since they are composed from the Hermite polynomials of adjacent orders. For meridional modes of odd order, the  $v$  field has a node (zero) at the equator (i.e., is antisymmetric about the equator) and the  $u$  and  $p$  fields have a local maximum or minimum at the equator (i.e., are symmetric about the equator). The converse holds as well.

## CHAPTER II - Data Acquisition and Reduction Procedures

The methods used to reduce the White Horse data for subsequent analysis are discussed here after a brief description of the instrument and its deployment. The data recorded by the instrument are first converted to velocity components and the horizontal velocity profiles are then scaled using the buoyancy profile calculated from the density data. Vertical displacement is also calculated from the density data, and similarly scaled, in order to provide additional comparisons to linear wave theory. The WKB scaling transformations are chosen to provide constant coefficients to the lowest order in the vertical structure equation, allowing sinusoidal solutions, for use in possible interpretation of vertical wavenumber analysis of the data.

### Section A. Initial Data Processing

A.1. Description of the instrument and its deployment. The White Horse System consists of an acoustic dropsonde, approximately two meters long and containing a standard Neil Brown CTD, acoustic navigation and recording equipment, and a network of (initially) three bottom-tethered transponders. Figure II-1 is a photograph of the instrument being lowered over the side of a research vessel, after which it is released and falls freely to the bottom. The transponders have previously been deployed in an approximately equilateral triangle (on the order of 4 km per side) on the ocean bottom. As the dropsonde descends through the water column, it transmits an 11.0-Khz pulsed signal every 20 seconds, which stimulates a return signal from each of



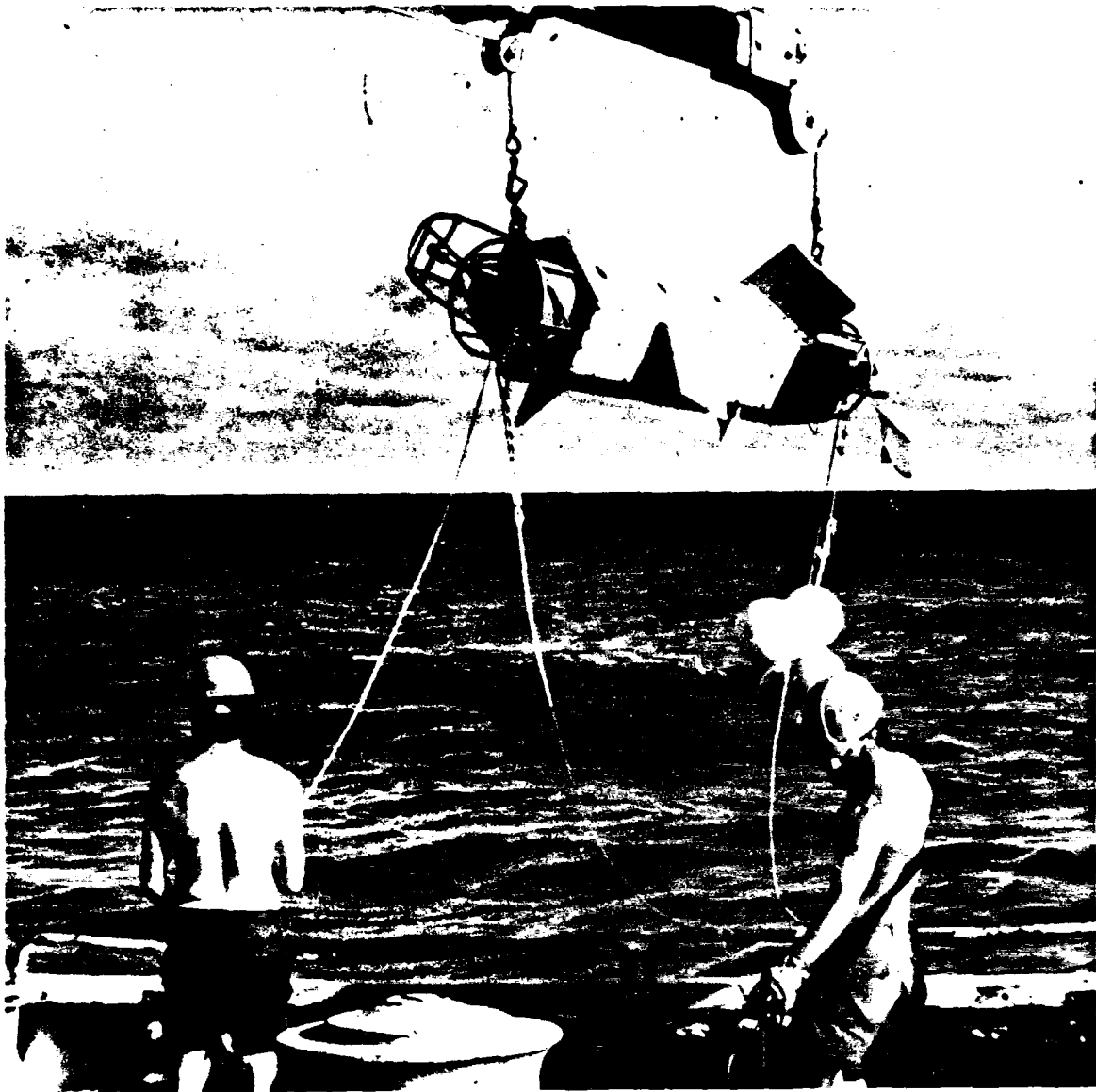


FIGURE II-1

Photograph of the White Horse on a crane,  
prior to launching at a profile station.

the bottom transponders. The time intervals between interrogation and reply are stored on a magnetic tape cassette within the White Horse.

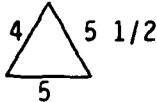
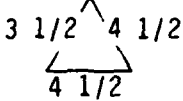
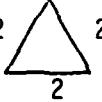
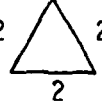
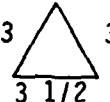
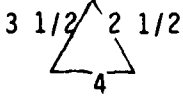
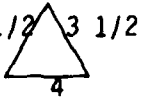
When the instrument reaches the ocean floor, its anchor is released by one of three mechanisms: a pre-set clock, an acoustic signal or a *corrosible magnesium link* in the connecting chain. The instrument then rises to the surface, acoustically tracking its trajectory as in descent. An acoustic signal to the AMF release is the normal method and reliance on the *corrosible link*, the second-order backup, has never been required for retrieval.

An acoustic survey is performed from the surface to determine the depths and relative positions of the three bottom transponders. The relative positions of the transponders are resolved using a least squares minimization procedure, from an overdetermined (more than six interrogation sites) set of ranges from the surface to the transponders (vanderKulk, 1961). Additional information collected during the survey from satellite fixes and dead-reckoning navigation allows the subsequent determination of the absolute positions of the transponders, and thus the absolute orientation of the network, to within  $\pm 5^\circ$ . Table II-1 contains survey results for the 1976 White Horse Indian Ocean networks.

A.2. Conversion of travel times to velocity components. The round-trip travel times are converted to three-dimensional ranges using the local sound velocity profile, computed from the CTD data. An iterative triangulation calculation (described in Luyten, Needell and Thomson, 1982) uses the ranges and transponder positions to find the

TABLE II-1

## WHITE HORSE SURVEY RESULTS

Profile Series	Location (Beacon 1 approx.)	Date of Survey 1976	Net Coordinates beac 1: x,y,z beac 2: x,y,z beac 3: x,y,z	Orientation of Net °E of N	Net Dimensions (km)
500	0° N 50°30' E	May 13	0, 0,5049 5291, 0,5046 1551,3950,5052	9	
600	0° N 53° E	May 15	0, 0,5049 4369, 0,5043 1323,3228,5049	0	
	0° N 53° E	June 15	0, 0,5049 3620, 0,5043	0	- 3 1/2 -
700	0°45' N 53° E	May 29	0, 0,5054 2137, 0,5053 1154,1715,5057	0	
800	1°30' N 53° E	May 30	0, 0,5091 2192, 0,5085 1129,1834,5091	-5	
900	3° N 53° E	May 31	0, 0,5099 3547, 0,5101 1745,2161,5101	7	
1000	5° N 53° E	June 1	0, 0,5083 3792, 0,5083 2457,2181,5085	5	
1100	0°45' S 53° E	June 5	0, 0,4994 3880, 0,4991 2667,3439,4993	0	

(x,y,z) location of the instrument within the water column. The instrument's position is determined every 20 seconds, or approximately every 20m in depth since the rise and fall rates are  $\sim 1$  m/sec. CTD data are collected once per second, so that they are twenty times as dense as the velocity data.

The horizontal position of the instrument is differenced and provides a direct measurement of the horizontal velocity components. A thorough analysis of the sources and magnitudes of errors inherent in or incidental to the White Horse System (i.e., unavoidable and random errors) was performed by Luyten, Needell and Thomson (1982). A hydrodynamical analysis of instrument response time was done by Hendricks and Rodenbusch (1981).

On occasion, the third bottom transponder has been recovered (for use at another station) before all instrument drops at a location were completed. In those cases, the triangulation calculation proceeds using two transponders and depth, the latter obtained from the White Horse CTD pressure sensor. Absolute velocity errors are somewhat higher, for that case (cf. Figure 7 of Luyten, Needell and Thomson, 1982). Table II-2 indicates which triangulation method was used for each profile.

A typical survey pattern is shown in Figure II-2. The surface track which the ship steamed while performing the survey is indicated by a dashed line. Individual survey points (shown as black dots) were collected while the ship was freely drifting and are used in the least-squares fit to locate the beacons with respect to each other.

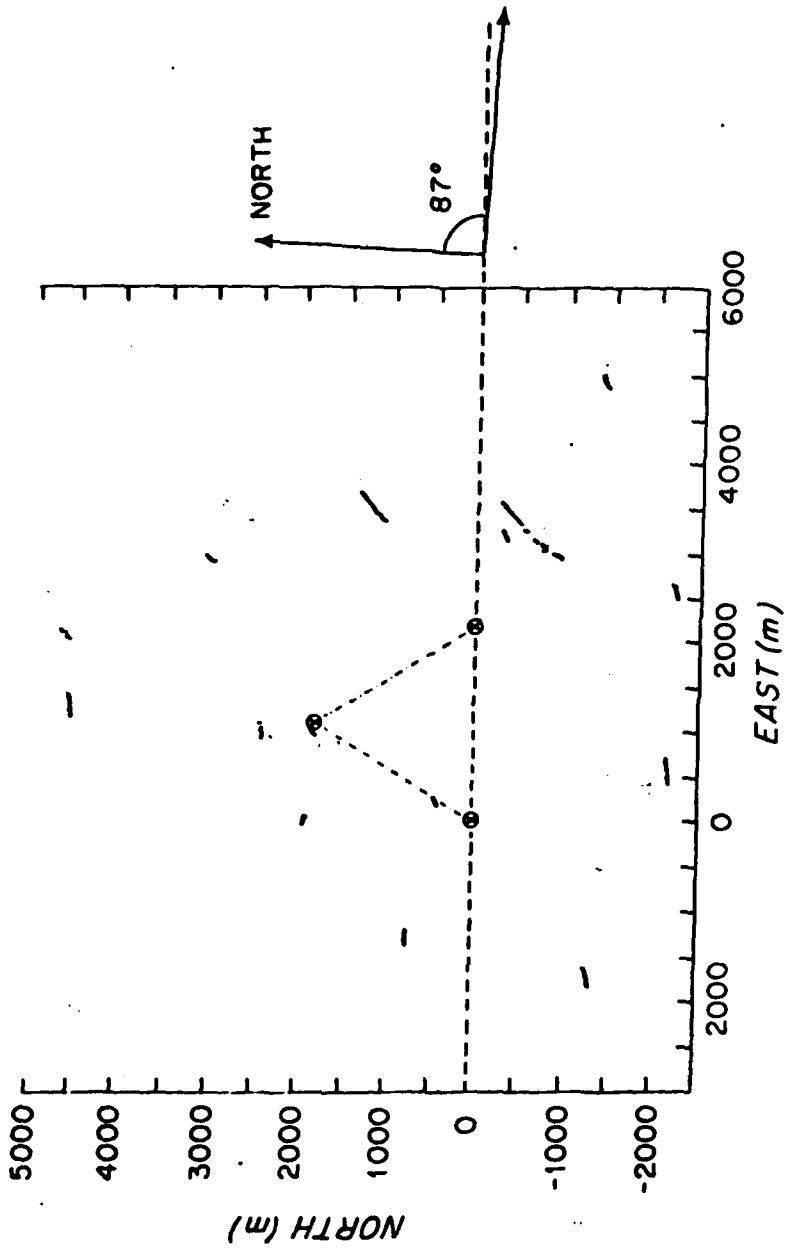


FIGURE II-2

Transponder survey pattern and network layout.

The bottom positions of the transponders, determined from the survey processing, are shown as crossed circles.

Figure II-3 presents profile 607 in plan view. Only the horizontal location of the White Horse, from release to retrieval, is shown. The symbol "+" marks the down track, "Δ" the up track. The spacing of the symbols indicates that the fall rate was slightly slower (about 20 per cent) than the rise rate so that the instrument had less time to move horizontally within the flow field while rising vertically. All the data used here have been interpolated onto a uniform 25m depth grid, to provide regular series for comparison.

Because the conductivity sensor is located at the bottom of the instrument when it rides in the water, the only useful CTD data are from the down profiles when the sensor is not affected by instrumental entrainment. Vertical isopycnal displacements calculated from the CTD data are thus available as profiles corresponding to the down velocity profiles. Consequently only the down portions of drops were used for cross-spectral estimates and for the dropped lagged coherence estimates. The exception is profile 705, for which only an incomplete down trace was obtainable. The velocity data from up and down profiles are equally accurate, however, and both profiles were used for the autospectral estimates in Chapters III and IV. Comparison of up and down profiles indicates that there are no nontidal systematic differences (Luyten, Needell and Thomson, 1982).

Table II-2 summarizes pertinent information about each White Horse profile. In a few indicated cases, a physically different but

## DROP # 607 ...LOCATION OF WHITEHORSE

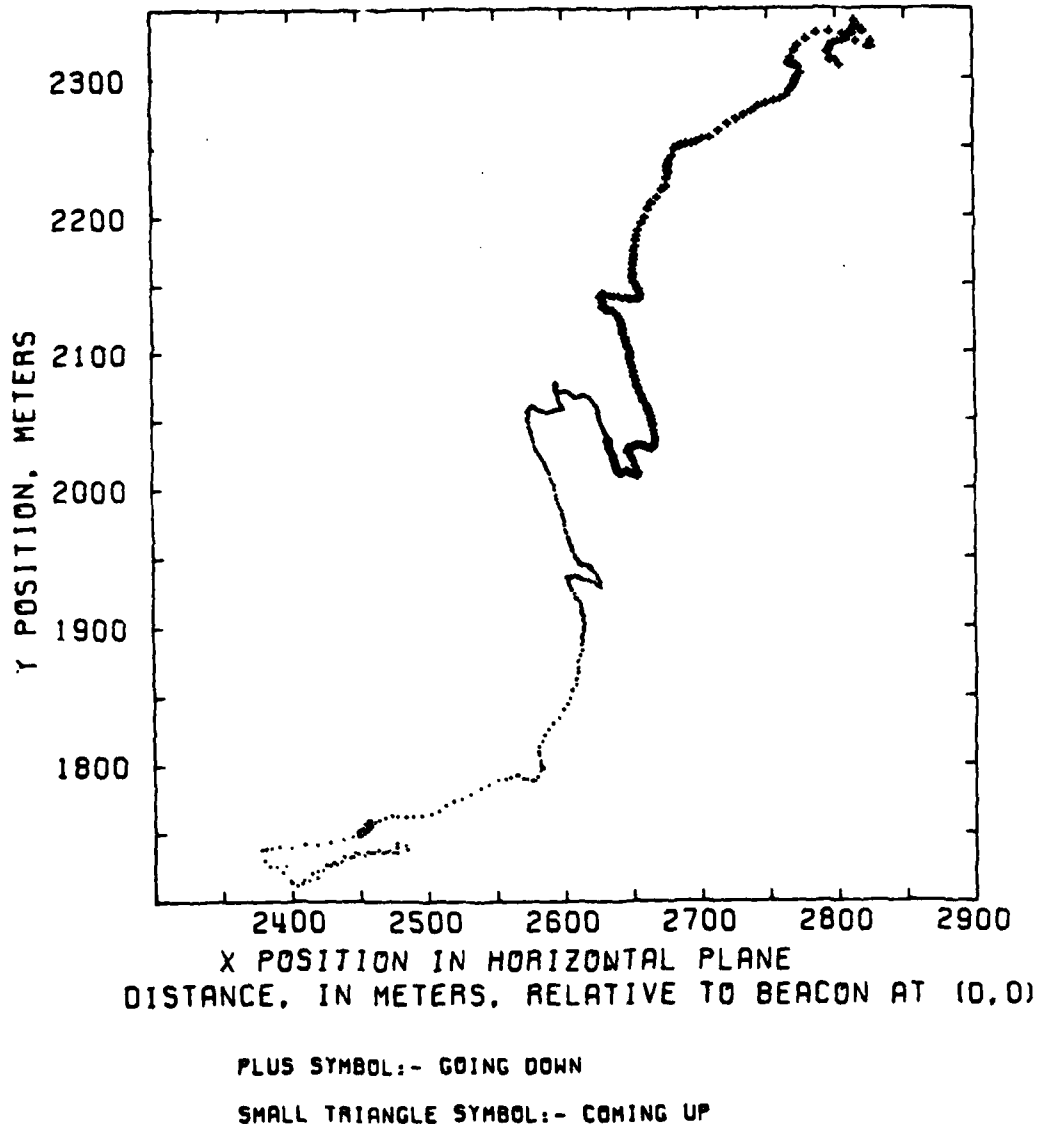


FIGURE II-3

White Horse profile track in plan view, showing zonal and latitudinal peregrinations.

TABLE II-2

## 1976 WHITE HORSE DATA

Profile	Date and Time	Code	Beacon	Notes
501	May 14 0820	DSX	23	Top 450m of up profile combined with rest of down profile. Signal lost below 4765m. Beacon 1 unusable due to distance
502	May 28 1035		23	
503	May 28 1706		23	
504	June 18 1010	BDS	23	CTD flooded at 2464m down
601	May 16 0900	Z	23	Beacon 1 noisy or no signal.
602	May 29 1238	*	12	North comp. noisy, upper 500m up
603	June 4 1854		12	No data
604	June 5 0018	*S	12	
605	June 6 0635	*	12	
606	June 11 0540	*D	12	Beacon 2 released from bottom with dropsonde
...	new net, due to beacon replacement			
607	June 12 2112	*	12	
608	June 15 1820	*	12	40-second sampling interval interpolated to 20 sec.
609	June 15 1933	B	12	609..heavy interpolation, less on up
610	June 16 1855	B	12	Heavy interpolation on up, above 2490m
611	June 17 1216	B	12	
701	May 17 1321		A	Instrument close to baseline
702	May 30 0815	*	23	Beacon 1 noisy
703	June 4 0655	*	A	Instrument close to baseline
704	June 6 1659	*	A	Instrument close to baseline
705	June 10 2032	*4	A	Down starts at 2775m, (4) Up noisy, but O.K.
706	June 13 0637	*D4	A	No down profile above 150m Up not usable (4)

Code	Beacon Configuration
*	Good CTD data
B	All 3 beacons used for position calculations.
D	Black Horse instrument used
S	Only 'down' profile available
X	12 Beacons 1,2 and pressure....
Z	Profile shallower than 4900 m
4	23 Beacons 2,3 and pressure....
	Beacon 1 retrieved after drop
	Beacon 3 retrieved after drop
	4ms problem, see data report (Spencer, O'Neill and Luyten, 1980)



TABLE II-2 (Continued)  
1976 WHITE HORSE DATA

Profile	Date and Time	Code	Beacon	Notes
707	June 15 0803	*	A	
708	June 17 0317	BD	12	Heavy interpolation above 1600m Pressure case flooded at 3200m up No signal from beacon 3
801	May 18 0254		A	
802	May 30 2346	*Z	A	
803	June 3 1855	*	12	
804	June 7 0349	*D	12	Up not usable, multiple problems No down profile above 350m
805	June 10 0753	*	12	Noisy data upper 200m
806	June 13 1517	*	12	No down profile above 200m
807	June 14 2343	*D4	12	5 point smoothing done on noisy pressure data. Heavy interpola- tion around 750m down (4) Up not usable (4)
901	June 1 0106	*Z	A	No up profile above 300m (rain!)
902	June 3 0444	*	12	
903	June 7 1818	*D4	12	No down profile above 100m Up not usable (4)
904	June 9 1821	*	12	
905	June 14 0411	*	12	
1001	June 2 0643	*Z	A	Heavy interpolation 300-450m up
1002	June 8 1436	*	12	No up profile above 475m
1003	June 9 0125	B	12	
1101	June 5 2202	*	AC	Below 3000m, profiles formed from 2,3 beacon case
1102	June 12 0440	*	A	
1103	June 16 0547	B	AC	950-3100m, profiles formed from 2,3 beacon case

Code

\* Good CTD data  
 B Black Horse instrument used  
 D Only 'down' profile available  
 S Profile shallower than 4900 m  
 X Beacon 1 retrieved after drop  
 Z Beacon 3 retrieved after drop  
 4 4ms problem, see data report (Spencer, O'Neill and Luyten, 1980)

Beacon Configuration

A All 3 beacons used for position  
 calculations.  
 12 Beacons 1,2 and pressure....  
 23 Beacons 2,3 and pressure....

electronically identical version of the instrument, named the Black Horse, was used in place of the White Horse. A data report covering both the White Horse profiles analyzed here and associated current meter observations was prepared in 1980, and contains additional details regarding both (Spencer, O'Neill and Luyten, 1980). Comparison of White Horse and simultaneous current meter velocity measurements has been used to confirm the velocity error estimates above (Luyten, Needell and Thomson, 1982) and also the absolute orientations of the transponder nets (Needell, personal communication).

The White Horse system has been used in several other locations and oceanographic experiments:

- Western Sargasso Sea [MODE-0] 1972 (Gould, Schmitz and Wunsch, 1974)
- Gulf Stream 1974 (Spencer, 1979, WHOI data report)
- Equatorial western Pacific 1978 (Eriksen, 1981)
- Equatorial western Indian Ocean 1979 [INDEX]. Some of the same plus additional stations; much more extensive coverage along the equator, from 47°E to 62°E. (Luyten et al., 1980; Levy, Spencer and Needell, 1981, WHOI data report, in preparation)
- Equatorial central Pacific 1981 [PEQUOD].

## Section B. Calculations from the CTD Data

B.1. Buoyancy Frequency. Buoyancy frequency profiles were calculated using a least squares fit of the gradient of potential specific volume anomaly, for all drops where CTD data were available

and could be edited. Table II-2 indicates the profiles for which CTD data were available. [Those from Black Horse drops (excluded because its CTD malfunctioned), drops which did not reach the bottom and those immediately after replacement of a broken conductivity cell were not used. There is no CTD data from  $0^\circ, 51^\circ 30'E$ ; all data is from the  $53^\circ E$  meridian.] An average buoyancy frequency profile [ $=N(x,z)=N(z)$ ] was produced, in order to minimize the perturbations on the background stratification peculiar to a particular place or time. This average was used to reduce each velocity profile to the form which might have been observed in a uniformly stratified ocean.

The temporal averages of  $\overline{N^2(x,y,z)}$  at each latitude were ensemble-averaged to produce a profile of  $\sqrt{\overline{N^2(x,z)}}$ . The only spatial smoothing applied is thus latitudinal. No smoothing was done over depth. Such smoothing was examined and had no visual or spectral impact. The buoyancy frequency profile used for WKB stretching and normalizing as well as for the displacement calculations (below) is shown in Figure II-4.

B.2. Vertical Displacement. Vertical displacements of isopycnals from their equilibrium positions have been calculated by a comparison of individual CTD profiles to a space-time average of sigma theta which defines the background stratification. The linearized conservation of mass equation for an incompressible Boussinesq fluid can be written

$$\frac{\partial \rho_\theta}{\partial t} - w \frac{\partial \bar{\rho}_\theta}{\partial z} = 0 \quad (\text{II-1})$$

where  $\rho_\theta$  is the deviation of potential density from the mean ( $\hat{\rho}_\theta = \rho_\theta - \bar{\rho}_\theta$ );

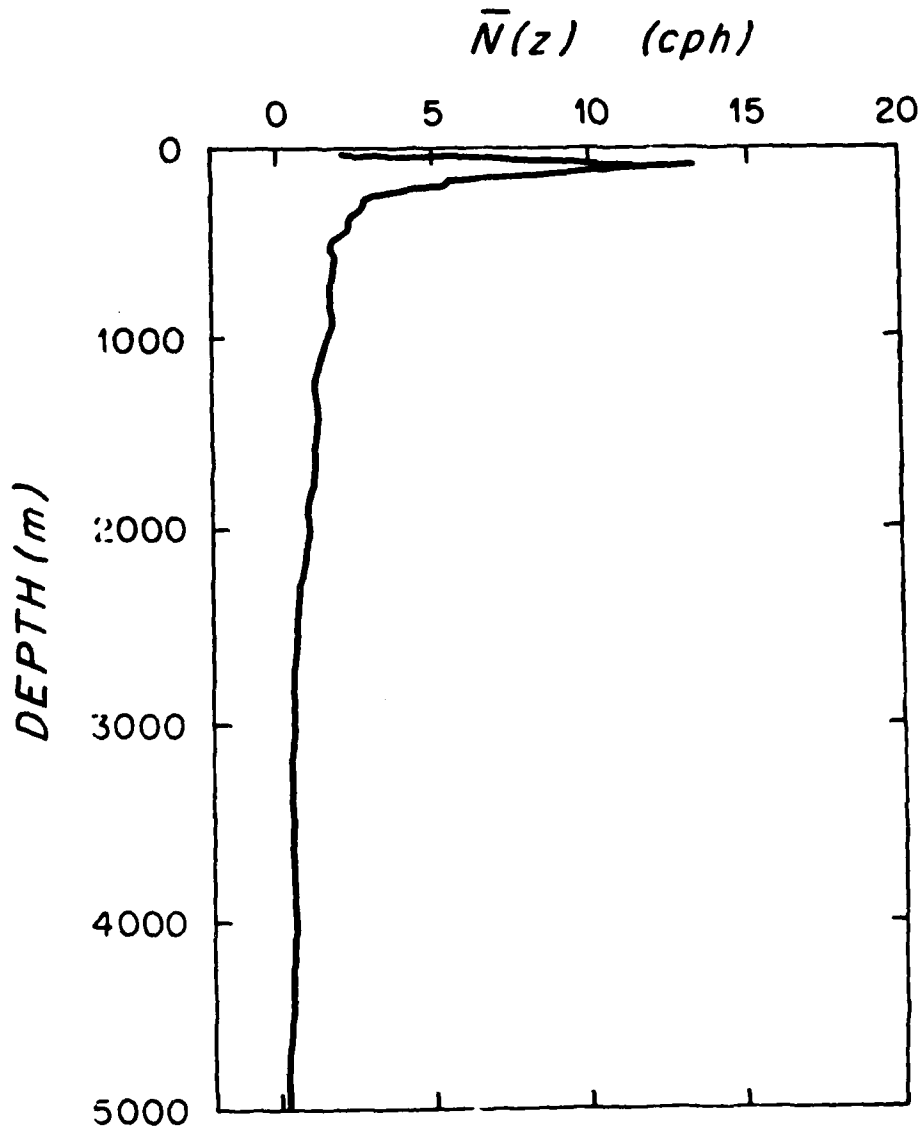


FIGURE II-4

Plot of  $\bar{N}(z)$  against depth: illustration of the average buoyancy frequency profile used for WKB stretching and normalizing, and in the calculation of vertical displacement.

$\hat{\rho}_\theta$  is the observed potential density [ $= 1 + 10^{-3}\hat{\sigma}_\theta$ ]). Since  $\int = \int w dt$ , where  $\int$  is vertical displacement measured upward, equation II-1 can be integrated in time to yield

$$\begin{aligned} \int(x,y,z,t) &= \frac{\hat{\rho}_\theta(x,y,z,t) - \bar{\rho}_\theta(x,z)}{\bar{\rho}_\theta(x,z)} \frac{g}{N^2(z)} \\ &= \frac{g}{N^2} \frac{\hat{\sigma}_\theta - \bar{\sigma}_\theta}{10^3 + \bar{\sigma}_\theta}, \end{aligned} \quad (\text{II-2})$$

where  $N^2(z) = -\frac{g}{\bar{\rho}_\theta} \frac{\partial \bar{\rho}_\theta}{\partial z}$ . Equation II-2 was used to calculate the displacement profiles presented here. The computation of  $\hat{\sigma}_\theta$  included a least squares fit of the in situ potential specific volume anomaly over a variable depth interval, referred to the center of the interval: 100db above 500m, calculated every 25db; 200db between 500 and 4000m, and 400db below 4000m, calculated every 50db for the latter intervals. Values above 50m and below ~4800m are extrapolated, and the profile is interpolated to the same 25m depth grid used for the velocity data. Adjacent values are therefore not independent anywhere in the water column, which accounts for the relative smoothness with depth of the variability in the displacement profiles. (See Appendix A.) Average  $\hat{\sigma}_\theta$  was obtained by ensemble-averaging the temporal averages at latitudes  $3/4^\circ\text{S}$  to  $3^\circ\text{N}$ . The buoyancy frequency profile used to compute displacement is the space-time average discussed above and used below for WKB stretching and normalizing.

The calculation can be visualized graphically:

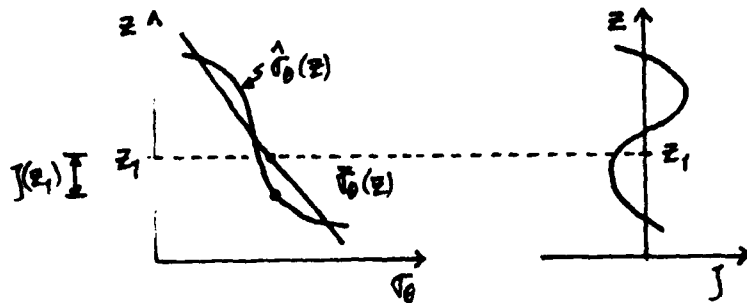


FIGURE II-5

Sketch illustrating calculation of vertical isopycnal displacement using deviations of an individual sigma theta profile from the space-time average sigma theta profile.

$$\text{i.e., } J(z_1) = \frac{\hat{\sigma}_\theta(z_1) - \bar{\sigma}_\theta(z_1)}{\frac{d\bar{\sigma}_\theta(z_1)}{dz}} . \text{ Density fluctuations due to horizontal}$$

displacements have been ignored, and the underlying assumption is that spatial averaging over four degrees of latitude and temporal averaging over three weeks provides a sufficient approximation to the equilibrium density field. For sample profiles, see Figure II-6. The full set of displacement profiles are shown as latitudinal sections in Appendix A and as temporal sections at each station in Appendix B.

### Section C. WKB Stretching and Normalizing Procedures

To permit simultaneous treatment of upper and lower portions of the water column, the apparent dependence of velocity amplitude and vertical length scale upon the buoyancy frequency has been removed,

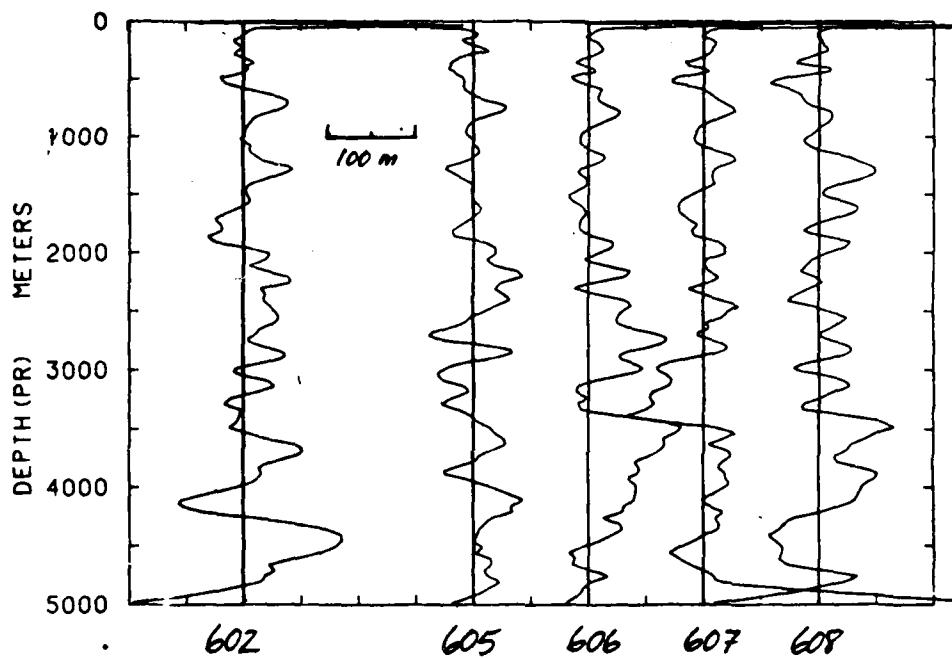


FIGURE II-6

Sample of displacement profiles. These are the five profiles available at the equator,  $53^{\circ}\text{E}$ . See Appendices A and B for full set of profiles.

using a WKB stretching and normalizing procedure first discussed by Bell (1974). Observational evidence justifying this procedure, based on moored current meter measurements, can be found in Luyten (1982). Theoretical justification is based upon the solutions to the vertical structure equation discussed in Chapter I-B.

Horizontal velocities are scaled by dividing them by  $[\bar{N}(z)/N_0]^{1/2}$ , where  $\bar{N}(z)$  is the average buoyancy frequency profile described in Section B.1 and  $N_0$  is the average of that profile. The  $N_0$  used here is 1.0915 cph, for reasons which are mentioned below.

$$u^*, v^* = \left\{ \frac{N_0}{\bar{N}(z)} \right\}^{1/2} u, v$$

$$j^* = \left\{ \frac{\bar{N}(z)}{N_0} \right\}^{1/2} j .$$

The vertical coordinate is correspondingly stretched, by multiplying each depth increment by the buoyancy frequency at that level, normalized by  $N_0$ .

$$z^* = \int \frac{\bar{N}(z)}{N_0} dz .$$

When the  $N_0$  used is the average of the Brunt-Vaisala profile used, as here, the stretched vertical profile ( $u^*$ ,  $v^*$  or  $j^*$  as functions of  $z^*$ ) maps back onto the original total water depth, 5000m in this case becoming 5000 stretched meters (sm). Vertical wavelengths and scales can then be readily interpreted as fractions of the total water depth, i.e.,  $\lambda_z=1200\text{sm}$  implies approximately four wavelengths between the surface and the bottom.



The maximum stretched depth interval between 25m-data points is 263sm at 100m, where  $\bar{N}$  is 13.4 cph. The maximum interval in the depth series used for spectral analysis (see Section D) is 63sm, corresponding to  $\bar{N}(262.5\text{m})=2.7$  cph. The minimum stretched depth interval is 4sm, where  $\bar{N}(4987.5\text{m})$  is 0.18 cph. The unequally-spaced stretched data have been interpolated onto a uniform 25sm depth grid.

An adaptive filtering technique was used to smooth the stretched data in the lower part of the water column, where a 100m interval in the vertical coordinate is condensed into as little as 16sm. A boxcar filter was applied to the scaled data before stretching. The filter length is determined by the relationship between the local and the depth-averaged buoyancy frequencies, according to the following formula (Dunlap, personal communication):

$$x^*(z) = \frac{1}{2n + 1} \sum_{z - n\Delta z}^{z + n\Delta z} x^*(z) , \quad (\text{II-3})$$

where  $n = 1/2 N_0/\bar{N}(z)$ . The filter has no impact upon the upper part of the stretched water column, where the local buoyancy frequency is greater than  $N_0$ , but smooths data in the lower portion over as much as 150sm.

The resultant velocity vectors have been used for the analysis to be described. The upper 300m of the water column is expanded to the upper 1500sm of the stretched profile; the bottom kilometer of the water column is condensed to the lower 300sm of the stretched profile. Upper level velocities have been relatively reduced and lower level

velocities enhanced. One can now discuss vertical wavenumbers throughout the temporal and spatial array rather than merely local vertical wavenumbers. Figure II-7 shows the stretched vertical coordinate ( $z^*$ ) plotted against depth ( $z$ ) and illustrates the one-to-one mapping of 5000m onto 5000sm. The upper part of the figure, corresponding to the top 275m of the total ocean depth, has been crosshatched, to indicate the equivalent top 1400sm of the stretched coordinate. The impact on the original data of the WKB stretching and normalizing is evident in Figure II-8.

#### Section D. Spectral Analysis Methods

Time series analysis has been used in this study in two ways: conventionally, as a means of determining the distribution of energy among vertical wavenumbers (autospectra) and phase relationships between variables (cross-spectra), and less conventionally, looking at dropped lagged coherence and phase (a particular averaging of cross-spectra) to detect vertically standing or propagating waves. In both cases, the upper 275m of the water column has been ignored. The density gradient is changing rapidly there and the first-order WKB approximation implicit in the scaling is not applicable. In addition (and perhaps more importantly), linear wave theory is unlikely to be an appropriate model in that region, so that spectral decomposition of this portion of the data would be less informative. The total depth interval analyzed is 3600sm, so that the maximum spectral resolution with standard techniques is wavelengths of 3600, 1800, 1200, 900, ...sm. The top of the series used is 1412.5sm, corresponding to the

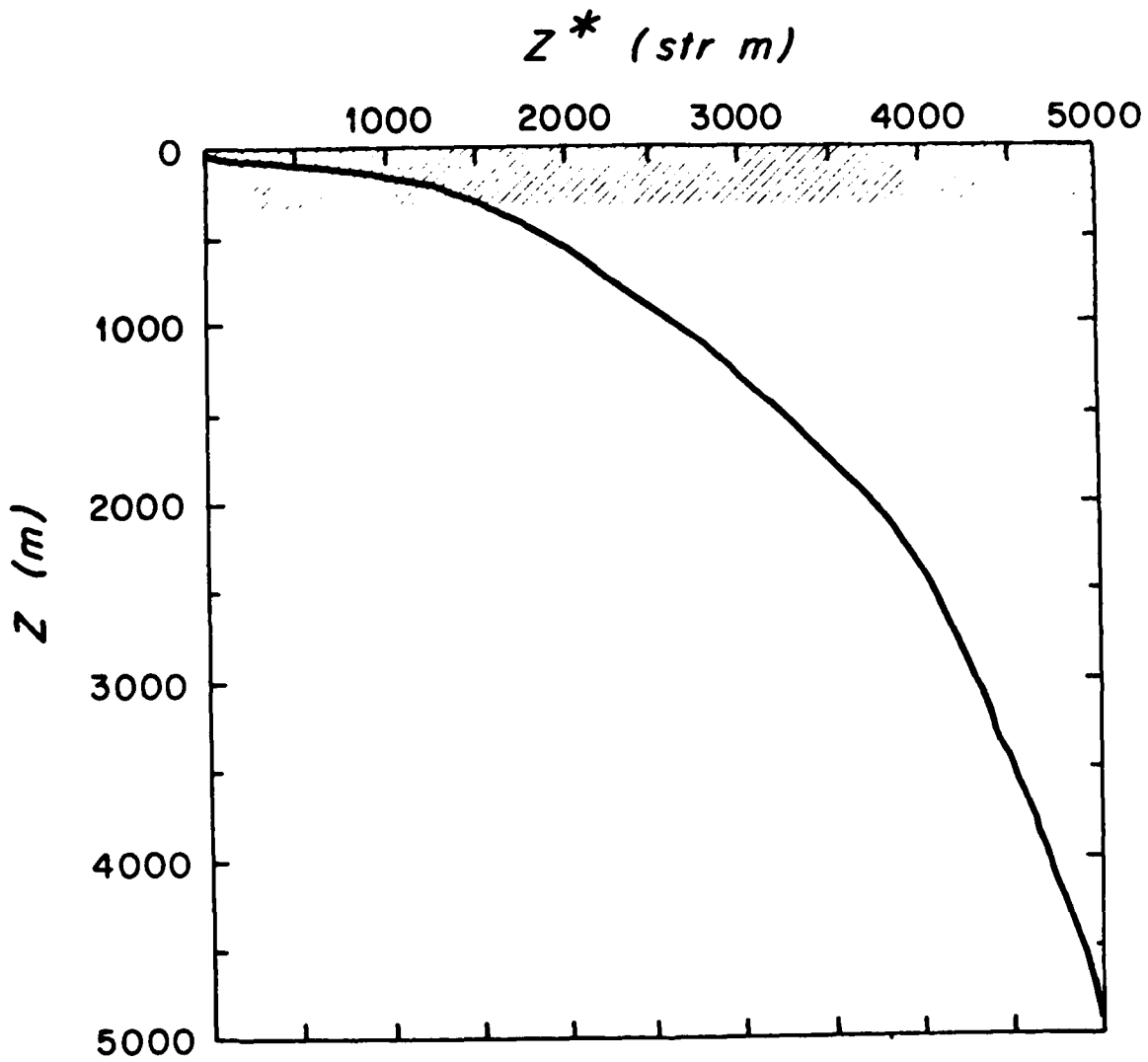
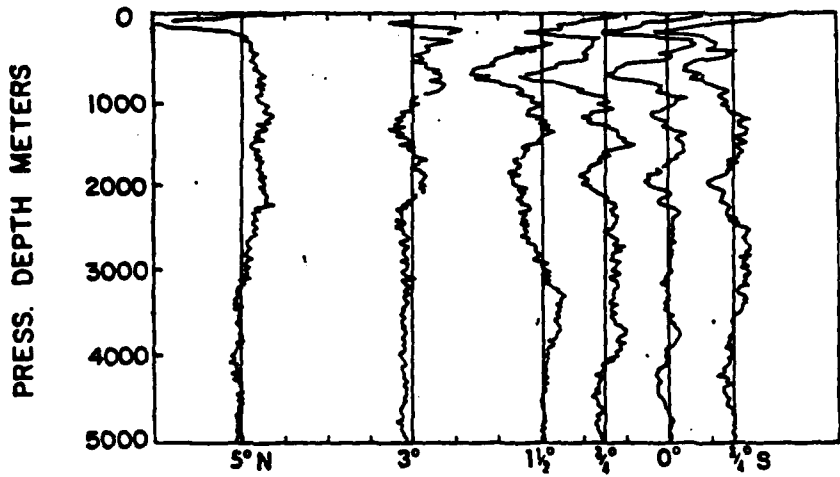


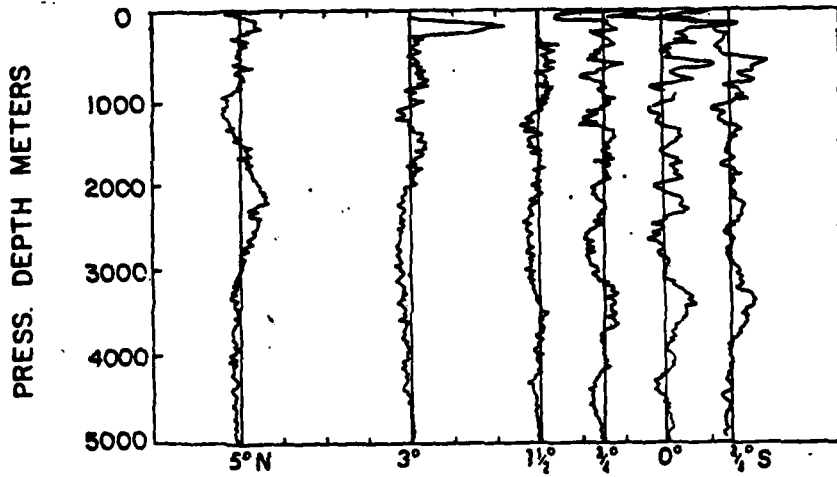
FIGURE II-7

Plot of  $z^*$  against  $z$ : stretched vertical coordinate versus depth, illustrating the smoothness of the WKB one-to-one mapping.

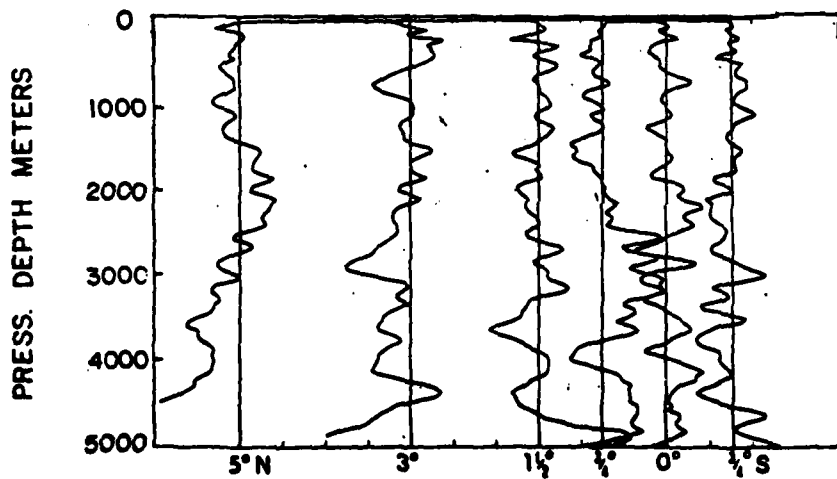
SECTION 4



U



V

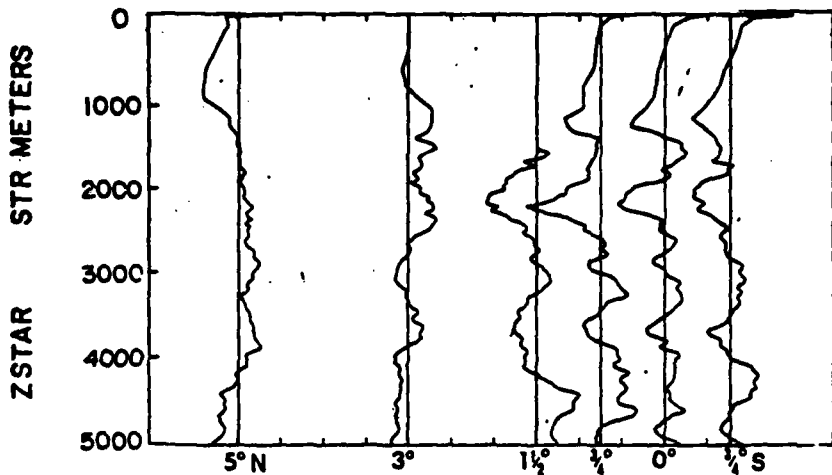


S

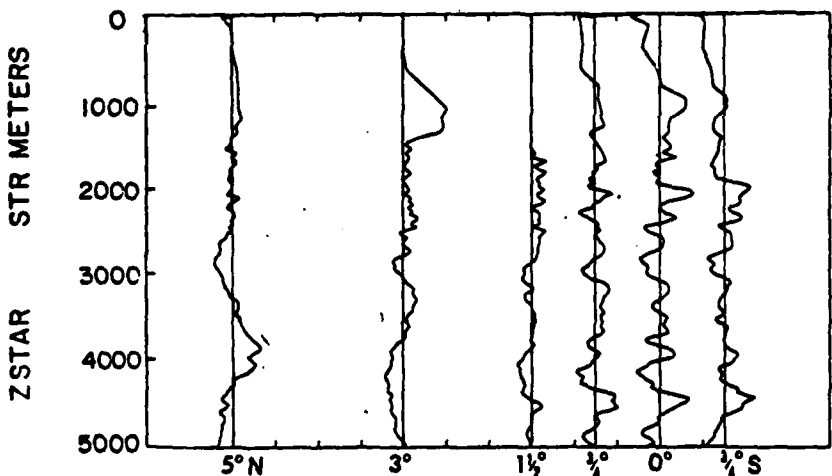
FIGURE II-8(a)

Original data: u, v, s.

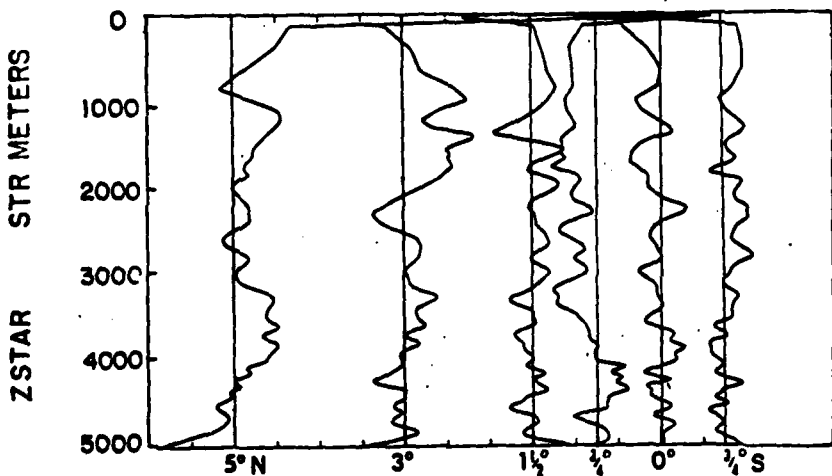
SECTION 4



$U^*$



$V^*$



$S^*$

FIGURE II-8(b)

Stretched and normalized data.

original data point 262.5m(1399sm). The deepest point used is 4987.5sm, corresponding to 4887.5m(4990sm).

A 10% 1/2-cosine bell is used to taper the data prior to spectral decomposition (Koopmans, 1974, p.302). This taper, a smooth modulating function, removes end effects, but also removes half the energy from the first and last ten percent of the record. The final spectral values should thus be adjusted by a factor of 1.11 (Munk, Snodgrass and Tucker, 1959), before comparison with untapered spectra.

D.1. Auto- and cross-spectra. A question which can be addressed via autospectral analysis is that of vertical homogeneity. Decomposition of the 3600sm profiles at net 6 into upper and lower 1800sm pieces reveals no significant differences in their autospectra. The two halves were not tapered prior to the spectral computation.

Statistical reliability of spectral estimates with no wavenumber averaging is dependent upon the number of pieces (in this case, profiles available at each latitude) included in each estimate. CTD data are available for a subset of profiles at each net, and have been used to compute vertical displacement profiles. At the equator, CTD data and thus vertical displacement are available for only half of the velocity profiles, spanning a total of two and a half weeks. At 3/4°N, CTD data are available for six of the eight drops, spanning the same time period as at the equator. The maximum number of vertical displacement profiles at a single latitude is six at 3/4°N and 1.5°N, and falls to a minimum of two, at 3/4°S and 5°N. There are five profiles at two stations, the equator and 3°N. All of the above are

along the 53°E meridian. There is none available at the other equatorial station at 50°30'E.

A relevant question regarding the cross-spectral phase estimates involves the accuracy of the determination of the absolute net orientations. It was asserted in Section A.1 that the orientations had been resolved to within  $\pm 5^\circ$ . General conclusions from a test of the impact of orientation errors, by rotation of the velocity vectors, are that the combination of high coherence and a  $90^\circ$  phase estimate is invariant with respect to rotation, since that result is dominated by the quadrature spectrum, which is invariant (Fofonoff, 1969). The combination of high coherence and a  $\sim 180^\circ$  phase estimate is affected by rotation, however. Rotation in either direction produces at first a gradual decrease in both coherence and phase. A rotation of  $30^\circ$ , for instance, changes the phase estimate for net 6 at a wavelength of 1200sm by only  $16^\circ$ , while the coherence remains significantly non-zero. However, coherence amplitude drops to a minimum at  $45^\circ$ , when the components are in quadrature, and then increases to a maximum at  $90^\circ$ , when the components are in phase. It seems unlikely, therefore, that any of the cross-spectral results presented in Chapters III and IV are affected by net orientation errors.

D.2. Dropped Lagged Coherence and its interpretation. Since the 1976 White Horse velocity profiles constitute a time series of snapshots of the water column, it is possible to use them to examine temporal behavior as well as vertical scales. Specifically, it is possible to use them to examine the question of vertical phase

propagation of the observed oscillations. The method applied is known as dropped lagged coherence (DLC) (cf. Hayes, 1975). Pairs of profiles separated by the same temporal lag are grouped and their ensemble-averaged cross-spectra computed. For each variable, changes in coherence and phase estimates with temporal lag can then be analyzed in a particular vertical wavenumber band, and, in special cases, lend themselves to straightforward interpretation.

An assumption underlying the approach of dropped lagged coherence is that vertical profiles at the same geographical location represent stationary processes, so that the cross-spectra for a particular wavenumber band are a function primarily of the time difference between the profiles. The cross-spectral estimates for each vertical wavenumber and for each pair of profiles are assumed to be independent. A certain degree of homogeneity within a profile is required in order to produce a detectable signal, i.e., a single process must be responsible for variability throughout a substantial portion of the water column at a particular vertical scale.

Two simple models of wavelike motion in vertical profiles are illustrated in Figure II-9. For particular frequency and vertical wavenumber, the models are of a standing wave (vertical mode) and of a propagating wave. For a standing wave, dropped lagged coherence would drop to zero and phase would change by  $\pi$  at temporal lags equal to  $1/4$  and  $3/4$  of the wave period. Coherence would be high at temporal lags of some integral multiple of half the wave period. For a vertically propagating wave, coherence would be expected to maintain a



IDEALIZED EXAMPLES FOR A WAVELENGTH = 2/3 DEPTH

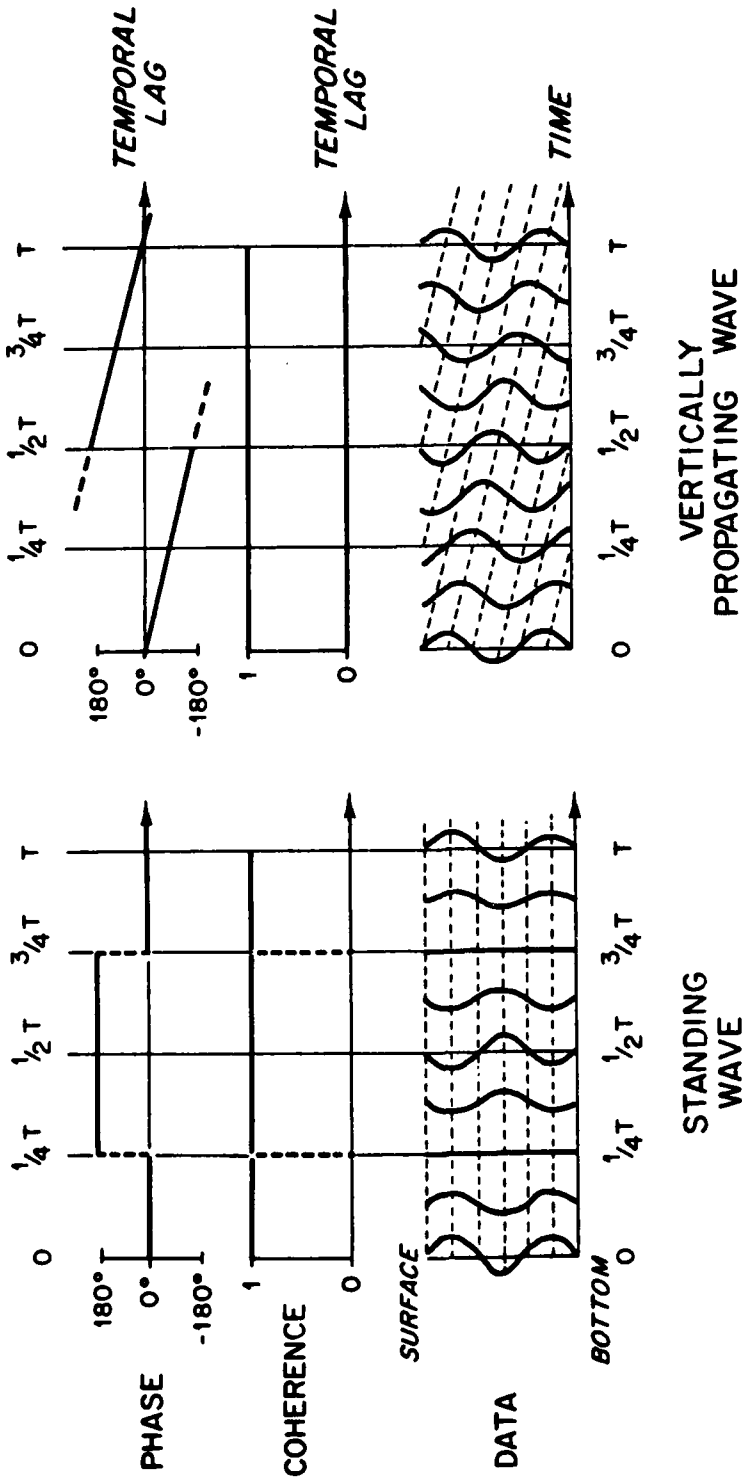


FIGURE II-9

Idealized representations of the way dropped lagged coherence and phase could indicate the presence of vertically standing and propagating waves.

constant value (probably less than unity because of noise, and possibly diminishing with temporal lag due to processes such as dissipation, for example), and phase would be proportional to the time lag, progressing linearly through a full  $360^\circ$  as the temporal lag approached the period length. ( $\phi = \omega t$ , where  $\phi$  is the phase estimate and  $\omega$  is the wave frequency.) The sign of the phase relationship would then indicate the direction of vertical phase propagation.

The absence of coherence or the presence of random phase relations, on the other hand, would indicate that neither of these simple models was appropriate or demonstrable.

Only a restricted range of periods can be inferred from DLC of the 1976 White Horse profiles. There are eight resolvable lags at the equator, to a maximum lag of 19 days, and only six at  $3/4^\circ\text{N}$ , out to 17 days. The gaps between the first and second profiles at each latitude are too large to allow an examination of longer lags. Dropped lagged coherence was computable at  $1.5^\circ\text{N}$  as well, although only four temporal lags are resolvable. The total time span of the series, one month, is too short to resolve reliably periods longer than several months. The total number of profiles at one location and their spacing in time constrains both the number of lags resolvable and the gaps between them and affects the range of elapsed time collected at a single lag, putting a lower limit of several weeks on the periods that might be observed.

In the context of linear equatorial wave theory, the period range of several weeks to several months resolvable using the dropped lagged

coherence estimates means that only Kelvin and mixed Rossby-gravity waves are likely to be detectable using the method on this depth series. Table I-2 showed the maximum period at which inertia-gravity waves can exist for each of the wavelengths resolvable, and the minimum period at which Rossby modes can exist. Only Kelvin and mixed Rossby-gravity waves satisfy the linear dispersion relation in the period range between them: between 15 and 86 days, for example, for a vertical wavelength of 1200sm.

## CHAPTER III - Zonal Velocity

Introduction

The dominant characteristics of the zonal velocity field from these profiles are the persistence with time and latitude of regular features in the vertical structure, and the phase reversal observed between profiles at 1.5°N and 3°N. The approach in this chapter will be to describe and quantify the distribution of zonal kinetic energy with latitude (Section A), to examine relationships between zonal velocity and other variables (Section B), to examine evidence of periodicity in Section C, and to evaluate possible interpretations in terms of linear equatorial wave theory in Section D. Comparison with other results will be made in Chapter V.

Section A. Latitudinal Distribution of Zonal Velocity

A.1. Latitudinal Energy Density. The latitudinal distribution of zonal kinetic energy as a function of vertical wavenumber is shown in Figure III-1a. Four of the curves are labelled by the center wavelength (in stretched meters) of the averaging interval: each point plotted represents an average over five wavenumber bands. The unlabelled curve at the top of the figure is the low-order estimate and represents an average of all wavelengths greater than 1800sm, i.e., the profile mean, all trends, and wavelengths as short as half the examined water column. The error bars on the estimates comprising the labelled curves represent the 95 % confidence interval limits.

A concentration of energy near the equator is evident in the

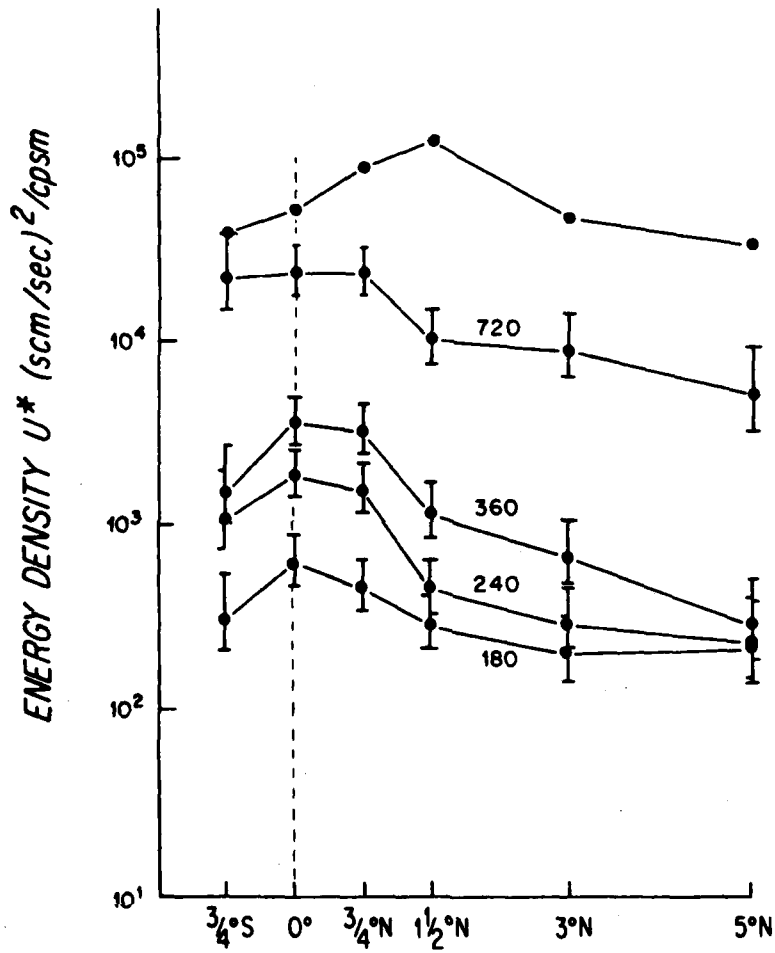


FIGURE III-1a

Autospectral estimates, by latitude, for zonal velocity

shortest wavelength bands and is particularly strong for 240sm. The energy density estimates at the equator and  $1.5^{\circ}\text{N}$  are significantly different from each other for all four wavelength bands presented here, from 720sm through 180sm. Also notice that the estimates for the 720sm and the 360sm band at each latitude are separated by an order of magnitude in energy density. The estimates for 360, 240 and 180sm cluster one and a half orders of magnitude below that for 720sm. Comparison of Figure III-1a with the corresponding figure for the meridional velocity component (Figure IV-1) reveals that both the estimated energy levels and the concentration of energy density at the equator for the horizontal velocity components are not significantly different from each other for the larger wavenumbers examined here: 360, 240 and 180sm. However, the shapes of the curves with latitude and their levels are significantly different (at the 95% confidence level) for the two shortest wavenumber bands, those for a centered wavelength of 720sm and for the low-order estimate (uppermost curve).

Figure III-1b shows the similarly averaged autospectral estimates for the vertical displacement field, by latitude. The pressure wave field for equatorial waves, and thus the displacement field, has no simple structure about the equator, such as the Gaussian velocity structures associated with the Kelvin and mixed Rossby-gravity waves. The patterns here certainly do not indicate equatorial trapping. The estimates for a particular wavenumber band are indistinguishable at the 95% confidence level.

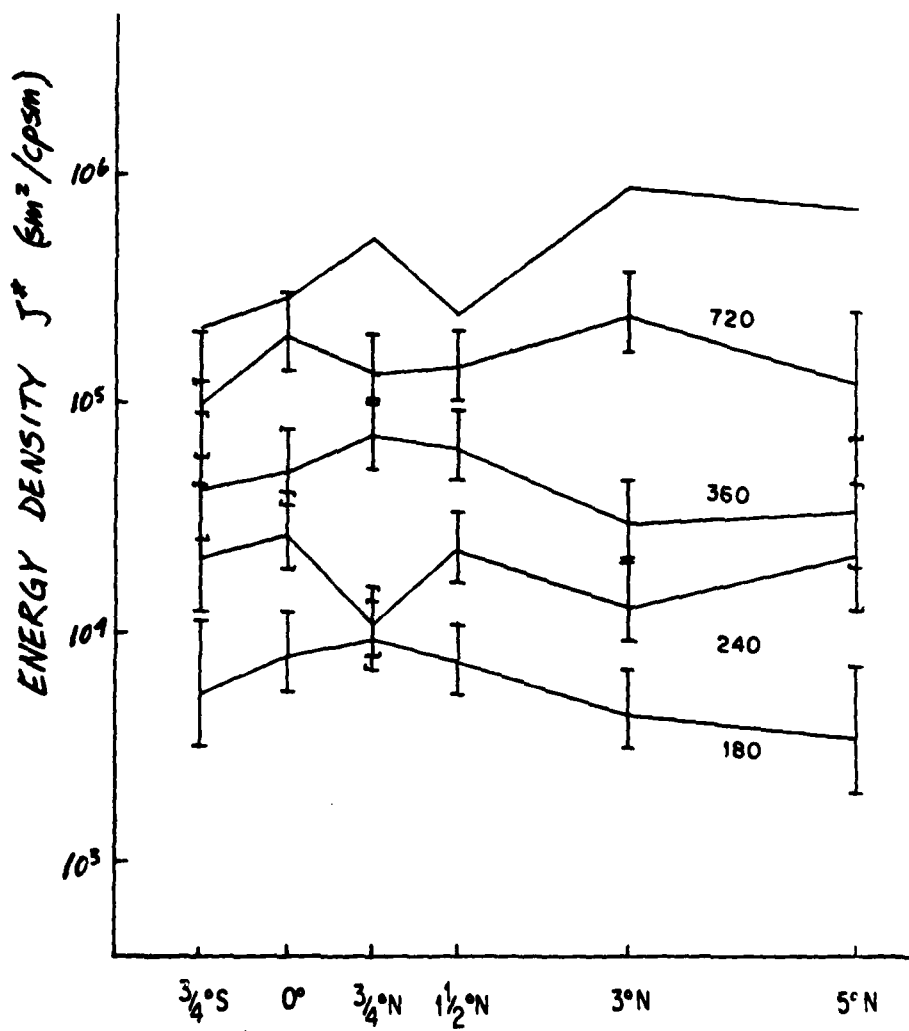


FIGURE III-1b

Autospectral estimates, by latitude, for vertical displacement.

A.2. Latitudinal Profile Sections. Figure III-2 illustrates both the persistence of vertical structure features across the equator and as far off the equator as 1.5°N, and also the striking antisymmetry between the vertical structure of zonal velocity at 1.5° and 3°N. The profile data ( $u$ ,  $u^*$ ,  $\zeta$ , and  $\zeta^*$ ) are taken from latitudinal section #3, spanning June 2 to June 5, 1976. The complete set of latitudinal sections is presented in Appendix A. The equatorial vertical displacement profile is not part of the displacement subset used here, since for this meridional section the CTD data at the equator was incomplete.

A simple measure of the degree of symmetry/antisymmetry between these profiles is

$$\Gamma = \frac{\sum (u_1 + u_2)^2}{\sum u_1^2 + \sum u_2^2}, \quad (1)$$

where  $u_1$  and  $u_2$  are the zonal velocities of two profiles being compared. For a case of antisymmetry, Equation III-1 will yield small values of  $\Gamma$  as one profile reflects into the other: the residual variance is then the variance which cannot be explained by pure reflection. In the opposite case of strong symmetry,  $\Gamma$  will be close to 2.0. A value of one for  $\Gamma$  is thus analogous to a cross-correlation coefficient of zero, indicating that neither symmetry nor antisymmetry dominates, and correspondingly,  $\Gamma = 2$  is similar to  $R_{u_1 u_2} = 1$ ;

$$\Gamma = 0 \Leftrightarrow R_{u_1 u_2} = -1.$$

Computing  $\Gamma$  with the profiles from 3°N and 1.5°N in this manner



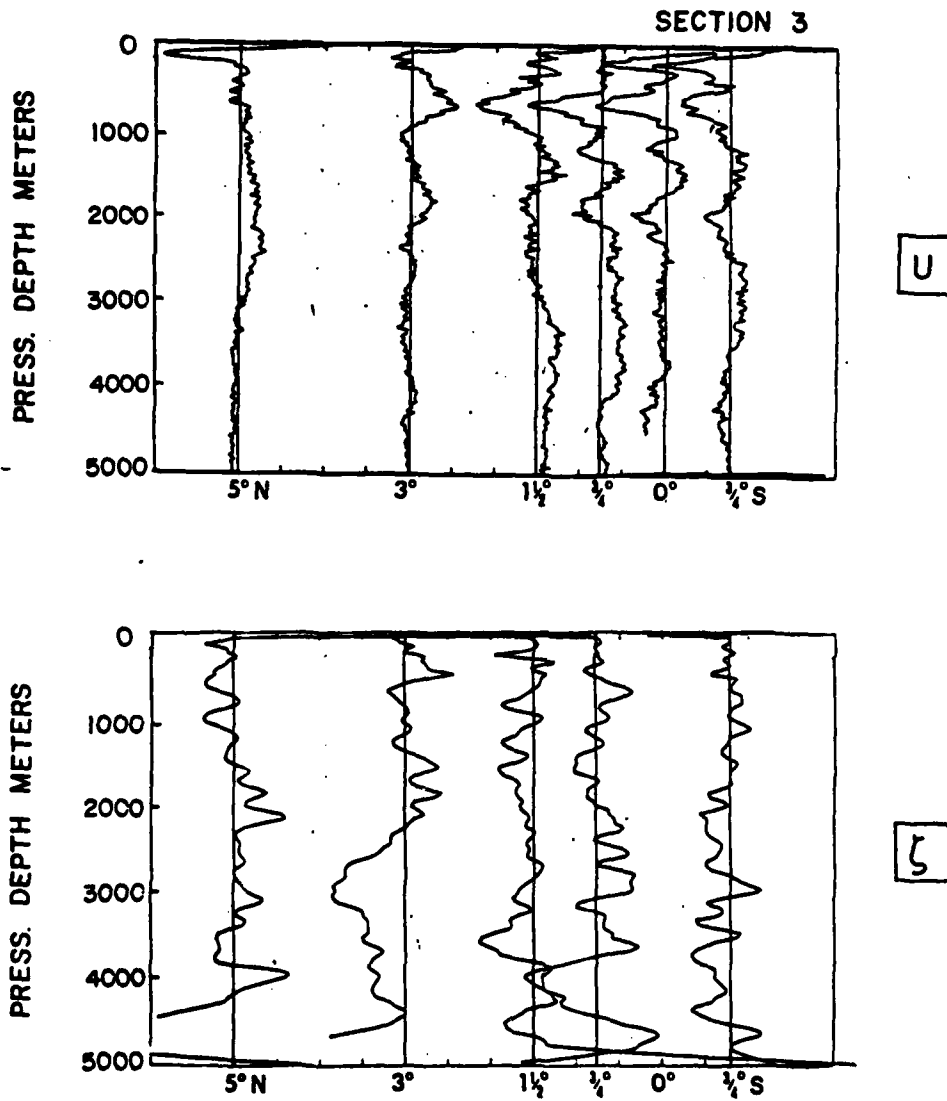


FIGURE III-2a,b

Original profiles of  $u$  and  $\sigma$  from Transect #3.

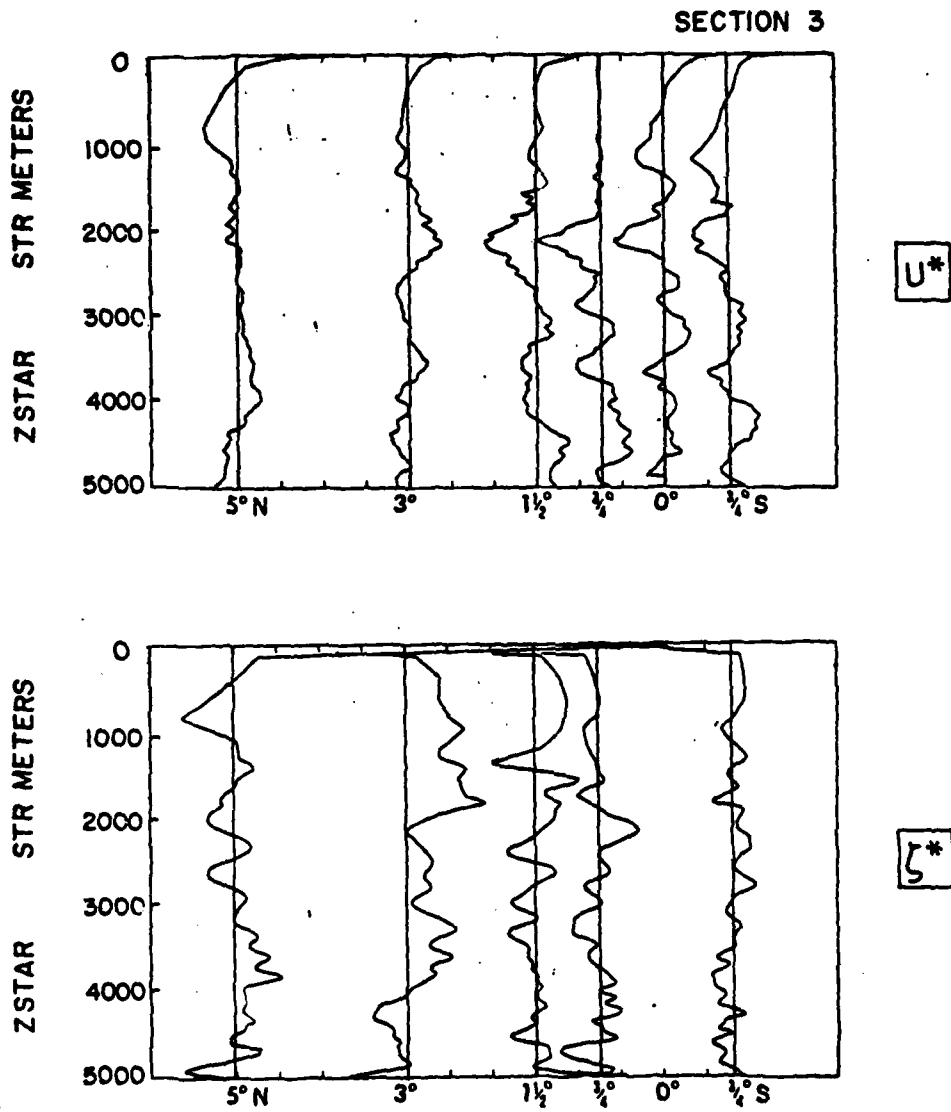


FIGURE III-2c,d

Stretched and normalized profiles of  $u^*$  and  $z^*$  from Transect #3.

(summing over the bottom 3600sm of the stretched water column), gives the result that almost 60% of the variance can be removed by reflection. Neglect of the top 1400sm was discussed in Chapter II-D in relation to the applicability of the WKB approximation implicit in the stretching and normalizing procedure applied to the data. [When the entire stretched water column is employed in the computation of  $\bar{v}$ , the result is that only 24% of the variance is removed. However, as discussed in Chapter II, the upper ocean currents are not well-resolved in the stretching and normalizing procedure: the upper 300m of the water column has been expanded to the upper 1500sm of the stretched water column. In addition, this portion of the water column is expected to be nonlinear.]

Table III-1 presents the results of the computation of Equation III-1 for various profile pairs from meridional section # 3. The upper portion of the table compares profiles whose antisymmetry can be seen visually in Figure III-2. In general, 38-59% of the variance in pairs of profiles spanning 2°N can be explained in terms of antisymmetry. The lower portion of the table indicates the degree of persistence with latitude of structural features in the zonal velocity profiles. From 40-63% of the total variance is removed via subtraction of one profile from another. Note that the least variance is removed when the equatorial profile is compared to a profile one and a half degrees away, a fact related to the shorter vertical scales present at and near the equator (viz. Figure III-1 and the upper part of Figure III-2). Also note that the last line of the table examines the degree of

TABLE III-1: Quantification of symmetry/antisymmetry of zonal velocity profiles with latitude (using bottom 3600sm of each profile unless otherwise noted). All profiles are from latitudinal transect 3.

Location of Profile Combinations		$\frac{1}{2}\sum(u_1')^2$	$\frac{1}{2}\sum(u_2')^2$	$\sum(u_1'+u_2')^2$	$\Gamma$	$R_{u_1u_2}$	$R_{u_1u_2}^2$
(1)	(2)						
antisymmetry							
1.5°N	3°N	59.9	26.9	25.4	.29	-.77	.59
(using total depth)		(49.9)	(26.7)	(40.9)	(.53)	(-.44)	(.24)
3/4°N	3°N	65.4	26.9	30.8	.33	-.76	.58
0°	3°N	42.3	26.9	27.8	.40	-.62	.38
symmetry							
3/4°N	1.5°N	65.4	59.9	223.9	1.79	.79	.63
0°	3/4°N	42.3	65.4	185.3	1.72	.74	.54
0°	1.5°N	42.3	59.9	166.1	1.62	.63	.40
symmetry across equator							
3/4°S	3/4°N	40.8	65.4	181.3	1.71	.73	.53

$$\Gamma = \frac{\sum(u_1'+u_2')^2}{\sum u_1'^2 + \sum u_2'^2}$$

= 2 : perfect symmetry

= 1 : perfect antisymmetry

symmetry across the equator, by comparing the profile at  $3/4^{\circ}\text{S}$  with that at  $3/4^{\circ}\text{N}$ . Symmetry accounts for 58% of the variance, in this case. The important point here is that neighboring profiles that span  $2^{\circ}\text{N}$  are as negatively correlated as the profiles equatorward of  $2^{\circ}$  are positively correlated.

A.3. Variance-preserving net autospectra. The autospectral estimates for zonal velocity of Figure III-1a are presented in greater vertical wavenumber detail in Figure III-3. Each curve is for a particular latitude; all profiles at each latitude along  $53^{\circ}\text{E}$  were averaged together, but no averaging was done over wavenumber bands. The estimates at the equator are averages for ten profiles, and at  $3/4^{\circ}\text{S}$  and  $5^{\circ}\text{N}$  for only three. The format is that known as variance-preserving, since the area under the curve is directly related to the energy in the wavenumber band. The ordinate is energy density times vertical wavenumber, plotted against log wavenumber along the abscissa. This type of spectral representation compensates for the increasing density of spectral estimates per unit log wavenumber and is more accessible to visual inspection. Note that an  $m^{-1}$  spectrum would appear as a straight horizontal line, so that the structure in these plots is a measure of deviation from a (-1)-slope on conventional spectral plots.

The strongest single signal is the peak, significant at the 95% confidence level, for a wavelength of 720sm at the equator and  $3/4^{\circ}\text{N}$ . The secondary peak which appears for 360sm at those two profile stations, but not at  $1.5^{\circ}\text{N}$ , is one explanation for the lower

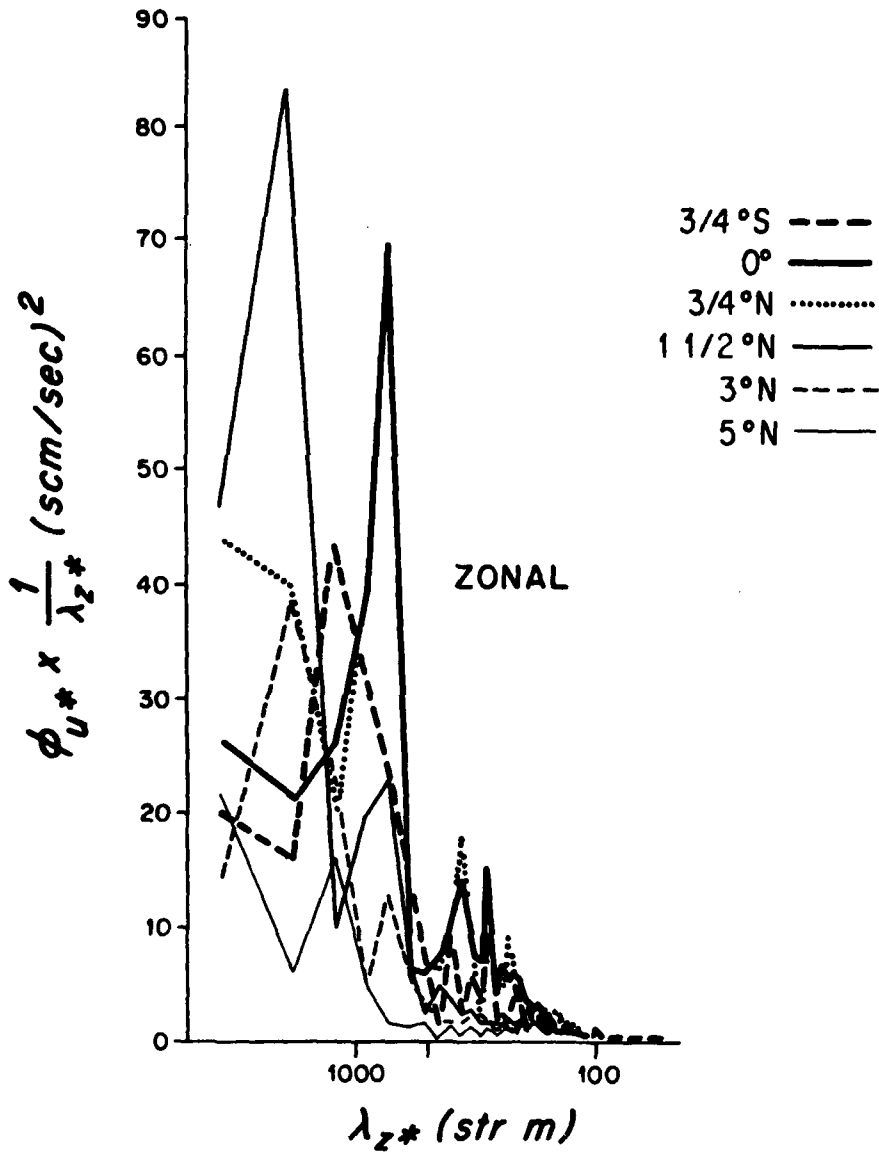


FIGURE III-3

Autospectral estimates of zonal velocity - no averaging.

Each curve represents a different latitude.

correlation, discussed in the previous section, when the profile at the equator is compared to profiles more than one degree from the equator. These peaks for 360sm are significant, as is the peak at the equator for a wavelength of 277sm.

Since the area under these curves represents the energy in each wavenumber band, the "redness" of the zonal velocity spectral estimates is apparent in this figure, and is prevalent at all latitudes examined. For contrast, refer to Figure IV-3, where meridional velocity autospectral estimates are displayed. The dominant feature in that case is the repetition of a peak at 1200sm, a low but not the lowest wavenumber.

When the 3600sm depth series is decremented at the top and bottom, to a 3200sm series, the effect of variations in the discretization of vertical wavelengths can be observed. The major difference in the autospectra is a drop in zonal kinetic energy at a vertical wavelength of 1067sm, relative to 1200sm. At the equator, energy was evenly distributed between 1200 and the adjacent bands, while energy at 1067 is only 20% that in adjacent bands. At  $3/4^{\circ}\text{N}$ , energy at 1200 was 30-70% that in adjacent bands, while energy at 1067 is 5-20% that in neighboring bands. At both latitudes, the trough in zonal kinetic energy at a vertical wavelength of 1067sm is statistically significant at the 95% confidence level.

## Section B. Relationships Between Zonal Velocity and Other Variables.

B.1. General cross-spectral results. Cross-spectral estimates were computed at each latitude for all vertical wavelengths between the

three variables, zonal and meridional velocity and vertical displacement. All significant coherences are listed in Table III-2, which also appears as Table IV-1. Some of the results are discussed in Chapter IV since their implications are primarily regarding the structure of the meridional velocity component

"Significant" is used here and in the following to mean significantly different from zero true coherence at the 95% confidence level. Error bars on the phase estimates indicate the 95% confidence limits. "Leads" is used in the table and the text following to mean leads by  $\pi/2$  with depth (within the error bars at the 95% confidence level). "Out of phase" means a phase estimate of  $\sim 180^\circ$ .

Cross-spectral phase estimates of 0,  $\pi/2$  or  $\pi$  lend themselves to simple interpretation in terms of single equatorial meridional wave modes with particular vertical and meridional structure. Left open in these cases are the questions of zonal and temporal structure. However, phase estimates significantly different from these key values may indicate that either a mix of frequencies is present, obscuring detection of individual wave components, or that the approach is misguided - that the mix in all dimensions is too complex for this attempt at decomposition.

The time series of profiles at the equator and the two northern near-equatorial stations are longer than at the other three stations along  $53^\circ\text{E}$ , so that more reliable statistical estimates are possible there. The energy trapping scales anticipated from linear equatorial wave theory lead one to expect more significant coherence estimates at



VERTICAL WAVELENGTH (sm)	225			$\zeta$ leads u			
	277		u, v out of phase $\zeta$ leads u by $> \pi/2$		$\zeta$ leads u	v leads u	
	300		v leads u	$\zeta$ leads u v leads $\zeta$ by $< \pi/2$			
	327					v leads u	
	360	$\zeta$ leads u by $> \pi/2$		$\zeta$ leads u			v leads $\zeta$ by $> \pi/2$
	400	u, v out of phase	u leads v by $> \pi/2$	u leads v $\zeta$ leads u v, $\zeta$ out of phase		$\zeta$ leads u	
	600			u leads v by $< \pi/2$	$\zeta$ leads u		
	720		v leads u $\zeta$ leads u by $> \pi/2$ $\zeta$ leads v	u, v in phase u, $\zeta$ out of phase $\zeta$ leads v by $> \pi/2$	u leads $\zeta$ by $> \pi/2$	u, $\zeta$ out of phase	
	900		u, $\zeta$ out of phase	u, v in phase $\zeta$ leads u	u, v in phase		u, v in phase
	1200		u, v out of phase	u, v out of phase		u, v in phase u, $\zeta$ out of phase	u, v in phase
1800 sm			u, v in phase $\zeta$ leads u		u, v in phase $\zeta$ leads u by $< \pi/2$ $\zeta, v$ in phase	u, v in phase	
		3/4°S	0°	3/4°N	1.5°	3°	5°N

LATITUDE

TABLE III-2

Three-dimensional tabulation of cross-spectral results

the equator and at  $3/4^\circ\text{N}$ , for the shorter vertical wavelengths. Symmetry relationships between variables mitigate against obtaining elucidating cross-spectral estimates from the equatorial data for linear wave modes, however (see Chapters I-B.2.d and II-D.1). Recall from Table I-1 that the equatorial Rossby radius of deformation is equal to  $3/4^\circ$  for a vertical wavelength of  $\sim 500\text{sm}$ . Consequently, the latitudinal structure of energy at wavelengths much shorter than that is unlikely to be resolved using this data.

B.2. 400sm cross-spectra. A consistent pattern emerges from the cross-spectral estimates for a vertical wavelength of 400sm, however, particularly at  $3/4^\circ\text{N}$ . At that latitude,  $u$  leads  $v$  and  $\zeta$  leads  $u$ , both by  $\pi/2$ , so that  $v$  and  $\zeta$  are  $180^\circ$  out of phase. These phase relationships are consistent with the presence of a mixed Rossby-gravity wave at that vertical wavelength, but the zonal kinetic energy in the 400sm wavelength band is not above the background level (viz. the autospectral estimates in Figure III-3 and the related discussion).

### Section C. Dropped Lagged Coherence Results.

C.1. General. Figure III-4 is a superposition, for the zonal velocity component, of the dropped lagged coherences and phases for each temporal lag resolvable at the equatorial station at  $53^\circ\text{E}$ . The overall pattern is one of high coherence and zero phase estimates at the longer wavelengths. For the shortest vertical wavenumber bands resolvable, the dropped lagged coherence calculations yield significant coherence: for wavelengths of 1800, 900, and 720sm, at least seven of

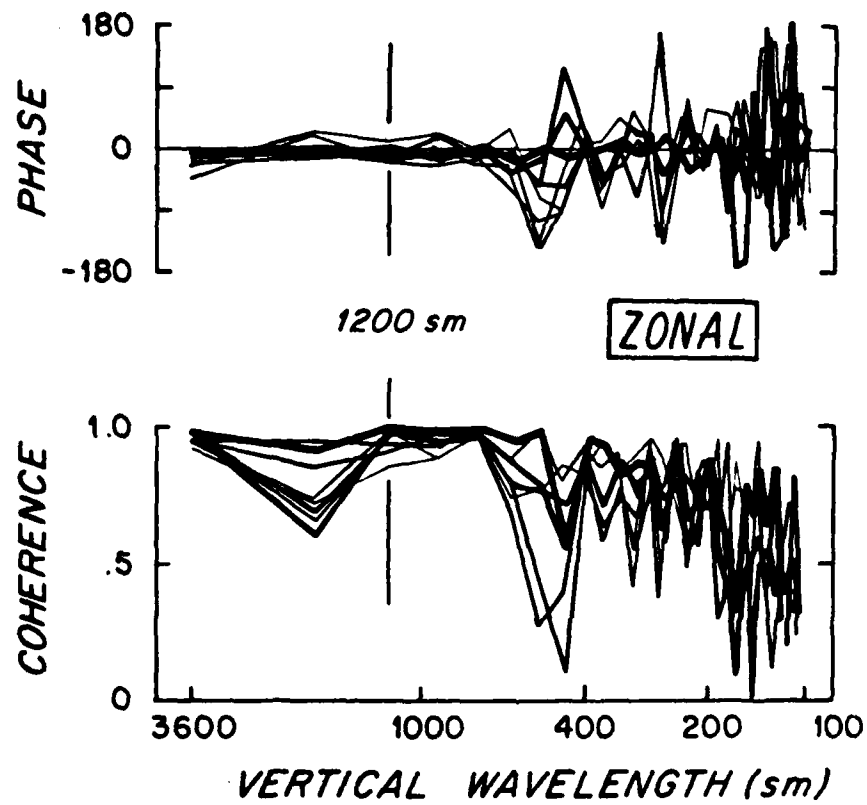


FIGURE III-4

Superposition of DLC for the zonal velocity component at the equator,  
for all temporal lags resolvable.

Key: dark to light corresponds to shorter to longer lags.

the eight resolvable temporal lags at the equator yield coherence estimates significant at the 95% confidence level. At 3/4°N, coherence between the lagged zonal velocity components is also high: significant for 2/3 of the six lags for 1800sm, 5/6 for 1200sm, and at all lags for 720sm. For none of these, however, are the phase estimates significantly different from zero, which, as explained in Chapter II-D.2, might be due to either of two factors: the energy observed at those vertical wavelengths is related to the presence of vertically standing rather than propagating waves, or the energy is due to coherent motion at longer periods than can be resolved with this month-long set of observations.

C.2. 400sm wavelength band. The only vertical wavelength for which the DLC calculations at the equator yield both sufficiently high coherence to be significant and phase estimates which are significantly non-zero is 400sm (Figure III-5). The range of periods which are consistent with the phase change with temporal lag is 105-216 days, with phase propagation upward. At 3/4°N, the 400sm band is coherent for half the temporal lags examined, and two of the phase estimates are nonzero. The phases are uniformly negative, indicating phase propagation in the opposite direction from that at the equator, but encompassing the same period range (47-295 days in this case).

#### Section D. Interpretation and Examination in Terms of Linear Theory.

D.1. Equatorial trapping. The equatorial concentration of zonal kinetic energy in Figure III-1 can be examined in terms of the Rossby radius of deformation ( $L_R$ ). If Kelvin waves dominate the zonal

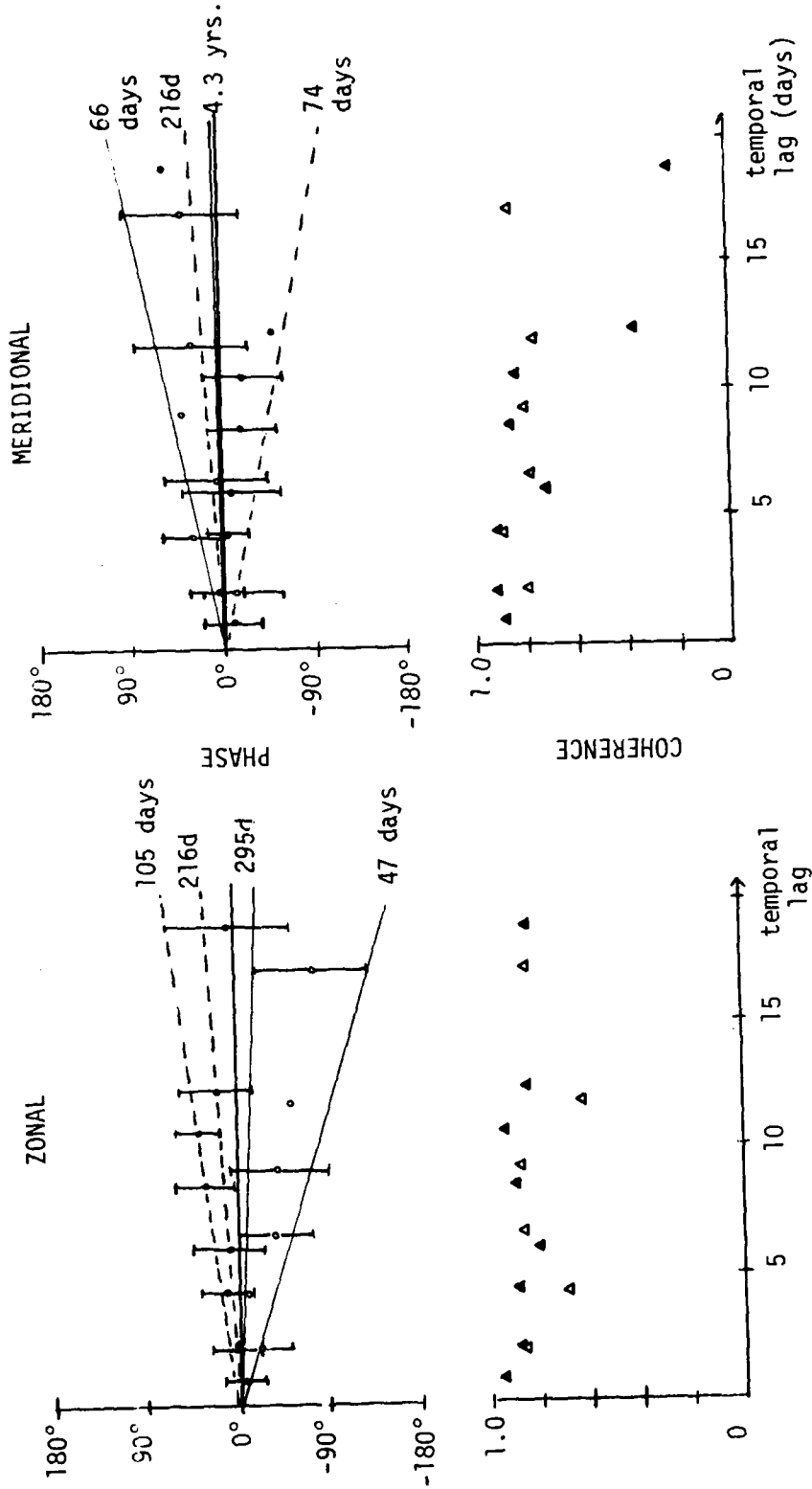


FIGURE III-5  
 Zonal and meridional dropped lagged coherence and phase for a vertical wavelength of 400sm  
 at the equator (closed triangles and circles) and at 3/4°N (open symbols).

velocity field near the equator, the latitudinal distribution of energy will scale with  $L_R$ . Table III-3 contains a comparison of the energy ratios between  $3/4^\circ\text{N}$  and the equator to the ratios consistent with a deformation radius scaling, for the averaged vertical wavelength bands centered at 720, 360, and 240sm, where equatorial intensification appeared strongest. The indication from the table is that Kelvin waves are not dominant at these vertical scales.

Table III-3: Equatorial trapping of zonal velocity

-R (km)	z (sm)	Autospectral estimates		Energy ratios	
		$0^\circ$	$3/4^\circ\text{N}$	$\frac{\text{est. } 3/4^\circ\text{N}}{\text{est. } 0^\circ}$	$e^{-\left(\frac{3/4^\circ\text{N}}{L_R}\right)^2}$
98	720	238(180-340)	236(179-339)	.99	.48
69	360	36(28-50)	33(25-46)	.92	.24
56	240	19(14.5-26)	15.5(12-22)	.82	.11

( ) : indicates 95 confidence limits.

D.2. Evaluation of latitudinal symmetry/antisymmetry. The strongest signals from visual inspection of the 1976 White Horse profiles are 1) the temporal persistence of vertical structures in the zonal velocity component, at the equator in particular (see Appendix B), and 2) the combination of symmetry across the equator and antisymmetry between the profiles at  $3^\circ\text{N}$  and the near-equatorial profiles, including the profiles at  $1.5^\circ\text{N}$ . There were six latitudinal transects made along  $53^\circ\text{E}$  in 1976 which include the station at  $3^\circ\text{N}$ , shown as Sections 2 through 7 in Appendix A. Figure III-2 illustrated

the phenomena. An explanation, first proposed by Carl Wunsch (1977), which is consistent with this latitudinal structure of zonal velocity as well as with the steadiness with time mentioned as point 1) above, is the presence of a first meridional mode long Rossby wave.

Only two and a half weeks elapsed between the first and the last of these six transects, so that it is not surprising that no significant phase differences at depth with time can be detected by examining the latitudinal sections. Consequently, the periodicity of a vertically standing or propagating wave cannot be determined directly from the data. However, the strongest zonal velocity signal in the ~400-day series of current meter data from the western equatorial Indian Ocean in 1979-1980 is for a 180-day period oscillation (Luyten and Roemmich, 1982). That period will be used as an estimate to examine consistency relations, since the 1976 data indicates that the oscillation is of much longer period than the length of this time series, and since a lot of energy is input at that frequency into the Indian Ocean (Knox, 1976; McPhaden, 1982). Note that if a periodic function is responsible for the observed signal, then increasing the period length beyond the semi-annual which will be used here would increase the zonal wavelength, according to linear theory, but would have little impact upon either the turning latitude or the radius of deformation, and thus would have little effect upon the latitudinal structure of the zonal velocity field.

Before a detailed interpretation, the visual and statistical evidence for the presence of strong antisymmetry will be discussed more

thoroughly than in Section III-A. All six of the latitudinal transects extending to 3°N display the same antisymmetry between the profiles at 1.5°N and 3°N. With vertical profiles, which constitute snapshots of the water column, one is limited by the number of realizations possible in the vertical. Using spectral techniques, for example, one cannot discern the differences in energy between the longest vertical scales (lowest vertical modes).

The scale of the zonal signal in this data is a significant portion of the observed water column, so that most standard statistical approaches are not going to be reliable in quantifying the picture. As a result, the measure  $\Gamma$  was devised in Section III-A, and used to examine the strength of the similarities and dissimilarities between pairs of profiles, by summing them at each depth. The equatorial profiles were included there only for completeness, since the vertical structure at the equator is visibly more complex than that at 3°N, for example, a fact consistent with the general expectation, from equatorial theory, of the nature of equatorial trapping, and also consistent with the spectral estimates presented by latitude in Figure III-1.

No similar antisymmetry is seen in the series of White Horse profiles collected in the western equatorial Pacific Ocean in 1978 (Eriksen, 1981). The latitudinal distribution and level of zonal kinetic energy observed in the two series are indistinguishable, however, and a fuller comparison of the two sets of observations is found in Chapter V.



Table III-4 sets forth some of the relevant consistency checks possible between the data and a first meridional mode long Rossby wave of, for this comparison, six-month period. The primary points of comparison are thus the zonal scale of the phenomenon, the latitudes where a  $180^\circ$  phase reversal occurs, and the relative amplitudes of the features at various latitudinal locations. The zonal scale cannot be resolved from the 1976 data: Figure III-6 shows pairs of near-simultaneous profiles from the two equatorial stations, at  $50^\circ 30'E$  and  $53^\circ E$ . Two weeks elapsed between each pair, and there are no clear phase differences with longitude, or with time. The former indicates that the zonal scale is much longer than the separation between the stations and the latter is consistent with a period, if any, of at least six months, i.e., six times the elapsed time between the first and last of the profiles at each station.

The second point of comparison is the latitude of phase reversal, which in the data occurs somewhere between the stations at  $1.5^\circ N$  and

TABLE III-4

---

$\lambda_2$	<u>1500sm</u>	<u>1800sm</u>
1) $L_R$	141km(1.28°)	154km(1.40°)
2) $y_T$	244km(2.31°)	267km(2.43°)
3) $\lambda_x$	2245km	2716km
4) nodes: u	1.55°	1.70°
5) amplitude retention of u from $0^\circ$ to (a) $3/4^\circ$	.74	.78
(b) $1.5^\circ$	.13	.27
(c) $3^\circ$	.11	.10

---

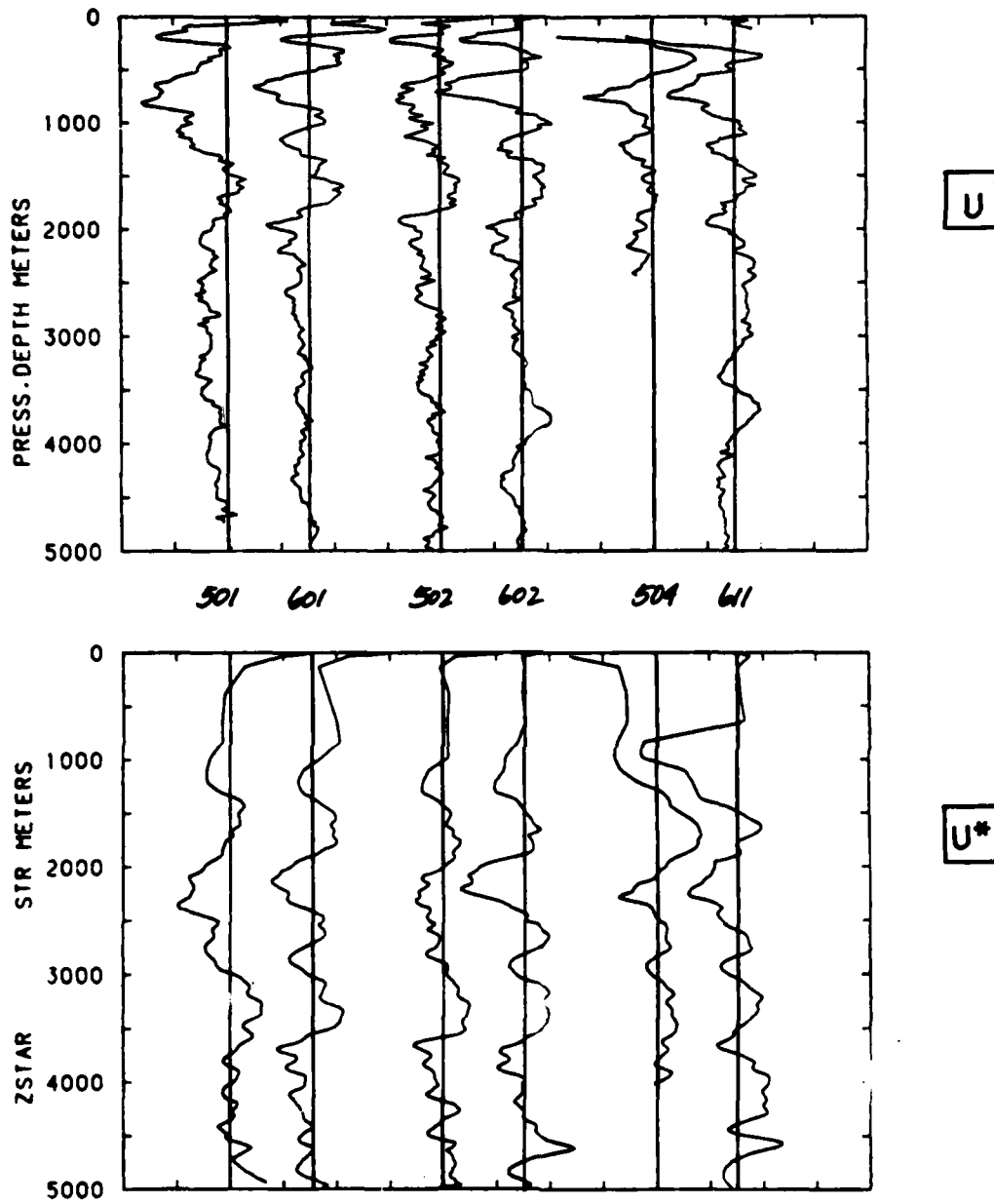


FIGURE III-6  
Comparison of profiles at the equator,  $50^{\circ}30'E$  and  $53^{\circ}E$

3°N. An estimate of 1500sm for the vertical wavelength gives a theoretical reversal location just to the north of the first station, while an estimate of 1800sm pushes that location 17km further towards 2°N.

The third point of comparison is the amplitude decay of the zonal velocity associated with a first mode Rossby wave from its primary maximum at the equator. Reference to Table III-4 indicates that this is where the major discrepancy in this interpretation arises. Amplitudes at the equator and 3/4° away would be very similar, as would amplitudes at 1.5° and 3°, particularly for a vertical wavelength of 1500sm. The data does not indicate the jump in relative amplitude between these pairs of latitudes, however. A 90% decrease in amplitude between the equator and 3°N would incline one to the view that a feature observable at the equator would not be manifest at 3°N.

It thus seems unlikely that the antisymmetry across 2°N is due to the presence of a linear first meridional mode Rossby wave. The possibility that a higher odd meridional mode Rossby wave is responsible is unlikely because a node in the zonal velocity field would be expected between 3/4°N and 1.5°N, although the relative amplitudes would remain higher in that case. Among other explanations are the possibility that the WKB approximation is becoming less valid for the longer vertical scales, or that linear theory is not applicable to this particular feature of the vertical structure. In addition, the full impact of the 45° slant of the western boundary of the Indian Ocean upon the velocity field is not known. Moore (personal

communication) has shown that a tilt of the western boundary alters the symmetry properties of the reflection. The reflection of a first mode long Rossby wave, for example, requires a mixed Rossby-gravity wave, of opposite meridional symmetry, to satisfy the boundary condition, in addition to a Kelvin and a short first mode Rossby wave. The relative distribution of energy shifts in favor of the mixed wave as the tilt of the coast to the east increases.

## CHAPTER IV - Meridional Velocity

Introduction

The meridional velocity component in general reveals both shorter vertical length scales and shorter temporal scales of variability than the zonal component. The approach in this chapter will be to describe and discuss information obtained from the White Horse profiles, by means of standard auto- (Section A) and cross-spectral calculations (Section B) and also by means of dropped lagged coherence and phase estimates (Section C). Interpretation of these results, and their evaluation in terms of linear equatorial wave theory, will comprise Section D.

Section A. Latitudinal Distribution of Meridional Velocity

A.1. Latitudinal energy density. The latitudinal distribution of meridional kinetic energy density over various vertical wavenumber bands is condensed into Figure IV-1. Each point represents autospectral density at a particular latitude averaged over five adjacent wavenumber bands. A concentration of energy at the equator is clearly visible at all but the lowest wavenumber estimates, and is particularly strong for the wavenumber bands centered at 360 and 240sm. Note that there were only three profiles made at  $3/4^{\circ}\text{S}$ , so that the spectral estimates for that latitude have larger error bars and less statistical reliability than the other near-equatorial locations. The estimate at  $1.5^{\circ}\text{N}$  is statistically lower than that at the equator, at the 95% confidence level, for the 720, 360, and 240sm bands, and

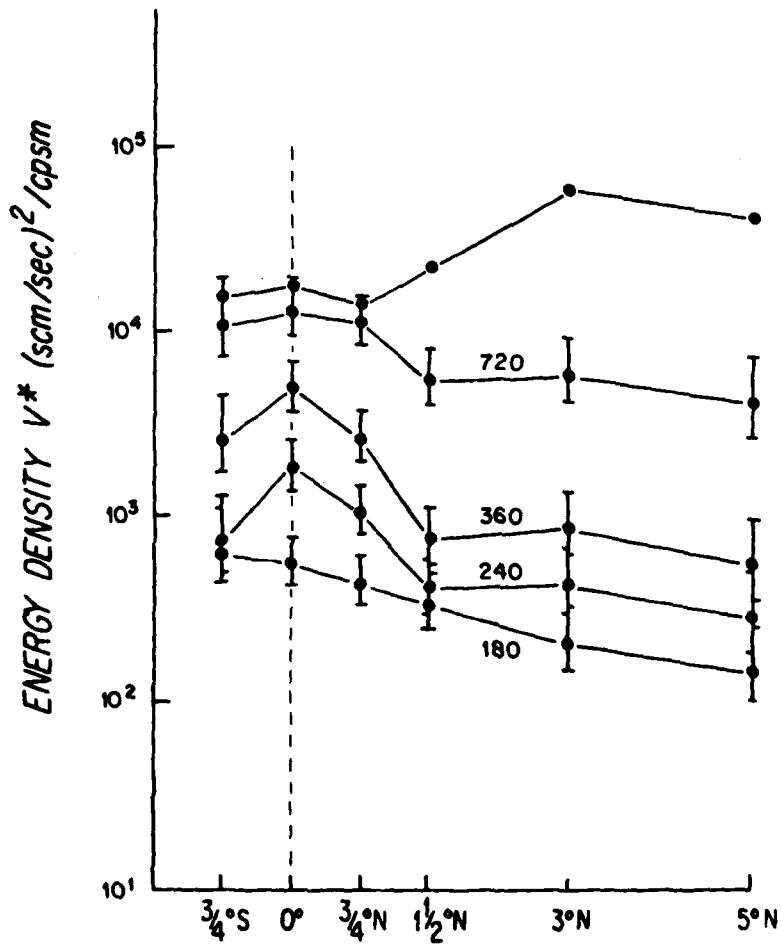


FIGURE IV-1

Autospectra of stretched and normalized meridional velocity, averaged over five wavenumber bands, presented as a function of latitude, from 3/4°S to 5°N.

spectral energy density seems to level off to a stable "background" level at that latitude. The energy concentration and its scales will be examined analytically in Section D.

The behavior of the 180sm band, where energy concentration is apparently less intense, may be an indication that the estimates are approaching the noise level of the stretched and scaled measurements. It was mentioned in Chapter II that the maximum stretched interval between data points was 63sm in the depth interval used for the spectral calculations, so that the shortest resolvable wavelength would be twice that. However, since for this dataset only two transponders generally were available for the triangulation calculation (see Chapter II-A), the noise level in  $v$  may be higher than the wave energy at wavelengths somewhat longer than 130sm. In addition, the adaptive filter described in Chapter II-C, which is used to smooth the stretched profiles, smooths the lower part of the water column over as much as 150sm.

A.2. Latitudinal profile sections. The latitudinal structure of meridional velocity profiles along  $53^{\circ}\text{E}$  is shown in the time series of meridional sections, extending from  $5^{\circ}\text{N}$  to  $3/4^{\circ}\text{S}$ , that forms Appendix A. The variability of vertical structure with latitude which was evident in the above autospectra (Figure IV-1) is clear in the profiles.

A transect from the middle part of the time series, section #4, is shown in Figure IV-2. Both straight ( $v$  in cm/sec) and stretched ( $v^*$  in scm/sec) velocity profiles are presented. Individual features can sometimes be tracked between the equatorial and near-equatorial

## SECTION 4

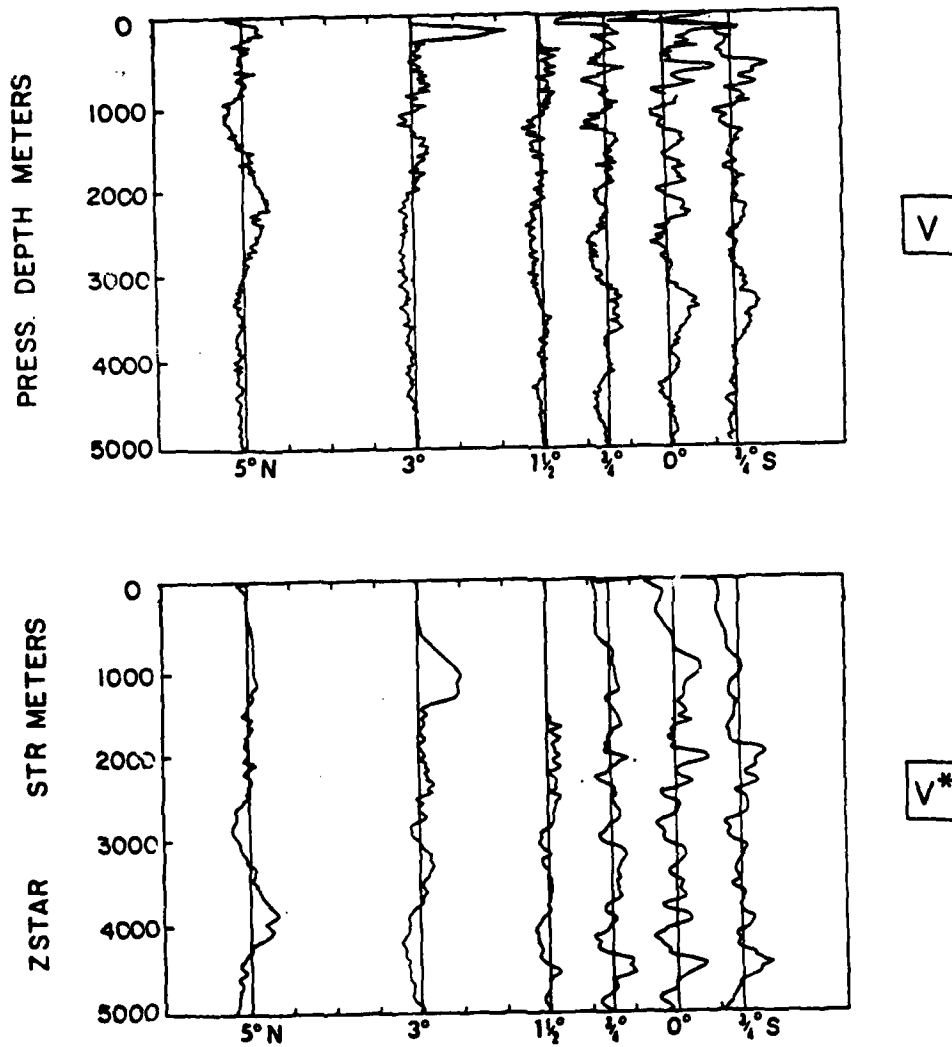


FIGURE IV-2

Profiles of meridional velocity along 53°E, from 3/4°S to 5°N, presented in both original form and after WKB stretching and normalizing. The meridional section shown is transect 4 from Appendix A.



profiles, but usually not as far as  $1.5^{\circ}\text{N}$ , although this visual approach can be deceptive. The decrease in vertical structure away from the equator, i. e., the increase in dominant vertical scale, is very clear.

A.3. Variance-preserving Net Autospectra. Figure IV-3 presents the autospectral estimates of Figure IV-1 in greater vertical wavenumber detail. All profiles at a particular latitude were averaged, but there was no averaging over wavenumbers. The format is that known as variance-preserving, since the area under the curve is directly related to the energy in the wavenumber band. The ordinate is energy density times vertical wavenumber, plotted against log wavenumber along the abscissa.

A general decrease in energy away from the equator is evident at all but the lowest wavenumbers. A peak is apparent at 1200sm, which gradually decreases in strength away from the equator to  $1.5^{\circ}\text{N}$ , where it is distinguishable primarily because of the abrupt decrease in level at 900sm. A secondary peak at 600sm at  $3/4^{\circ}\text{N}$  and S is broader at the equator, where there is approximately the same energy density at 720sm. Troughs appear at 900sm and at 514sm at the three equatorial and near-equatorial stations, giving the peak between them more significance than if it occurred at a single latitude. A broad peak at 400-450sm occurs at the same three stations. The other strong feature is a peak at 257sm, which occurs only at the equator.

Although the peak at 1200sm is somewhat misleading in that only at the equator does this band contain more energy than the bands on either

AD-A113 565

WOODS HOLE OCEANOGRAPHIC INSTITUTION MA  
OBSERVATIONS OF VERTICALLY PROPAGATING EQUATORIALLY-TRAPPED WAVES--ETC(U)

F/G 8/3

MAR 82 K O'NEILL

N00014-76-C-0197

NL

UNCLASSIFIED

WHOI-82-11

2 of 2

40 A  
113568


END  
DATE  
FILMED  
05-82  
DTIC

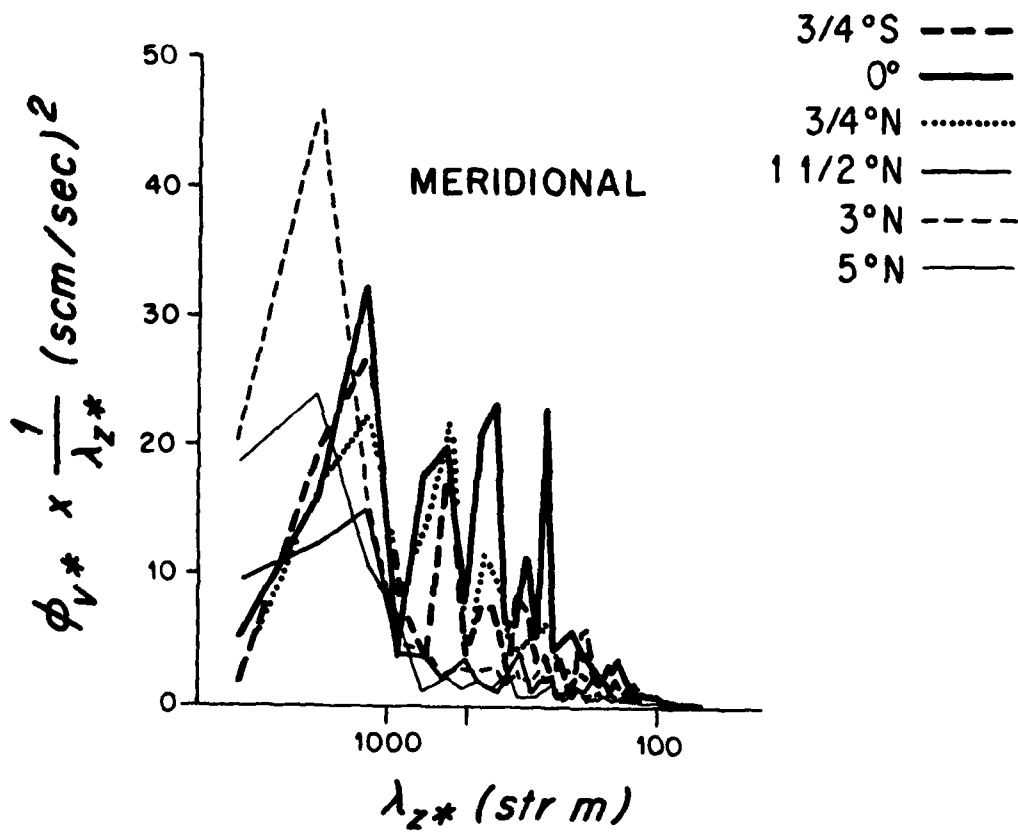


FIGURE IV-3

Autospetra of stretched and normalized meridional velocity ( $v^*$ ), with no wavenumber averaging, presented for each net as a function of vertical wavenumber.

side, at all four latitudes ( $3/4^{\circ}\text{S}$  to  $1.5^{\circ}\text{N}$ ) the 1200sm band is more energetic than the adjacent higher wavenumber band, centered at 900sm. Examination of the zonal kinetic energy spectra (Figure III-3) reveals a trough rather than a peak at 1200sm, at the equator,  $3/4^{\circ}\text{N}$  and  $1.5^{\circ}\text{N}$ . At each of these latitudes, the meridional component is slightly more energetic than the zonal, but in no case is the difference statistically significant.

The meridional spectral energy at 450sm is approximately twice the zonal energy at both the equator and  $3/4^{\circ}\text{N}$ . For both velocity components, there is slightly more energy in the 400sm band than in the 450sm band, which is also the case for zonal kinetic energy at  $3/4^{\circ}\text{N}$ . However, meridional energy is significantly greater at 450sm than at 514sm at both latitudes.

#### Section B. Cross-spectra

Coherence between stretched variables is low in general. Significant coherence is found predominantly at lower wavenumbers. Appendix C shows all significant coherences at each latitude between the three variables ( $u, v, \zeta$ ), with no averaging in wavenumber space (Table C-1). "Significant" is used here and in the following to mean significantly different from zero true coherence at the 95% confidence level. Error bars on the phase estimates indicate the 95% confidence limits.

Relationships which can be gleaned by examining coherence at the same location in unaveraged bands are presented in Table IV-1. "Leads" is used in the table and the text following to mean leads by  $\pi/2$  with

VERTICAL WAVELENGTH (m)

225			c leads u			
277		u, v out of phase c leads u by $> \pi/2$		c leads u	v leads u	
300		v leads u	c leads u v leads c by $< \pi/2$			
327					v leads u	
360	c leads u by $> \pi/2$		c leads u			v leads c by $> \pi/2$
400	u, v out of phase	u leads v by $> \pi/2$	u leads v c leads u v, c out of phase		c leads u	
600			u leads v by $< \pi/2$	c leads u		
720		v leads u c leads u by $> \pi/2$ c leads v	u, v in phase u, c out of phase c leads v by $> \pi/2$	u leads c by $> \pi/2$	u, c out of phase	
900		u, c out of phase	u, v in phase c leads u	u, v in phase		u, v in phase
1200		u, v out of phase	u, v out of phase		u, v in phase u, c out of phase	u, v in phase
1800 m			u, v in phase c leads u		u, v in phase c leads u by $< \pi/2$ c, v in phase	u, v in phase
	3/4°S	0°	3/4°N	1.5°	3°	5°N

LATITUDE

TABLE IV-1

Cross-spectra of all three variables ( $u^*$ ,  $v^*$ ,  $\zeta^*$ ), presented as functions of latitude and vertical wavenumber, with no wavenumber averaging. All significant coherence pairs are presented, with their phase estimates. The same information is contained in Table 1 of Appendix C, and this figure is repeated from Figure III-4.

depth (within the error bars at the 95 % confidence level). "Out of phase" means a phase estimate of  $\sim 180^\circ$ .

When the cross-spectral estimates are averaged over "two" wavenumber bands, only 5 % of the coherences between meridional velocity and the other two variables are significant at the 95 % confidence level. Since a 95 % confidence level means that 5 % of the estimates of zero true coherence will appear significantly different from zero, this reduction in coherence implies that the coherent processes have narrow vertical wavenumber bandwidths. Table 2 in Appendix C shows all significant coherence pairs between the three variables when the estimates are averaged over "two" adjacent wavenumber bands, equivalent to weights of 1/4, 1/2, and 1/4 about the center band, so that adjacent estimates are not independent.

The following discussions will focus primarily upon cross-spectral relations in the wavenumber bands where dropped lagged coherence (to be discussed in Section C) has shown a strong indication of periodicity. Bands adjacent to these primary ones are scanned to see how broad the relationships are in wavenumber space.

B.2. 1200sm wavelength cross-spectra. Examining coherence in the 1200sm band between orthogonal velocity components from profiles at the same location, one sees significant coherence at the equator in the 1200sm band and also in the adjacent 900sm band. The phase relation is not stable, being indistinguishable from  $180^\circ$  at 1200sm and from  $-90^\circ$  at 900 sm, in the latter case indicating  $u$  leads  $v$  with increasing depth. At  $3/4^\circ N$ , the velocity components are coherent over a broad

wavenumber range, from wavenumber bands centered between 600 and 1800sm. At 1200sm the phase estimate is close to  $-180^\circ$  ( $-139^\circ \pm 30^\circ$ ), while in the neighboring bands the phase is indistinguishable from zero.

Assuming independence of the profiles in the subset for which displacement at the equator is available, the only significant coherence for the 1200sm band is between velocity components; neither velocity component is coherent with displacement. The phase estimate between  $u$  and  $v$  for the subset is  $170^\circ \pm 27^\circ$ , indistinguishable from that for the full set of profiles. Coherence in adjacent bands is limited to vertical displacement-zonal velocity at 900sm, although all three variables are coherent at 720sm, with displacement leading both  $u$  and  $v$ .

At  $3/4^\circ\text{N}$  for the 1200sm band, again only the velocity components are coherent. The phase estimate for the displacement subset is  $-147^\circ \pm 29^\circ$ , compared to  $-139^\circ \pm 30^\circ$  when all drops are used. There is an indication (not statistically significant) that displacement leads zonal velocity in this band, as it does in the bands to each side, where coherence is significant. [At 1800sm,  $.82(90^\circ \pm 29^\circ)$ ; at 1200sm,  $.55(61^\circ \pm 180^\circ)$ ; at 900sm,  $.71(122^\circ \pm 43^\circ)$ , compared to the coherence cutoff of  $.67$ ]. There is no other coherent relationship between variables at 1800sm, and at 900sm the other phase relations between variables are not distinguishable from zero, although coherence is significant.

B.3. 450sm wavelength cross-spectra. By contrast with the 1200sm wavelength behavior, the cross-spectra between velocity components show no coherence in the 450sm band, at either the equator or  $3/4^\circ\text{N}$ . The

adjacent longer wavelength band is also not coherent, but at both latitudes the 400sm band shows significant coherence, with a phase estimate of  $-133 \pm 22^\circ$  at the equator and  $-88 \pm 35^\circ$  at  $3/4^\circ\text{N}$  (both indicating  $u$  leads  $v$ ).

None of the cross-spectra between velocity components and displacement shows coherence at 450sm at either the equator or  $3/4^\circ\text{N}$ . The same holds for 514sm, the adjacent higher wavelength band. At 400sm, however, the coherence and phase estimates between velocity components for each subset agree with the above. In addition, at  $3/4^\circ\text{N}$  displacement at a 400sm wavelength is coherent with both velocity components. Phase estimates indicate displacement leads  $u$  ( $96 \pm 33^\circ$ ) and that  $v$  and displacement are out of phase. Displacement is not coherent with either velocity component at the equator in the 400sm band, although the coherence amplitude between  $u$  and displacement is sufficiently high (.71 versus cutoff of .73) to give a phase estimate significantly different from zero, and consistent with that calculated at  $3/4^\circ\text{N}$  ( $83 \pm 54^\circ$ ).

### Section C. Dropped Lagged Coherence (DLC) Results

C.1. General. Several dominant features emerge from the DLC analysis. In contrast to a mid-latitude spectral model of internal waves at low wavenumber (GM76: Desaubies, 1976), it is clear that these equatorial dropped lagged coherence estimates are a function of vertical wavenumber. In general, pairs of the zonal velocity component show high coherence for the longest resolvable vertical wavelength



bands at all three latitudes for which there are enough velocity profiles to use the temporal lag approach: at the equator,  $3/4^{\circ}\text{N}$  and  $1.5^{\circ}\text{N}$ ,  $53^{\circ}\text{E}$ . For the meridional component, the opposite is true. Coherence is reduced for the lowest vertical wavenumbers, and in general is not significant. Consequently, the high coherence for the meridional component in the 1200 stretched meter band is prominent, as is shown in Figure IV-4. Examination of the corresponding phase estimates for evidence of periodicity reveals a strong signal in the 1200sm band for the meridional velocity. There is in general more evidence of periodicity for the meridional component than for the zonal, and stronger evidence of periodicity at the equator than away from it.

These general results are consistent with first impressions from examination of the original unstretched data: a shorter-term temporal variability evident in the north-south velocity component in sharp contrast to the persistence of features in the east-west component during the time span covered by the profiles, and a tendency toward shorter vertical scales in the meridional velocity component compared to the zonal.

C.2. DLC at 1200sm. At a vertical wavelength of 1200sm, the meridional components are coherent at the equator and at  $3/4^{\circ}\text{N}$ . The adjacent bands are not coherent. Steadily decreasing phase with longer temporal lag is observed, indicating phase propagation downward. (See the discussion of Figure II-9 for the interpretation of DLC phase in terms of propagating waves.) At the equator, the meridional component

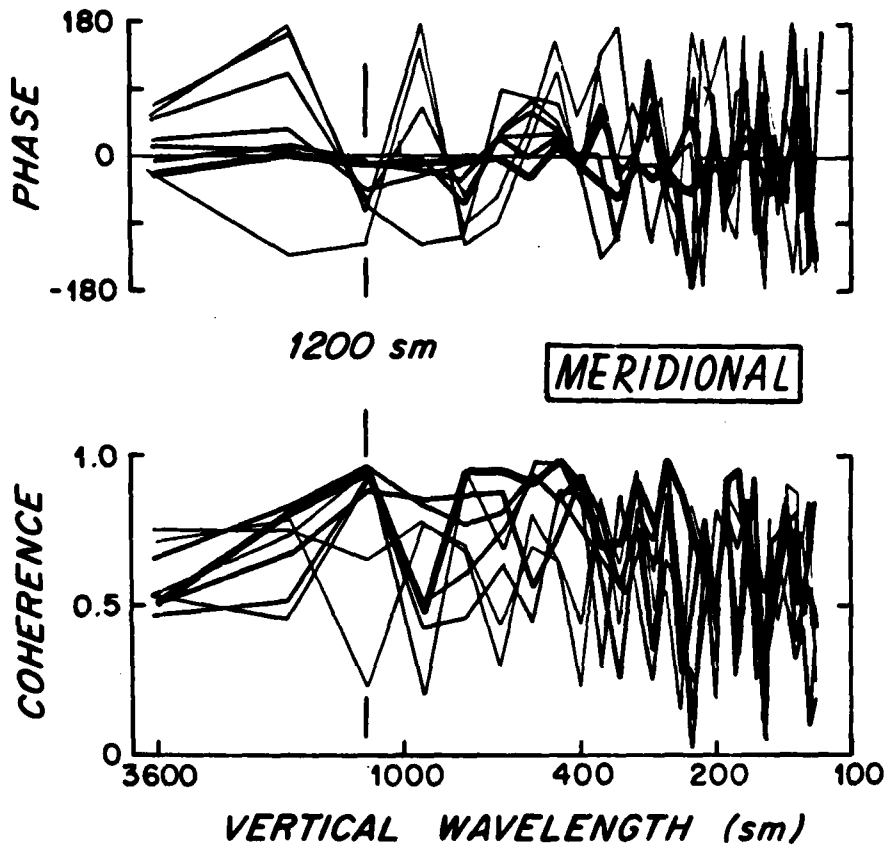


FIGURE IV-4.

Superposition of dropped lagged coherence and phase for the meridional velocity component at net 6, 0°, 53°E. All eight resolvable temporal lags are presented, from 1 day to 19 days. The consistent high coherence for the 1200sm band is clear for the first six lags; the steady decrease in the phase estimates is apparent through the longest lag. The darkest curves are for the shortest lags, and vice versa. The same information is presented in different form for the 1200sm band in Figure IV-5; for 450sm in Figure IV-6; and for 720sm in Figure IV-7.

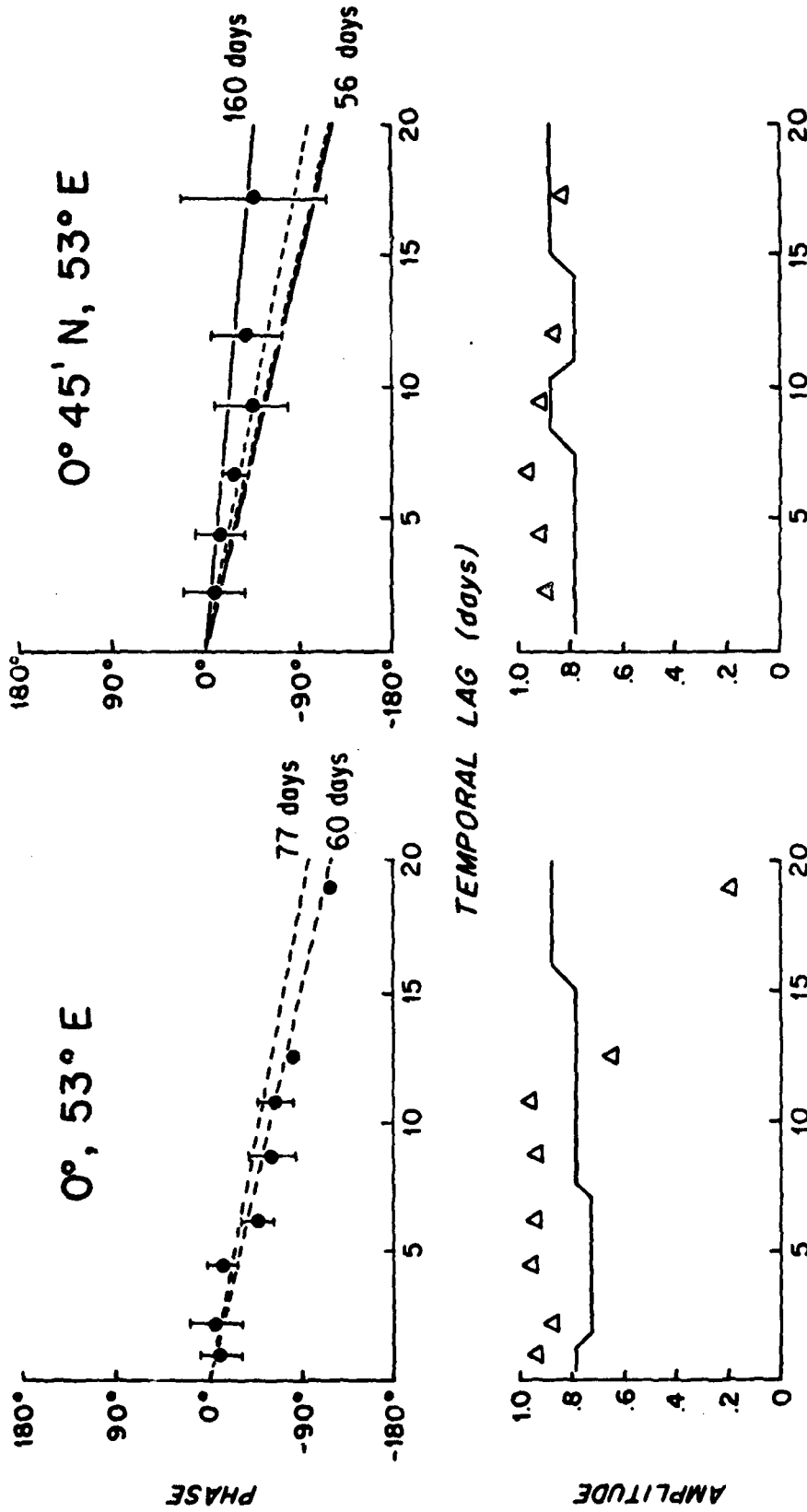


FIGURE IV-5

Dropped lagged coherence and phase for the meridional velocity component at 53°E, 0° and 3/4°N, presented as functions of temporal lag, for the 1200sm vertical wavelength band. The cone which defines the inferred range of periodicity is indicated by cross-hatching.

is coherent at six of the eight temporal lags, with three of the phase estimates non-zero at the 95 % confidence level. At  $3/4^{\circ}\text{N}$ , five of six lags are coherent, with three of the phase estimates significantly different from zero. See Figure IV-5.

Using 95 % error bars on meridional phase estimates to compute period ranges, at the equator one obtains a range of 60-77 days; at  $3/4^{\circ}\text{N}$ , 57-161 days. A linear least-squares fit to the phase estimates at both latitudes yields a joint estimate of 72 days, whether all phase estimates are used or only those for which the coherence was significant.

Dropped lagged coherence was also computed at  $1.5^{\circ}\text{N}$ , where only four temporal lags were resolvable. The meridional velocity component is coherent through ten days there, and the phase estimates are increasingly negative, although not significantly different from zero.

It should be noted that at all three latitudes ( $0^{\circ}$ ,  $3/4^{\circ}\text{N}$ ,  $1.5^{\circ}\text{N}$ ) where dropped lagged coherences could be computed, the phase estimate for the meridional component in the 1200sm band continues to decrease at a steady rate, even when the coherence estimate is no longer significantly different from zero.

The best estimate for the periodic signal in the DLC results for a wavelength of 1200sm is 72 days, from the above. For reference, recall that the minimum Rossby wave period at this vertical wavelength is 86 days; the maximum inertia-gravity period is 15 days. (These limits were derived in Chapter I-B.2, for Table I-2). For the second meridional mode, the minimum Rossby wave period is 112 days, maximum

inertia-gravity 11. Only Kelvin and mixed Rossby-gravity waves satisfy the linear dispersion relation between the maximum inertia-gravity and the minimum Rossby wave periods. A Kelvin mode is not relevant here since the signal appears in the meridional velocity component, at and near the equator.

C.3. DLC for 450sm. Strong evidence of periodicity is also found in the dropped lagged coherences for the 450sm wavelength band. At the equator, coherence is significantly different from zero for aggregated pairs of meridional velocity through temporal lags of eleven days; for five of these six estimates, the phase is also significantly different from zero. For the next longer lag, 12.5 days, coherence is slightly below the cutoff but the phase estimate is still significantly different from zero and consistent with those preceding it. The inferred propagation direction is the reverse of that for the 1200sm band: in this case, phase is steadily increasing with temporal lag, indicating phase propagation upwards, with the second of each pair leading the first. The meridional DLC at  $3/4^{\circ}\text{N}$  yields phase estimates that are consistent through temporal lags of 9 days with those at the equator, but only two of the six coherence estimates are significant and their significance is borderline (.81, .79 for cutoff .79). See Figure IV-6.

When 95% error bars on the meridional phase estimates are used to compute a period range for the equatorial data, the result is 47-72 days. A linear fit to the phase estimates for which coherence is significant yields a period estimate of 57 days. (For reference, the

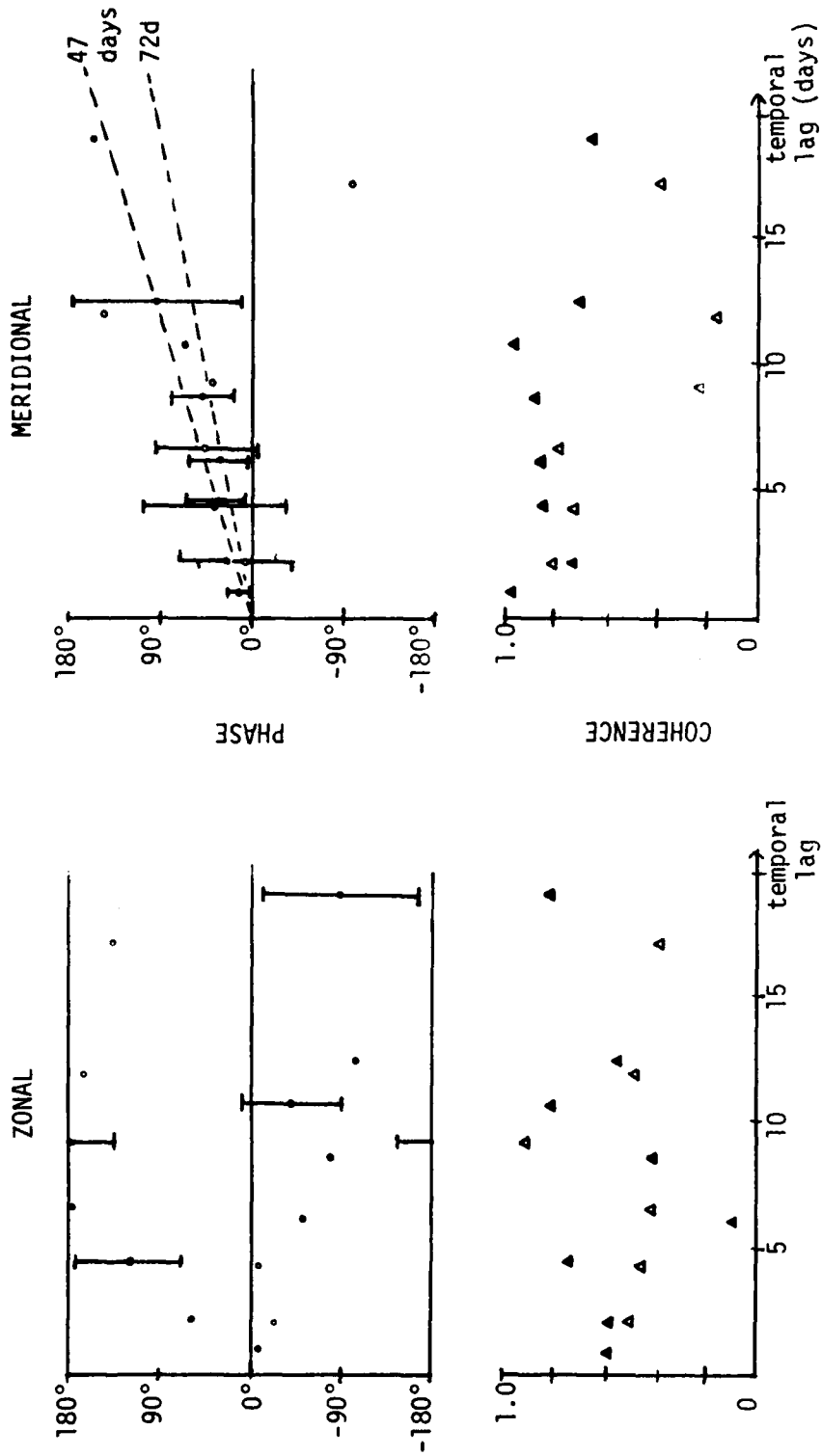


FIGURE IV-6  
Zonal and meridional dropped lagged coherence and phase for a vertical wavelength of 450sm at the equator (closed triangles and circles) and at 3/4°N (open symbols).

minimum Rossby wave period for this vertical wavelength is 141 days; the maximum inertial-gravity is 24 days.)

The adjacent longer wavelength band, centered at 514sm, is less coherent meridionally at the equator and phase estimates do not progress uniformly. The phase estimates are included within the error bars of the estimates at 450sm, however, and three of eight are significantly different from zero. The adjacent shorter band, centered at 400sm, shows coherence over the same temporal lags as the 450sm band, but no phase estimates are non-zero. There is no coherence meridionally at  $3/4^{\circ}\text{N}$  in the 514sm band, and although some coherence is found in the 400sm band, phases are indistinguishable from zero.

C.4. DLC for 720sm band. A third wavenumber band where the meridional dropped lagged coherences indicate some periodicity is centered on 720sm. Coherence is significant for half the eight lag groups at the equator and two of the corresponding phases are significantly different from zero, so that a period range of 31-44 days can be computed from the 95% error bars on the phase estimates. The phase estimates are consistently negative, indicating phase propagation downward. Four of the six coherence estimates are significant at  $3/4^{\circ}\text{N}$ . The phase estimates are uniformly negative, decreasing regularly with increasing lag, and again two of the phase estimates are significantly non-zero. They indicate a somewhat longer period of 80 days, with the range being 52-254 days, so that the two sets of period estimates do not overlap (Figure IV-7).

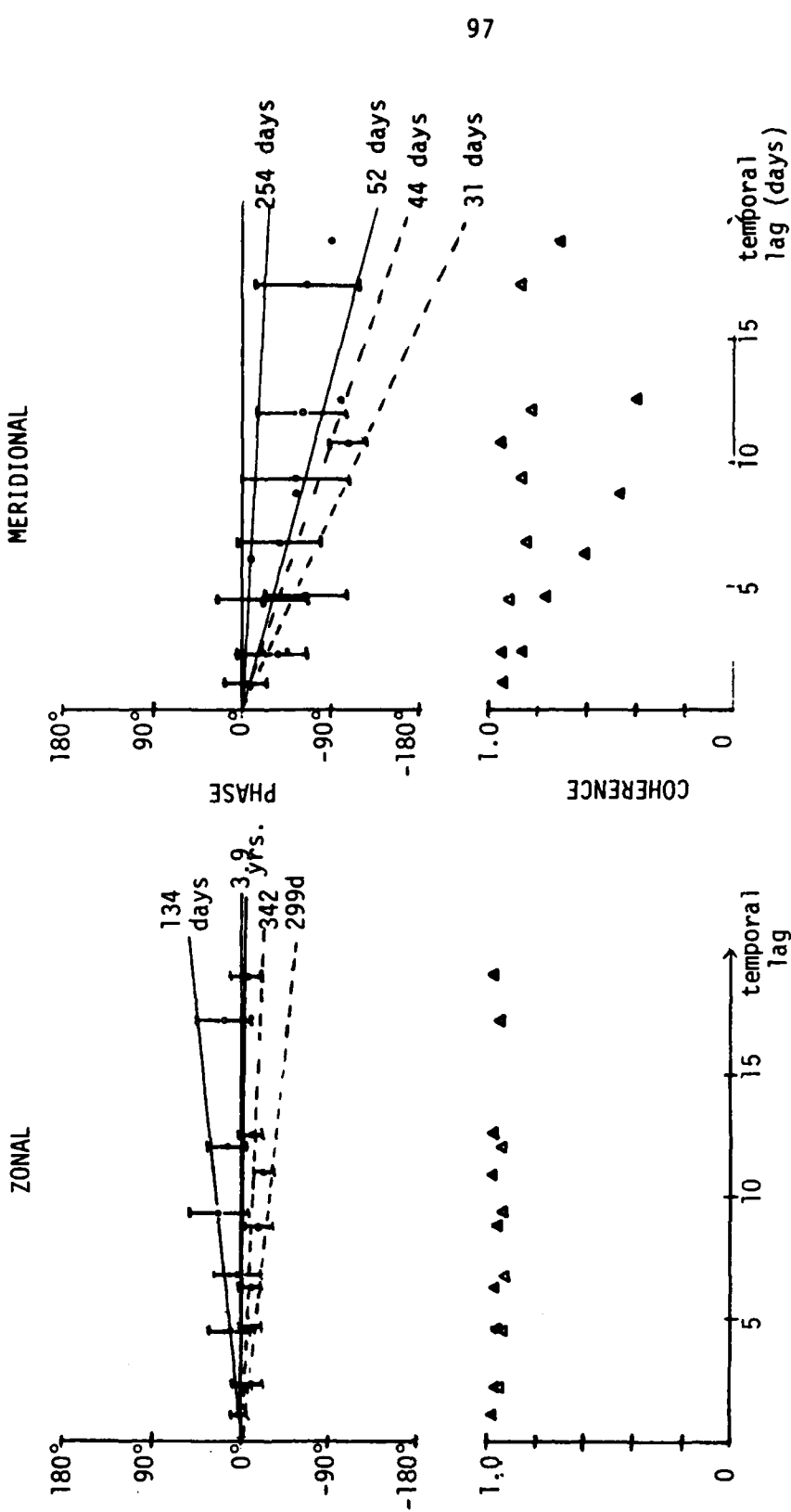


FIGURE IV-7  
 Zonal and meridional dropped lagged coherence and phase for a vertical wavelength of 720sm at the equator (closed triangles and circles) and at 3/4°N (open symbols).



## Section D. Interpretation and Examination in Terms of Linear Theory

D.1. Equatorial trapping. As shown in Chapter I, the latitudinal structure of the dominant velocity component of the two gravest equatorially-trapped meridional modes is a Gaussian centered at the equator. For a Kelvin wave ( $n=-1$ ), the only velocity component is the zonal; for a mixed Rossby-gravity wave ( $n=0$ ), meridional velocity has the same structure as  $u$  for a Kelvin and the off-equatorial maxima of zonal velocity (which has a node at the equator) are of lower amplitude than the meridional component.

The latitude  $[(N_0/\beta |m|)^{1/2}]$  at which the kinetic energy of the Gaussian velocity component falls to one-third its equatorial value is less than  $3/4^\circ$  for vertical wavelengths less than 514sm (see Table I-1, equatorial Rossby radius of deformation). Consequently, the latitudinal structure of Kelvin and mixed Rossby-gravity waves with vertical wavelengths less than 500sm, if they are present, cannot be well-resolved with this data set. Cross-spectral phase relations, in particular, are likely to be dominated by noise at short vertical wavelengths, since the equator is the location for a node in one of the velocity components.

In light of the above, the equatorial concentration of meridional kinetic energy evident in Figure IV-1 can be examined to see if the Rossby radius is the appropriate scaling, that is, whether the concentration of energy is consistent with the presence of mixed Rossby-gravity waves. Table IV-2 shows a comparison of energy density off the equator to the equatorial values.

TABLE IV-2.  
Equatorial trapping of meridional velocity

$L_R$ (km)	$\lambda_z$ (sm)	Autospectral estimates		Energy ratios			
		0°	3/4°N	$\frac{\text{est. } 3/4^\circ\text{N}}{\text{est. } 0^\circ}$	$\frac{\text{low } 3/4^\circ\text{N}}{\text{high } 0^\circ}$	$e^{-\left(\frac{3/4^\circ}{L_R}\right)^2}$	$\frac{\text{adj. } 3/4^\circ\text{N}}{\text{adj. } 0^\circ}$
98	720	129(97-180)	118(87-155)	.91	.48	.48	(.24)
69	360	51(38-70)	27(20-38)	.54	.29	.24	(.19)
56	240	19(14.5-26)	11(8.2-15)	.57	.31	.11	(.18)
		1.5°N		$\frac{\text{est. } 1.5^\circ\text{N}}{\text{est. } 0^\circ}$	$\frac{\text{low } 1.5^\circ\text{N}}{\text{high } 0^\circ}$	$e^{-\left(\frac{1.5^\circ}{L_R}\right)^2}$	$\frac{\text{adj. } 1.5^\circ\text{N}}{\text{adj. } 0^\circ}$
98	720		57	.44		.06	
69	360		8	.15		.003	
56	240		4.2	.22		.0002	

( ): 95% confidence limits

adj.: estimate at 1.5°N subtracted from numerator and denominator before division.

Column 7 is the proportion of equatorial energy that would be present at  $3/4^\circ$  off the equator if the Rossby radius is the controlling latitudinal scale factor. Column 5 is the quotient of the spectral estimates at  $3/4^\circ$  and  $S$  and  $0^\circ$ , and column 6 shows the minimum ratio, produced when the lower bound on the estimates at  $3/4^\circ$  and the upper bound at  $0^\circ$  are used. The upper and lower bounds are the confidence limits at 95%. Comparing columns 5 and 7, one can see that the actual energy decrease is slower than the Gaussian, although when the extremes at 95% confidence are used (column 6), energy in the 720sm band decreases to  $3/4^\circ N$  according to the Gaussian. Energy in the 360sm band falls off somewhat more slowly, and in the 240sm band is almost three times as large as the Gaussian model.

The lower part of the table concerns the estimates at  $1.5^\circ N$  and it is clear that no amount of manipulation will extract agreement with a Gaussian decrease in energy. However, if the apparent leveling off at  $1.5^\circ N$  is taken into account and the spectral estimates at that latitude are considered as background levels, they can be subtracted from the equatorial and near-equatorial estimates (see column 8). Energy at 360sm falls off well within the predicted model, and at 240sm is closer to the prediction. The latitudinal distribution of meridional kinetic energy in the 720, 360 and 240sm wavelength bands is thus consistent with the presence of mixed Rossby-gravity waves at those vertical wavelengths.

The spectral estimates discussed above have been averaged over five adjacent wavenumbers, but standard coherence and phase (Section B) and

dropped lagged coherence and phase (Section C) indicated significant behavior in individual wavenumber bands. In particular, it would be interesting to be able to explain the structure of the peaks in the autospectra shown in Section A. These attributes of the data will be synthesized in the following sections.

D.2. Interpretation of spectral behavior for the 1200 m wavelength band. Since the indication of temporal periodicity at a vertical wavelength of 1200m is solely in the meridional component, a tentative identification of a mixed Rossby-gravity wave can be made, based primarily upon the period estimate from the equator, which is more tightly defined than that at  $3/4^\circ\text{N}$  and for which no other even meridional modes are possible with real zonal wavenumber. Choosing a plane in the three-dimensional  $(m, k, \omega)$  dispersion relation (Equation I-10) based on this vertical wavenumber, and cutting that plane at this frequency range, one obtains a zonal wavelength of 300-400km when the meridional mode number is zero. See Figure I-6. Since the signal is in  $v$  at the equator, only even meridional modes  $[n=0,2,4,\dots]$  need be considered. For  $n > 0$ , the dispersion relation yields a complex zonal wavenumber, deemed to be unrealizable considering the distance of the profile station from the African coast (D. Moore, personal communication). The period estimate from  $3/4^\circ\text{N}$  overlaps that at the equator, but, being broader, also admits the possibility of the second meridional Rossby mode. The e-folding distance for mixed Rossby-gravity wave meridional kinetic energy at this vertical wavelength is 126km, i.e., energy decay to 65% at  $3/4^\circ$ , 18% at  $1.5^\circ$ .

The turning latitude for a second mode Rossby wave is 280km.

[ $y_T = ((2n+1)N_0/\beta m)^{1/2}$ .] The fact that the period signal occurs in the meridional velocity component at the equator rules out a Kelvin or first Rossby mode being responsible.

The analysis of the White Horse profiles can be presented as an information matrix. The interpretation problem is then reduced to the finding of a coherent solution consistent with the various elements. The matrix components are the autospectra of the three variables, [1] $_u$ , [2] $_v$ , [3] $_s$ ; the dropped lagged cross-spectra of [4] $_{u*u}$ , [5] $_{v*v}$  (the number of displacement profiles is insufficient to compute DLC for  $s$ ); and the more standard cross-spectra of [6] $_{u*v}$ , [7] $_{u*s}$ , and [8] $_{v*s}$ .

In the context of linear equatorial wave theory, a testable hypothesis generated from [5], the DLC for  $v$ , is the presence of a mixed Rossby-gravity wave of 1200sm vertical wavelength, with downward phase propagation and slightly longer than two-month period. At the equator, zero zonal velocity and vertical displacement are associated with such a wave (i.e., both variables have a node at the equator), and to the north of the equator,  $v$  and  $s$  would be in phase, leading  $u$  by  $\pi/2$  with depth. Examination of [2], meridional kinetic energy at a wavelength of 1200sm, as a function of latitude indicates the e-folding distance from the equator is broader than the predicted Gaussian. There is a falloff, however, as well as evidence that the apparently slow rate might be attributable to a high background level. Examination of [4], DLC for  $u$ , reveals that no periodicity can be directly ascribed to the zonal velocity component: the high coherence

and near zero phase estimates are compatible with the presence of a long-period standing wave, with a period greater than 80 days, or of a propagating wave of longer period. External evidence (from current meters set in 1976 and 1979) indicates a general concentration of zonal kinetic energy at periods greater than two months (Luyten, 1982), and, in particular, a highly energetic vertically propagating signal of semi-annual period, with a vertical wavelength of the order of the ocean depth (Luyten and Roemmich, 1982). Attenuation with depth due to weak reflections from the north-south boundaries might yield an energy distribution over the longest resolvable vertical scales, when analyzed by means of vertical profiles, consistent with the high DIC coherence [4] as well as the energy level [1] in those bands (Luyten, personal communication).

The absence of coherence between vertical displacement and the velocity components ([7] and [8]) off the equator is consistent with the fact that the calculation of  $\xi$  is a noisy one and also with the relatively low amplitudes of  $u$  and  $v$  for a mixed Rossby-gravity wave of this period. Although the ratio  $u^2/v^2$  increases with increasing latitude for a mixed Rossby-gravity wave (5% at  $3/4^\circ$ , 21% at  $1.5^\circ$ , for a 72-day period at this vertical wavelength), the ratio  $v^2/v^2(0^\circ)$  falls so quickly (to 18% by  $1.5^\circ$ ) that any zonal velocity signal would be lost in the noise. Displacement for a mixed Rossby-gravity wave follows the same pattern as does the zonal component.

The cross-spectra of velocity components [6] seem to provide the major discrepancy for this interpretation, since they indicate that  $u$  and  $v$  are coherent and  $180^\circ$  out of phase at both the equator and  $3/4^\circ\text{N}$ , rather than the expected lack of coherence at the equator and  $90^\circ$  phase difference off the equator. Additional information with respect to the average phase difference between the components seems to support the decoupling interpretation of zonal energy above, however. When the complete series of profiles are considered in shorter groups and cross-spectra are computed (shown below in Table IV-3), the phase difference is seen to be a function of time.

TABLE IV-3: UV Cross-spectra

	equator		$3/4^\circ\text{N}$	
	coherence	phase[ $^\circ$ ]	coherence	phase[ $^\circ$ ]
all profiles	.84(.59)	$161 \pm 20$	.75(.59)	$-139 \pm 30$
early	.84(.79)	$-139 \pm 40$ u leads	.77(.79)	$-115 \pm 56$ u leads
middle	.87(.73)	$170 \pm 27$	.82(.67)	$-147 \pm 29$ u leads
late	.98(.79)	$156 \pm 12$ v leads	.97(.79)	$-174 \pm 15$ u leads

( ): 95 % cutoff level for true coherence significantly different from zero.  
 $\pm$  : 95 % confidence interval on phase estimates.

Consider the  $n$ th harmonic of two series,  $u_n = a \cos(2\pi k_n z + \alpha_n)$  and  $v_n = b \cos(2\pi k_n z + \beta_n)$ .  $\theta_n (= \beta_n - \alpha_n)$  is then the average phase lead of  $v_n$  over  $u_n$  with depth and  $\theta_n = f(t)$  implies that  $\beta_n$  and/or  $\alpha_n$  are some functions of time. Let  $\beta_n = -2\omega t + c_1$ ,  $\alpha_n = -\omega t + c_2$ ; then  $\theta_n = -\omega t + c_3$ . Over an elapsed time of  $\Delta t = \frac{1}{10} \frac{2\pi}{\omega}$ , say, one-tenth the period of the longer-period wave, the average phase difference will

change by  $30^\circ$  and in the observed direction, if the wave frequencies are related as above.

The choice of frequencies in the above analysis is deliberate, with one frequency twice that of the other. The 1976 White Horse profiles, analyzed by means of dropped lagged cross-spectra, indicate a temporal periodicity in the meridional velocity component of two to three months. The 1979-80 current meter measurements indicate a vertically-propagating wave in the zonal velocity component with a period of six months. Although the observed coherence amplitude and phase estimates for a vertical wavelength of 1200sm cannot be explained by the presence of a single mixed Rossby-gravity wave, an infinite sum of wave solutions is not required as an explanation. Two wave forms will suffice.

The apparent inconsistency in an interpretation of the 1200sm signal in energy and period as indicating the presence of a mixed Rossby-gravity wave may instead be evidence of the simultaneous presence of a longer-period wave, with energy predominantly in the zonal velocity component. Such an ad hoc approach neglects some major dynamical questions, however, among them linearity and energy sources.

The validity of the assumption of linearity must be considered. Neglect of the advective terms in the momentum equation requires that the phase speed be large compared to both the mean flow and the perturbation particle speeds. At a vertical wavelength of 1200sm for a mixed Rossby-gravity wave, the linear dispersion relation yields a zonal wavelength of -404km (phase propagation westward) at a period of



60 days, or a zonal wavelength of  $\sim 316$  km at a period of 72 days. The respective zonal phase velocities are  $-7.8$  and  $-5.1$  cm/sec, which are to be compared to rms amplitudes from the spectral decomposition of the velocity profiles of  $\sim 3.0$  cm/sec at the equator for this wavenumber band. It is clear from the ratio  $u/c$  that nonlinear effects may not be completely negligible. It is not clear what their impact might be on a mixed Rossby-gravity wave. Evaluation of the mean flow, in order to compare its magnitude with these phase speeds, is difficult to do from the profiles. Although the individual profile means are all of order 1-2 stretched centimeters per second, critical levels may exist at various depths. These questions will be topics for future research, but will not be pursued further here.

A third consideration involves the penetration of energy to depth. For a linear Kelvin or mixed Rossby-gravity wave, the ratio of zonal to vertical group velocities is  $N_0/\text{wave frequency}$ , exactly, where  $N_0$  is the buoyancy frequency used to stretch and normalize the original velocity profiles and thus represents the ambient density structure. For a mixed Rossby-gravity wave of 60-day period, this ratio yields propagation of one and a half kilometers zonally for one stretched meter vertically. For longer periods, the angle from the horizontal at which energy would propagate is even smaller.

The correct interpretation of the dropped lagged coherence results is that phase propagation is downward (profiles earlier in time lead subsequent profiles), implying a deep rather than surface energy source. Source possibilities include reflection from a smooth bottom

or bottom topographic features, since reflection from the African coast requires preservation of frequency, and no westward-propagating (i.e., incoming to the African coast) linear equatorial waves have real zonal wavenumbers for this frequency and vertical structure.

It should be noted that the inferred zonal energy propagation direction, i.e., eastward, has been based exclusively upon the assumption of a mixed Rossby-gravity wave from the period fit. There is no direct evidence regarding zonal structure or propagation. However, the zonal antisymmetry which is apparent in Figure IV-8 for  $v$  and  $v^*$  offers indirect evidence of a zonal wavelength approximately twice the station separation. The figure shows three pairs of velocity profiles: all of the profiles are from the equator, and the pairs were collected at approximately two week intervals. The first profile in each pair is from  $0^\circ, 50^\circ 30'E$ ; the second is from  $0^\circ, 53^\circ E$ , so that the profiles are taken from longitudes  $\sim 275\text{km}$  apart. Statistical resolution of the associated vertical length scale is complicated by the fact that too few profiles exist from the station nearest the African coast for sufficient degrees of freedom. A vertical length scale of much less than  $1200\text{sm}$  is apparent, which may be superimposed upon a longer vertical scale oscillation.

D.3. Interpretation of spectral behavior in the 450sm wavelength band. The DLC results also showed a strong signal at 450sm. In the framework of linear equatorial wave theory, at a scale of 450sm only a mixed Rossby-gravity wave displays the observed periodicity with real zonal wavenumber, and signal in the meridional component. Given a

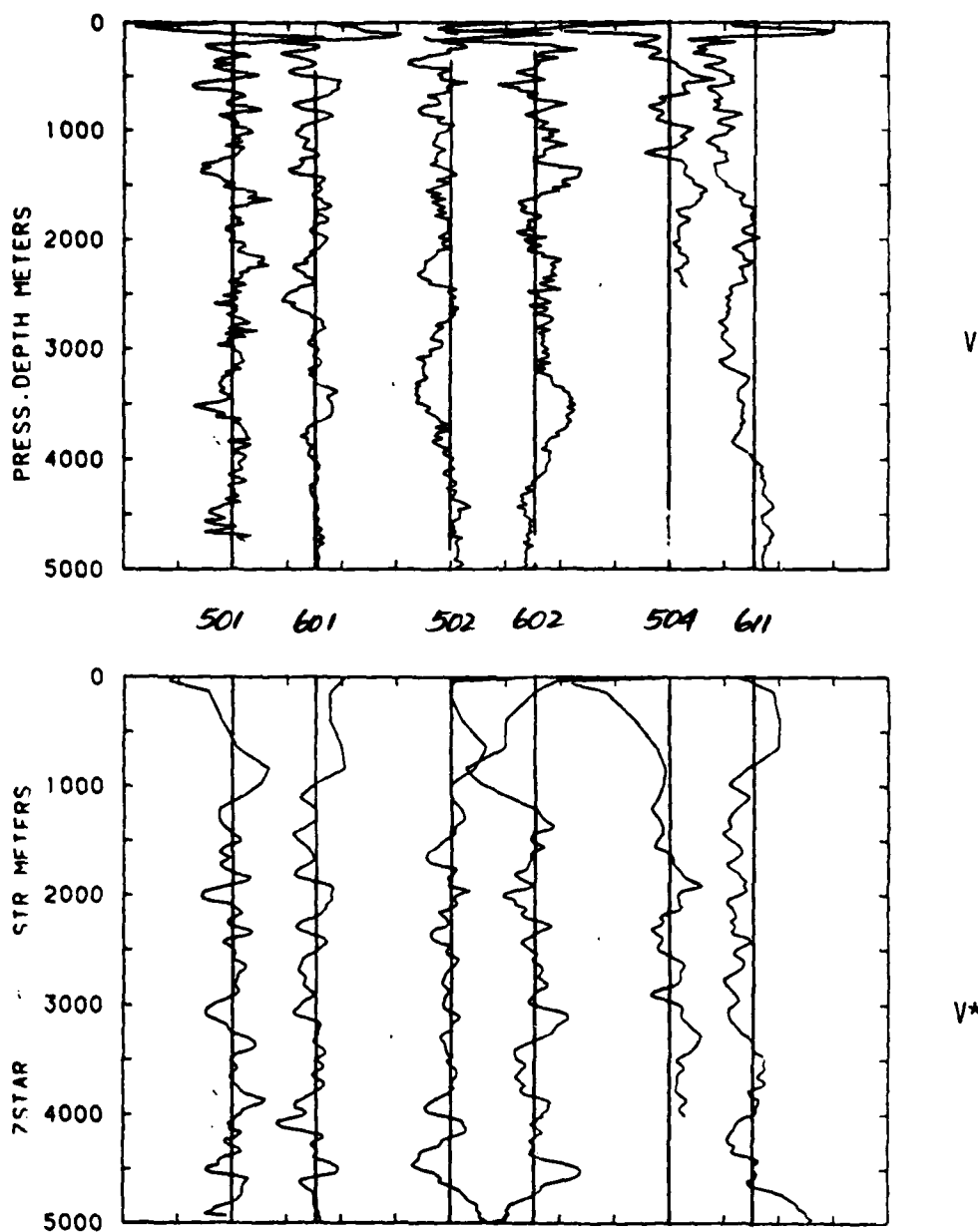


FIGURE IV-8

Comparison of pairs of profiles at the equator: 500 series are from  $50^{\circ}30'E$ ; 600 series are from  $53^{\circ}E$ . Each pair was separated by elapsed time of two weeks from the adjacent pair(s).

vertical wavelength of 450sm and vertical phase propagation upward, a mixed wave with 47-day period will have a zonal wavelength of almost 1000km and an eastward zonal group velocity of 5.9cm/sec or 5.11km/day. Thus almost four wave periods would be required to travel from the African coast to 53°E. At that longitude, it would have penetrated ~800sm deeper into the water column while traveling a thousand kilometers zonally.

If the longer period estimate, 72 days, is taken from the dropped lagged coherence results, the zonal wavelength is much shorter, ~410km, the group velocities are almost halved, and depth penetration at 53°E is about 535sm.

Choosing the intermediate period of 57 days from the linear fit yields a zonal wavelength of ~730km and zonal group velocity of 5cm/sec. A disturbance originating at the African coast with energy propagation downward, related to the Somali current, for example, and with an initial depth penetration of 400m, say, will have propagated approximately 1000km by the time it reaches 53°E. The depth interval from the surface to 400m is equivalent to the interval from the surface to 1700sm in the stretched coordinate, and in 1000km such a disturbance would have penetrated only 700sm deeper into the ocean. Since the portion of the stretched ocean that has been examined in the above spectral analysis is 1400-5000sm, a coastal disturbance generating a Kelvin or mixed wave at this period (57 days) will only have involved the upper 1000sm of the examined water column. For a longer period, the angle from the horizontal of the ray path along which energy

travels is even shallower. Reexamination of Figure IV-8, shown earlier in the discussion of the 1200sm wavelength band, demonstrates that the clearest antisymmetry is in the upper part of the water column and at a length scale shorter than 1200sm, so that the longitudinal reversal of phase may relate to this 450sm oscillation.

For the above periods, the relationship between zonal phase speed and rms zonal velocity is consistent with the linearization assumption: the rms zonal velocity estimated from the autospectra is  $\sim 3$ cm/sec at the equator and  $3/4^\circ\text{N}$ , at least one order of magnitude smaller than the phase velocities ( $\sim 7$ cm/sec for a period of 72 days,  $\sim 45$ cm/sec for a period of 47 days). The mean flow is also of much smaller magnitude than these phase speeds.

The energy e-folding distance  $[N_0/g \{m\}]^{1/2}$ , i.e., the equatorial Rossby radius of deformation, is 77 km, so it is not surprising to find that the period signal is in fact weaker at  $3/4^\circ\text{N}$ .

### Conclusion

There is strong evidence of vertical propagation from the dropped lagged cross-spectra of 1976 White Horse profiles of the meridional velocity component. The indicated propagation is at two different vertical wavelengths and is in opposite directions. The above interpretations showed that all of the information available from the data studied here are at least reasonably consistent with the presence of two separate mixed Rossby-gravity waves.

## Chapter V. Conclusion

The major results from this research are the evidence of equatorial trapping, which varies with vertical wavenumber, and evidence of vertical propagation, which in some cases is consistent with the presence of particular equatorially-trapped meridional wave modes.

The presence of deep energy, well below the thermocline, was revealed by the White Horse profiles in 1976. The velocity structure which became visible was not any simple current field but a complex multi-directional, rather than zonally-dominated field, albeit with multiple reversals. A unique forcing regime exists at the equator, such that waves can be forced at any frequency, so that coupling with atmospheric variability at all periods is possible. With respect to the Indian Ocean as a dumping ground for atmospheric energy, Luyten and Roemmich (1982) have estimated that the downward flux of energy through the thermocline at 180 days corresponds to an amount 15% of the annual mean energy put into the North Atlantic.

The questions of what happens to that energy put in at the surface, presumably by wind forcing, and of the setup problem of modes, particularly meridional modes in the equatorial waveguide, have not been addressed here. The setup of vertical modes versus vertical propagation has been examined in passing and remains to be comprehensively addressed. The problems involved here are clear:

only in special cases can energy in a particular meridional mode propagate even predominantly vertically, so that zonal diffusion of energy at a particular vertical wavelength and particular period is involved. The  $x,z$ -angle at which energy propagates requires multiple reflections from sidewalls (of non-longitudinal orientation in the western Indian Ocean) as well as from the bottom, before energy could return to the same  $x,z$ -location. Related issues are the mechanisms for vertical scale selection: the problems of energy propagation through the thermocline and through the zonal surface and near-surface currents have also not been addressed here.

What has been attempted is a definition of what was going on beneath the thermocline in the western Indian Ocean during May and June of 1976, with the presumption that that period was not atypical. Energy was clearly present: what was its form? Initially, an attempt to examine possible forcing mechanisms was planned. The equatorial concentration of energy seems to rule out off-equatorial sources, although the latitudinal coverage is limited to  $3/4^\circ$  south of the equator. Ray path tracing from sources such as the Somali Current is constrained by the direction of propagation (phase downward) for the strongest and most consistent signal of vertical propagation.

The clearest evidence for vertical propagation is from the meridional velocity component at vertical wavelengths of 1200sm and 450sm. In both cases, the indicated periods allow only mixed Rossby-gravity waves in a linear wave model. The autospectral peak at 1200sm for  $v$  is echoed by the peak in dropped lagged coherence at that

wavelength. The period indicated is 2-3 months, with a best fit of 72 days. Energy decreases away from the equator, at a slightly lower rate than the theoretical Gaussian with latitude. The zonal wavelength of 300-400km obtained via the dispersion relation is reinforced by a comparison of profiles separated by  $2.5^\circ$  of longitude at the equator. Phase propagation is downward, implying upward energy propagation.

The major inconsistency in the 1200sm interpretation, high coherence between  $u$  and  $v$  at the equator with a phase estimate of approximately  $180^\circ$ , can be explained by the simultaneous presence of a Kelvin or Rossby wave of at least twice the period of the mixed wave, with approximately the same vertical scale. This explanation is consistent with analysis of a slightly reduced portion of the water column, which resolves different vertical wavenumber bands, and indicates that the zonal energy is concentrated closer to a vertical wavelength of 1600sm than 1200sm and is consequently not well-resolved by the discretization from spectral analysis of the entire sub-thermocline water column.

The second strongest evidence of vertical propagation is for a vertical wavelength centered at 450sm, and the indicated direction of propagation is upward in this case, implying a surface energy source. The energy e-folding distance is consistent with the theoretical structure of a mixed Rossby-gravity wave and the period estimate from the dropped lagged coherence results is 1 1/2-2 1/2 months, with a best fit of 57 days. The corresponding zonal wavelengths calculated using the linear dispersion relation are 410-2000km, with 57 days yielding a



zonal wavelength of ~730km.

Dropped lagged coherence analysis of the zonal velocity component suggests processes of longer period than can be resolved with this set of observations. The phase reversal across 2°N suggests the presence of a first meridional mode Rossby wave. However, the energy observed at 3°N relative to the equator is higher than explainable by the presence of a first mode Rossby wave.

Examination of spectral energy density variation with latitude showed equatorial intensification at all vertical wavenumbers for both velocity components. The meridional velocity component settles to an apparent background level at 1.5°N, and a Gaussian decrease in energy away from the equator can be extracted for the wavenumber bands encompassing 287sm through 1440sm. That decrease is consistent with the dominance of the meridional velocity field by mixed Rossby-gravity waves. Note that the slant of the east African coast near the equator, approximately 45° to the meridian, theoretically favors the selection of mixed Rossby-gravity waves when incoming energy is reflected (Moore, personal communication).

Zonal kinetic energy is less tightly trapped to the equator than meridional, and appears to decrease more gradually to 5°N, the furthest data station. For all four of the averaged wavenumber bands studied here, however, the estimate at 1.5°N is significantly lower than that at the equator, at the 95% confidence level. There is relatively more energy in the zonal component at longer wavelengths, relatively more in the meridional component at shorter wavelengths.

The equatorial intensification is stronger at shorter wavelengths for both components, consistent with linear theory. A general conclusion from the analysis of equatorial trapping is that more than just mixed Rossby-gravity and Kelvin waves are present. The distribution of energy implies the presence of Rossby waves as well.

A comparable series of profiles, also using the White Horse, was collected in the western equatorial Pacific Ocean in 1978 by Charles Eriksen (1981). That series has greater longitudinal coverage, so that individual stations were not repeated as often as in the Indian Ocean. Consequently, those profiles cannot be examined as a time series. The Pacific profiles cover approximately the same latitudinal range about the equator, so that comparisons can be made on that basis.

Equatorial intensification was observed in the Pacific data for all three variables, both of the horizontal velocity components and vertical displacement. The relative intensity of trapping was the reverse of that observed in the Indian Ocean, i.e., stronger for the zonal velocity component than for the meridional. The displacement spectra in the Indian Ocean do not exhibit equatorial intensification. The averaged autospectra of zonal kinetic energy from the Pacific and the Indian Oceans are not distinguishable either in energy level or in latitudinal distribution, within the 95% confidence level error bars (cf. Eriksen, 1981, figure 7, and Figure III-1). The Indian Ocean autospectral estimates for meridional kinetic energy, however, are significantly higher at the equator for the 720, 360, and 240sm wavelength bands, although indistinguishable from the Pacific

observations  $1.5^\circ$  away from the equator.

A major result of Eriksen's analysis (1981, 1982) was the conclusion from the phase relation between zonal velocity and vertical displacement at the equator (where  $\xi$  led  $u$  by  $90^\circ$  with depth for vertical wavelengths longer than 100sdb) and from the equatorial trapping of those two variables that Kelvin waves dominated near the equator. No such conclusion can be drawn for the Indian Ocean from this data.

Heavy averaging over vertical wavenumbers was required for the Pacific data in order to obtain statistically significant results, since there were fewer profiles at a particular station. The resultant spectra are smooth and significant coherence estimates are rare. The discrete vertical structures revealed in the Indian Ocean spectra disappear with wavenumber averaging, as does the significance of the coherence pairs, so that it is clear that the dominant vertical processes in the Indian Ocean are narrow band in vertical wavenumber.

Our observational capacity in the ocean is limited. Current meters can be deployed for long time spans and provide excellent sources for monitoring periodic oscillations at specific depths, but resources limit those specific depths. Vertical profilers offer snapshots of the water column, but using them to determine periodicity or to examine the longest vertical scales, corresponding for example to the lowest vertical modes, is extremely difficult. Dropped lagged coherence, used here, seems the only option for the former and the latter is

complicated by the inapplicability or gradual breakdown of the WKB approximation as the scales approach those of the vertical variability of the buoyancy frequency.

In any case, profilers are limited by the number of realizations possible between the surface and the bottom of the ocean. Current meters merely need to be deployed some multiple of the period of interest in order to obtain multiple realizations in time. On the other hand, one of the problems revealed by these particular profiles is that motion at depth appears highly organized, whereas linear theory indicates that energy propagation occurs at shallow angles to the horizontal for low meridional modes. Intuitively, it is easier to envision the setup of the lower modes.

Additional observations exist now of the complex vertical structure in the equatorial oceans. The particular instrument used here has also been used in the equatorial Pacific Ocean (Eriksen, 1981), and other profilers have been used in both the Pacific and the Indian Oceans (Hayes, 1981; Leetmaa and Spain, 1981). Other investigations have discovered the dichotomy in frequency dominance of the velocity components. Weisburg and Horigan (1981) discuss evidence in the eastern equatorial Atlantic for a vertically-propagating mixed Rossby-gravity wave of 30-day period dominating the meridional velocity component, while the zonal component indicates a periodicity on the order of four to eight months. With other types of instruments, oscillations with periodicities longer than several weeks have been discovered in the Indian Ocean: a 30-60 day period oscillation, perhaps

identifiable as a Kelvin wave, and a periodicity of 180 days (McPhaden, 1982), the last of which agrees well with the intense zonal signal analyzed as a combination of Kelvin and first mode Rossby wave by Luyten and Roemmich (1982). The latter also see a strong signal in the meridional velocity component, identified as a mixed Rossby-gravity wave of 26-day period (Roemmich and Luyten, personal communication).

Evidence of vertical wave propagation in the deep equatorial oceans leads to questions that go beyond linear equatorial wave theory. The basic state of the equatorial oceans is not quiescent, but includes both vertical and meridional shear flows. Their consequences have been well studied in the atmosphere, but the oceanic case has received much less attention. Since the equations of motion are not separable for the case of mean vertical shear, a numerical model is required.

The analyses of wave propagation in a mean flow field that have been done to date for the equatorial oceans have been primarily concerned with latitudinal variations of the mean flow in a two-layer ocean (McPhaden and Knox, 1979; Philander, 1979). Some qualitative analysis has been done by Philander (1979) of the effects of vertical shear across an interface, but specific examples need to be analyzed. Philander (1978) has also examined the transmission of equatorial waves through a typical tropical density profile, and concludes that only particular wavelengths can penetrate to great depths. Spectral analysis indicates certain preferred scales in the western Indian Ocean, so that the selection process becomes a first-order question.

## APPENDICES

Appendix A: Eight longitudinal transects showing zonal and meridional velocity profiles, vertical displacement profiles in original form and after WKB stretching and normalizing.

1.  $u, v, \zeta$  from  $5^{\circ}\text{N}$  to  $3/4^{\circ}\text{S}$
2.  $u^*, v^*, \zeta^*$  from  $5^{\circ}\text{N}$  to  $3/4^{\circ}\text{S}$

Appendix B: All profiles at each profiling site (i.e, temporal transects for each latitude):

1.  $u, v, \zeta$  for each net
2.  $u^*, v^*, \zeta^*$  for each net

Appendix C: Tables of coherence and phase

Table 1. (no wavenumber averaging)

- a.  $u^* * v^*$  [all profiles]
- b.  $\zeta^* * u^*$  [subset for which
- c.  $\zeta^* * v^*$  displacement is available]

Table 2. (averaged over 2 adjacent wavenumber bands)

$u^* * v^*, \zeta^* * u^*, \zeta^* * v^*$  [subset]

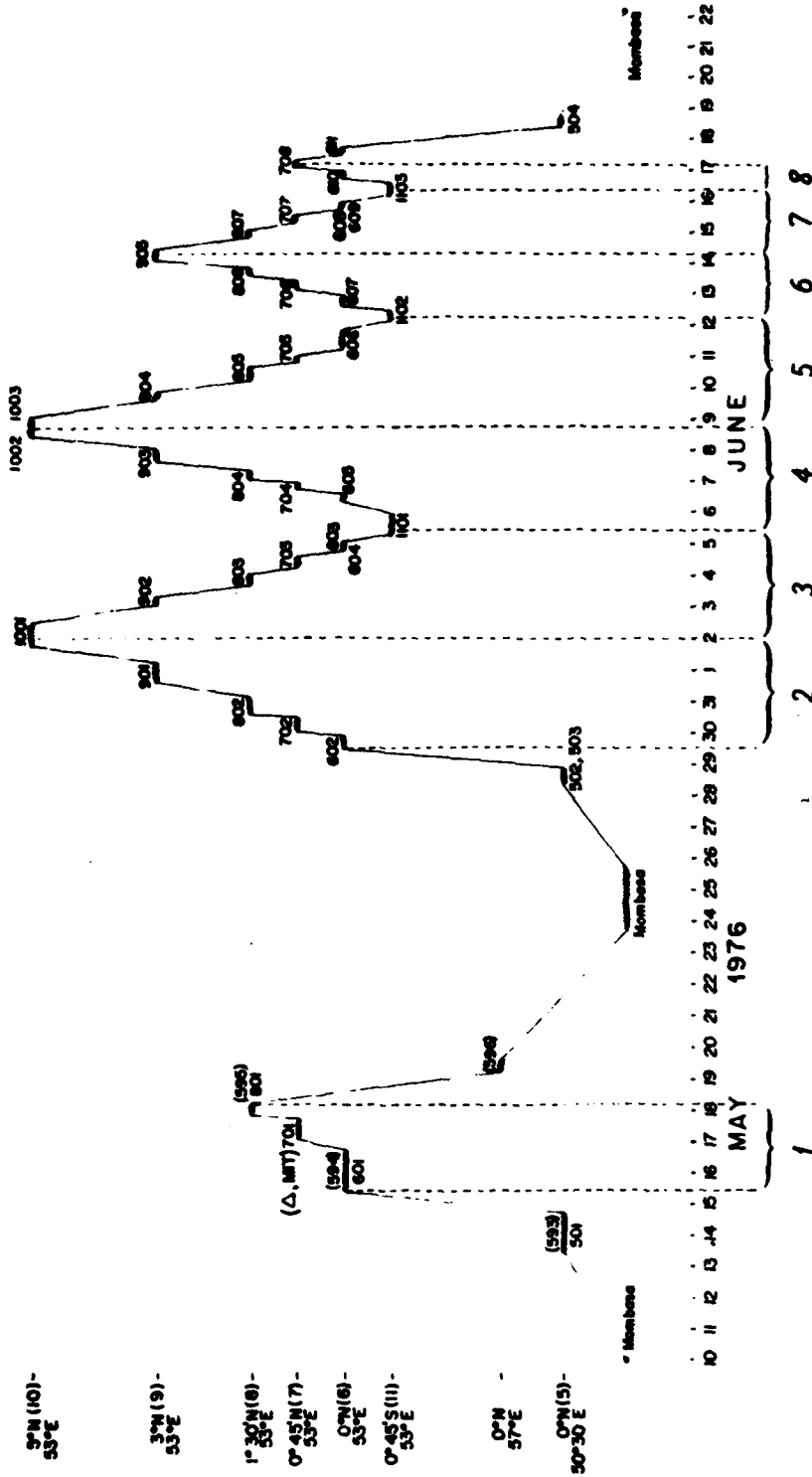
## APPENDIX A

Eight latitudinal transects showing zonal and meridional velocity and vertical displacement profiles in both original form and after WKB stretching and normalizing.

For each section,

- a)  $u, v, \zeta$  from  $5^{\circ}\text{N}$  to  $3/4^{\circ}\text{S}$ .
- b)  $u^*, v^*, \zeta^*$  from  $5^{\circ}\text{N}$  to  $3/4^{\circ}\text{S}$ .

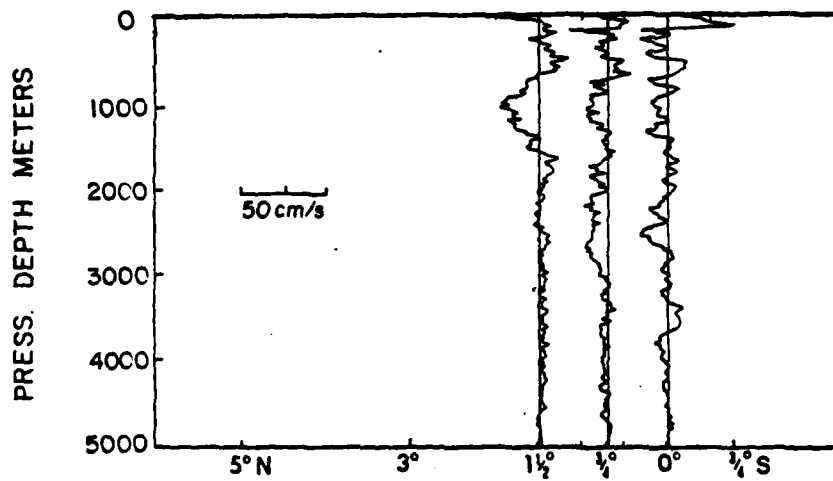
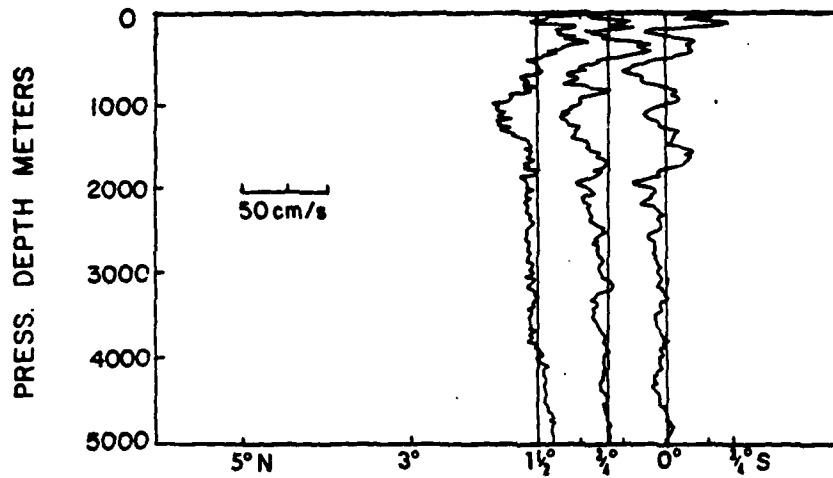
The profiles at the end points are common to sequential sections. The distribution of the sections in time is shown in the first figure (cruise track). Maximum elapsed time between profiles presented in the same section was 3.6 days ( $3/4^{\circ}\text{S}$  to  $5^{\circ}\text{N}$ ), and average elapsed time between the most closely spaced profiles ( $3/4^{\circ}\text{S}$  to  $1.5^{\circ}\text{N}$ , latitudinal spacing  $3/4^{\circ}$ ) was 12 hours.

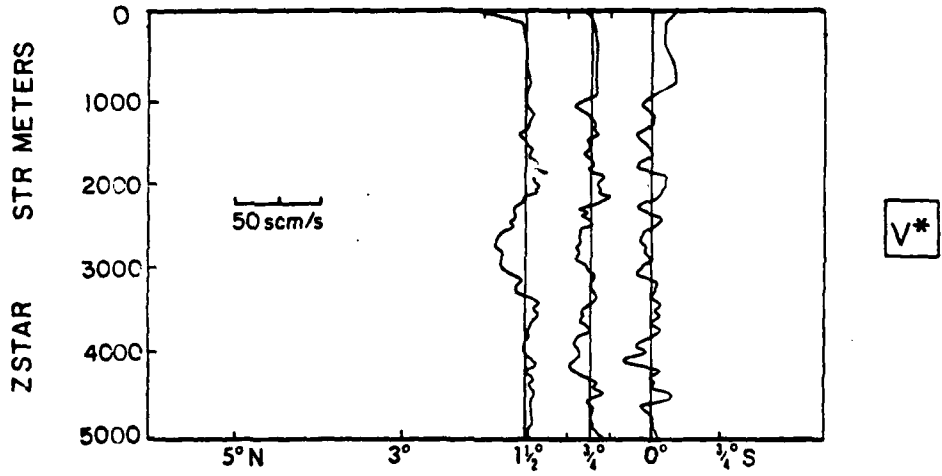
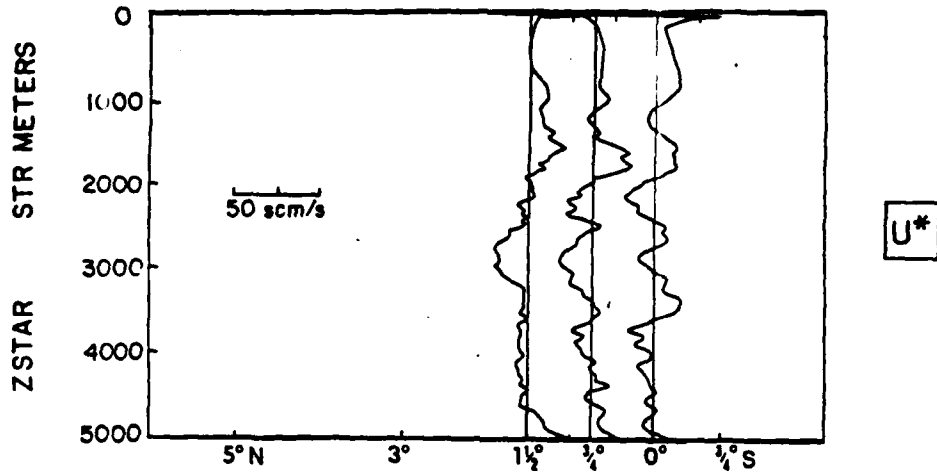


MERIDIONAL TRANSECTS ALONG 53°E

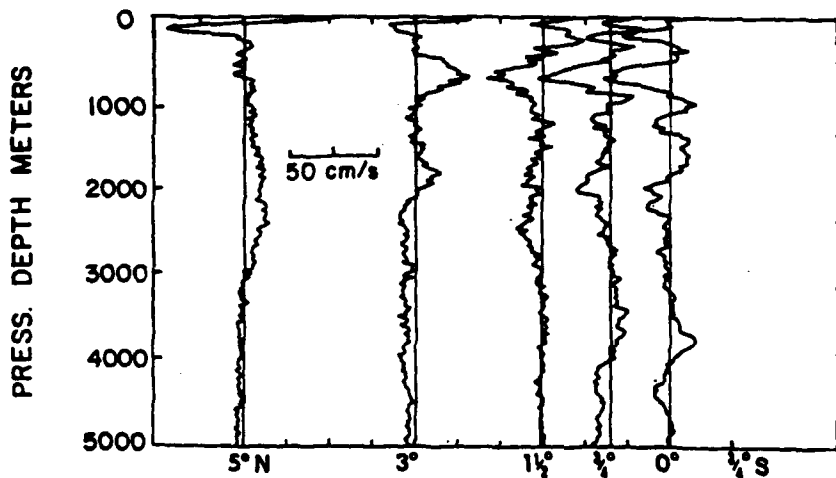


## SECTION I

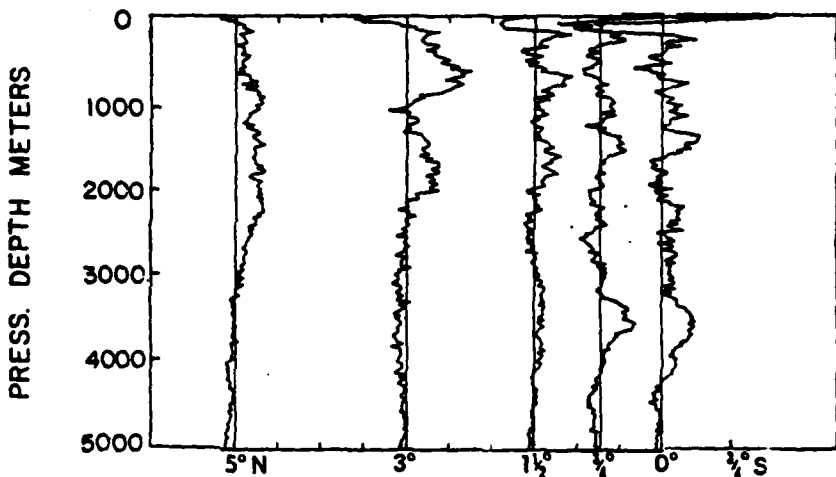




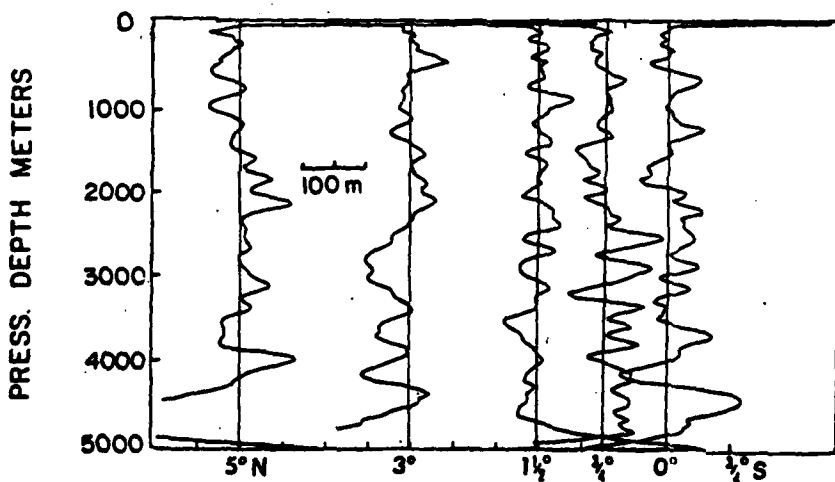
SECTION 2



U

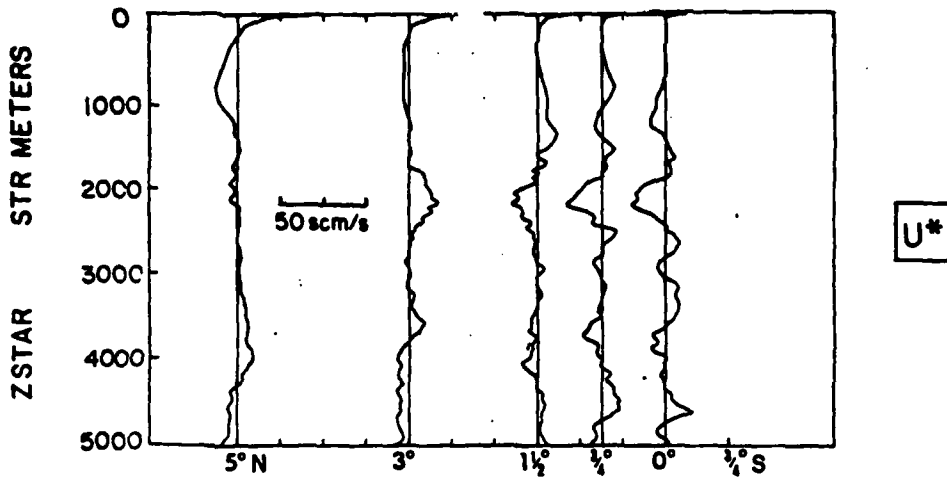


V

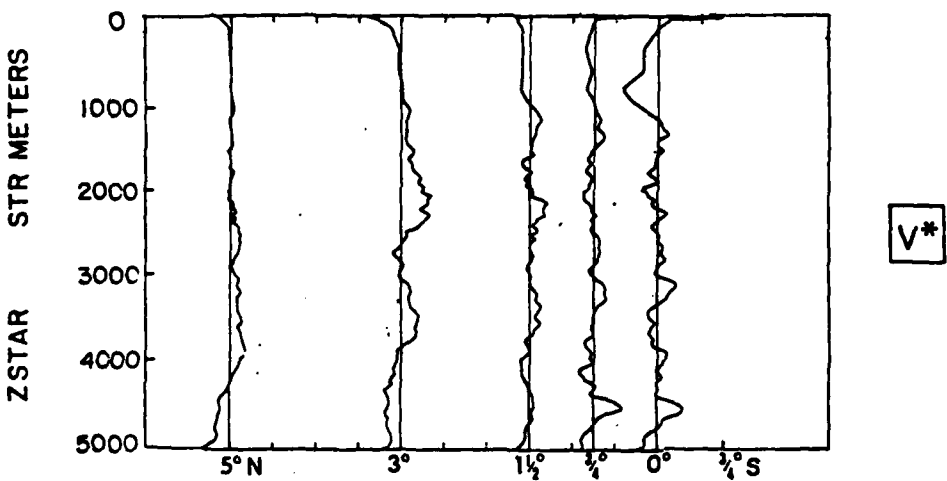


S

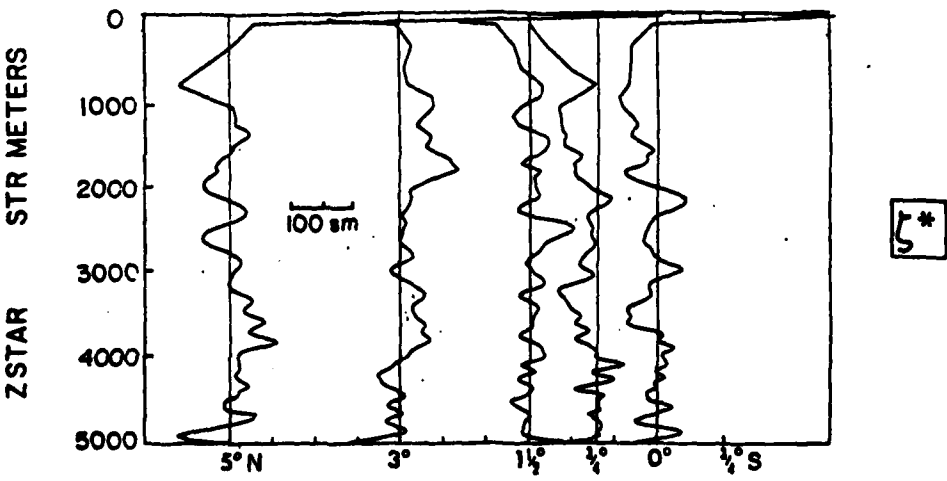
SECTION 2



$U^*$

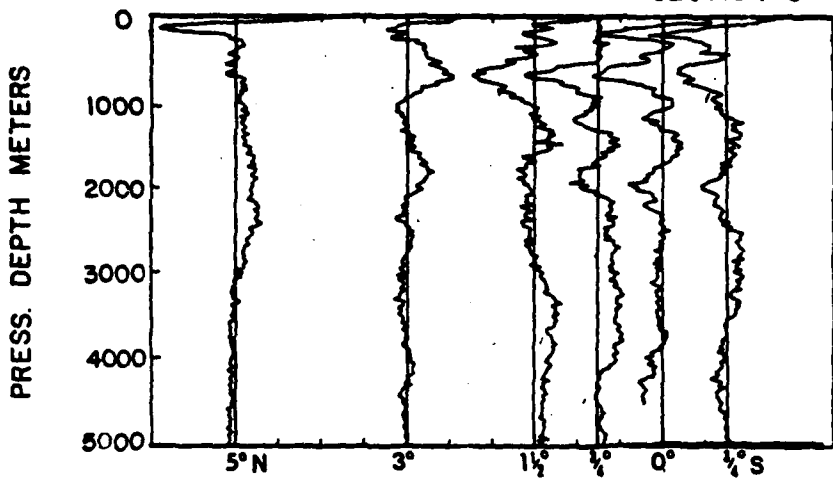


$V^*$

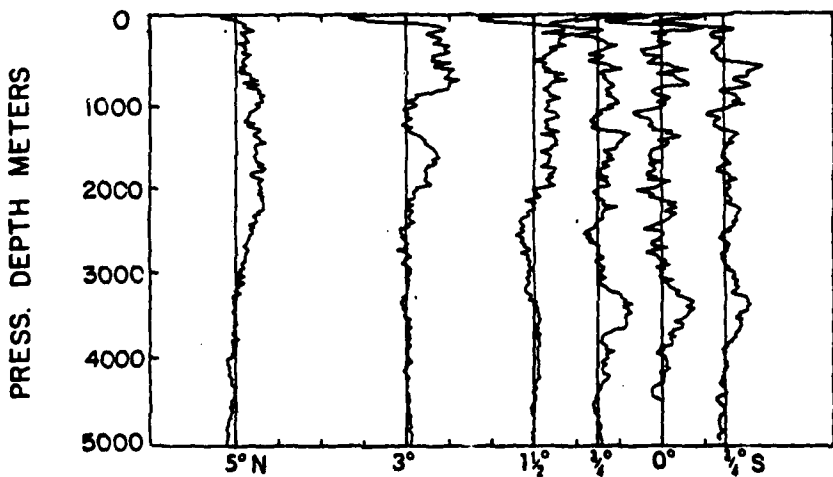


$\sigma^*$

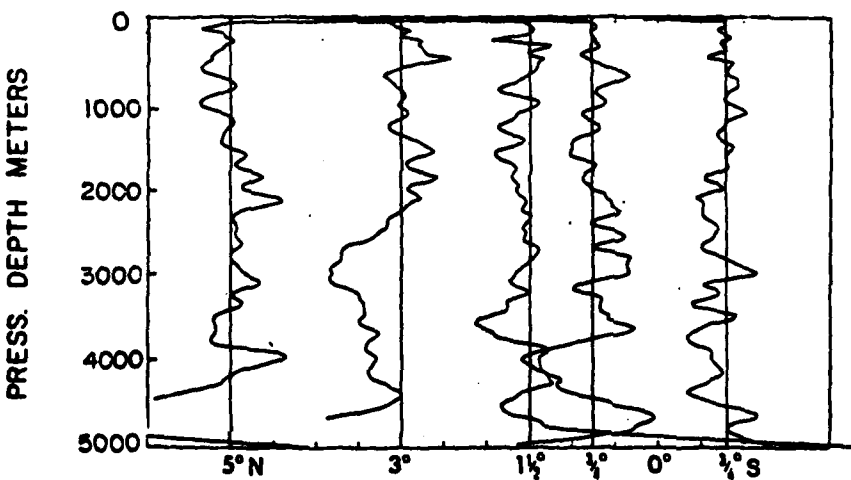
SECTION 3



U

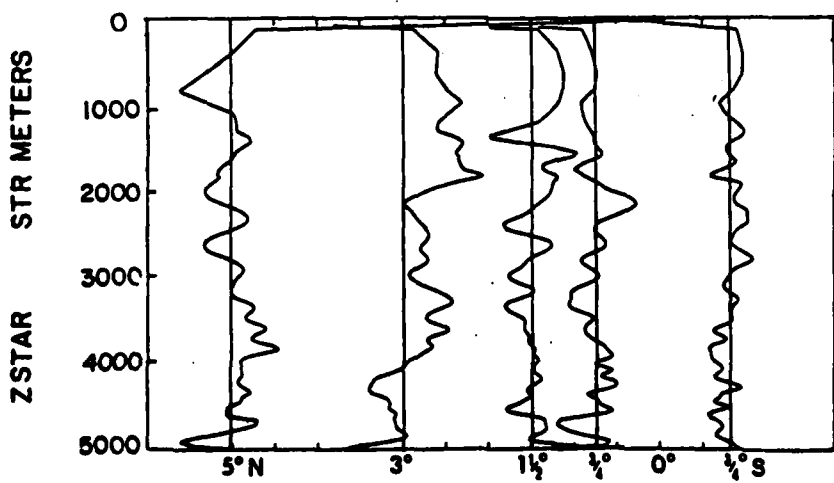
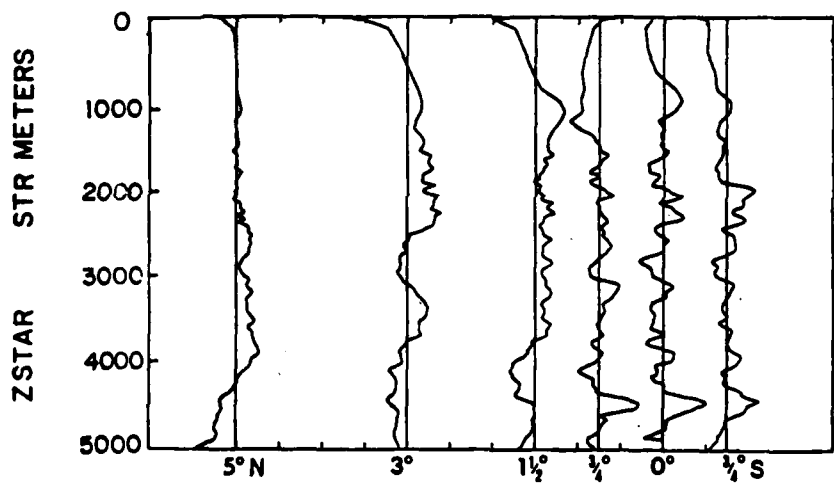
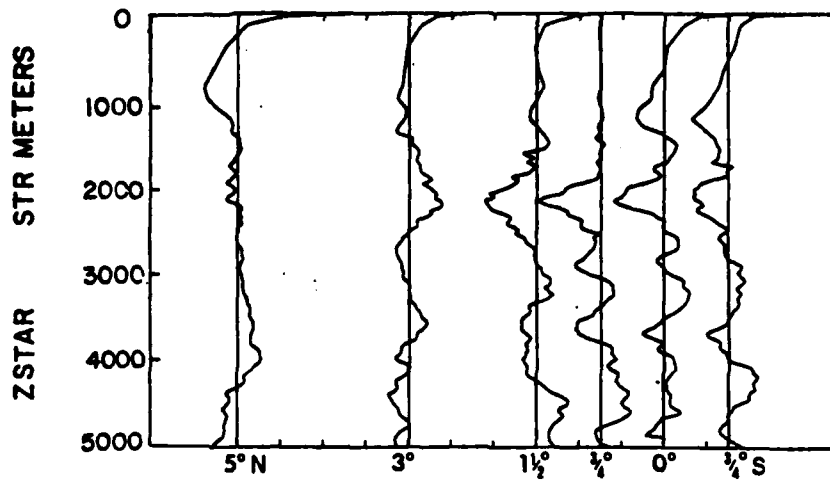


V

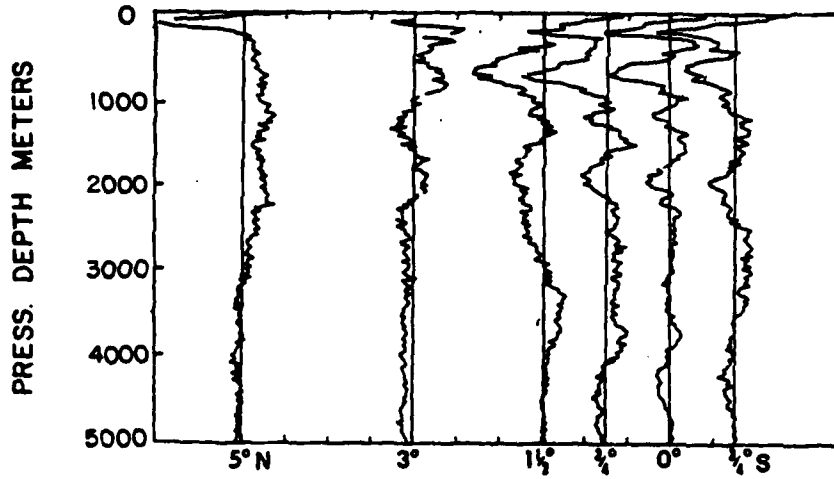


S

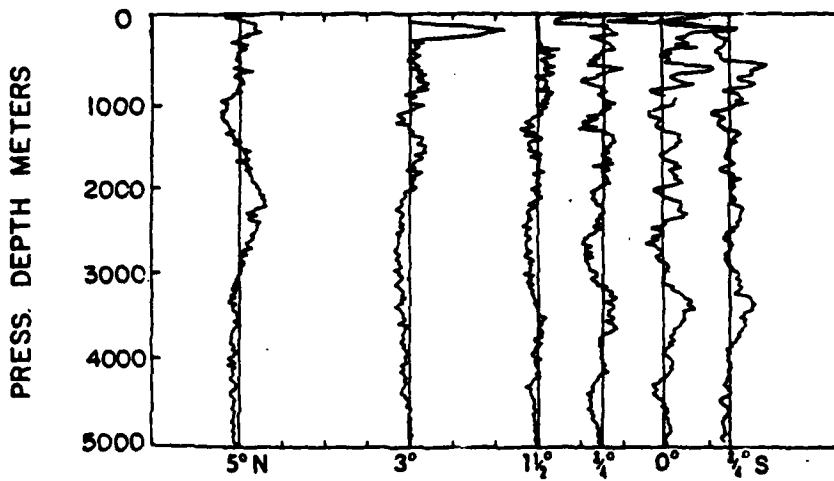
## SECTION 3



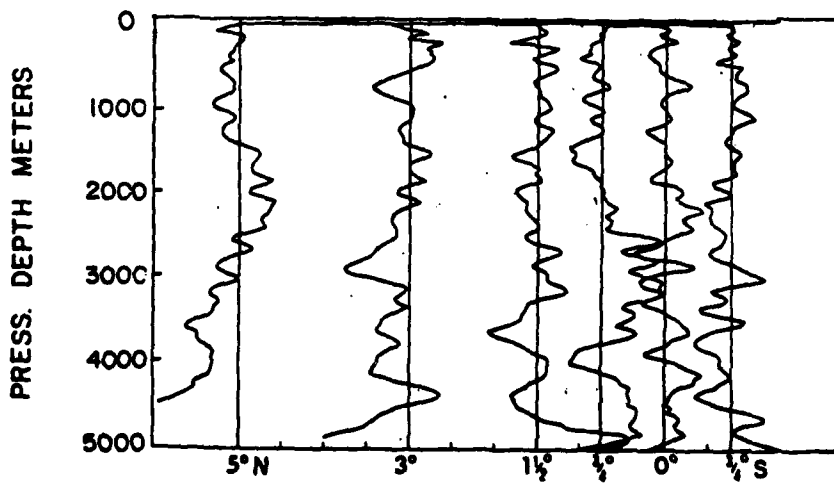
SECTION 4



U

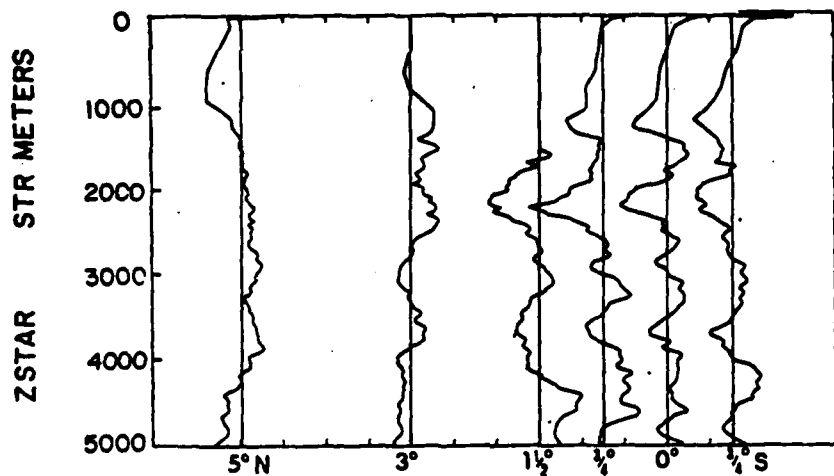


V

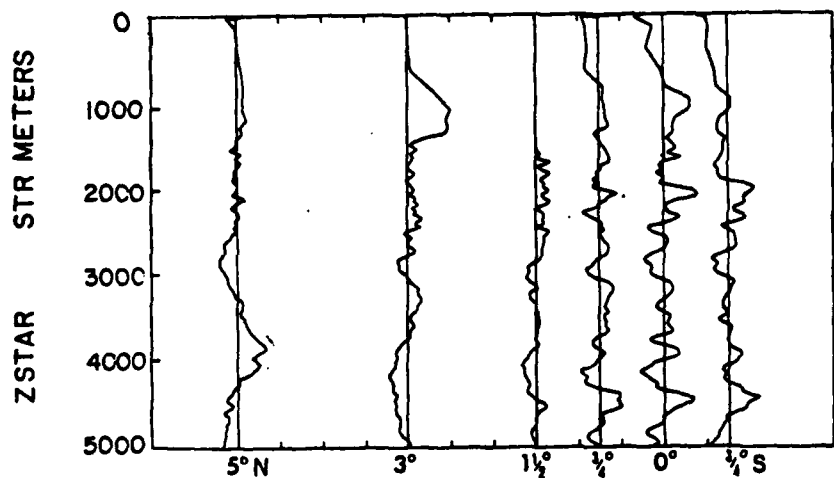


S

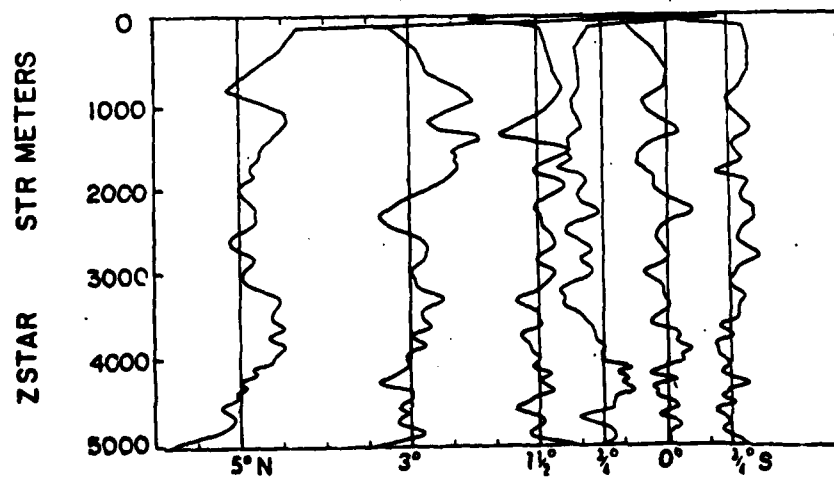
SECTION 4



$U^*$



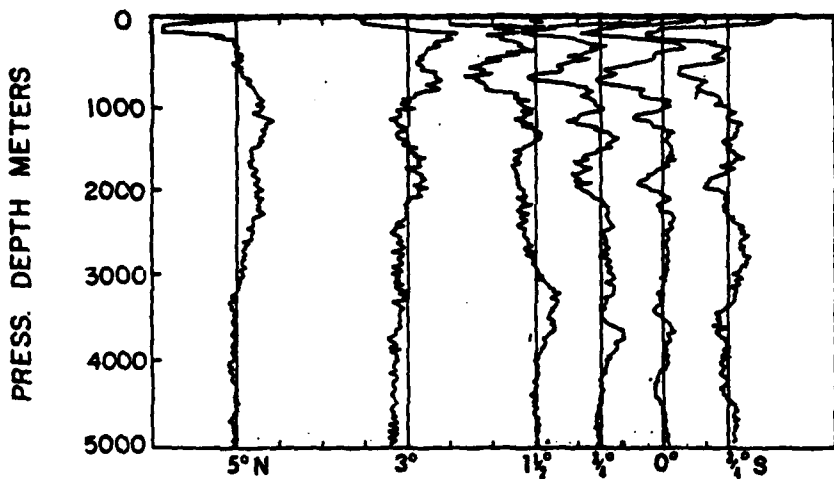
$V^*$



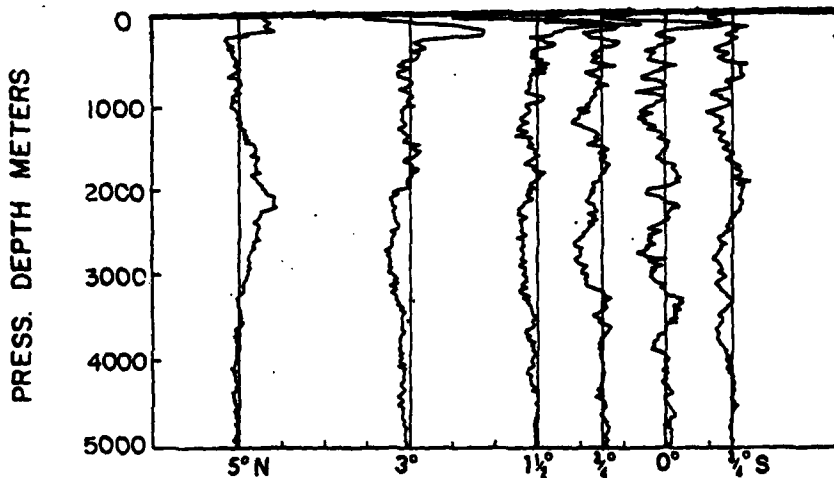
$W^*$



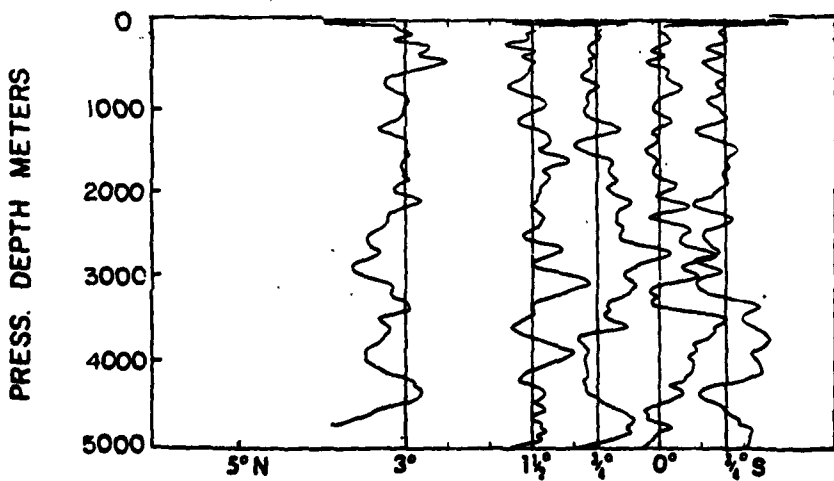
SECTION 5



U

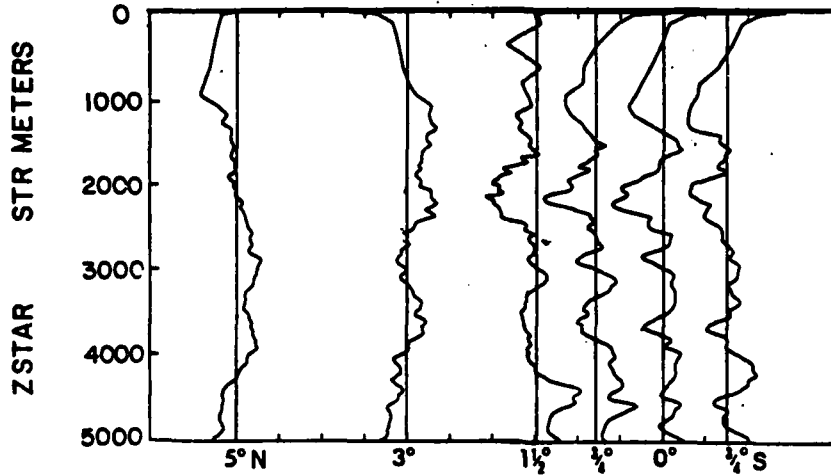


V

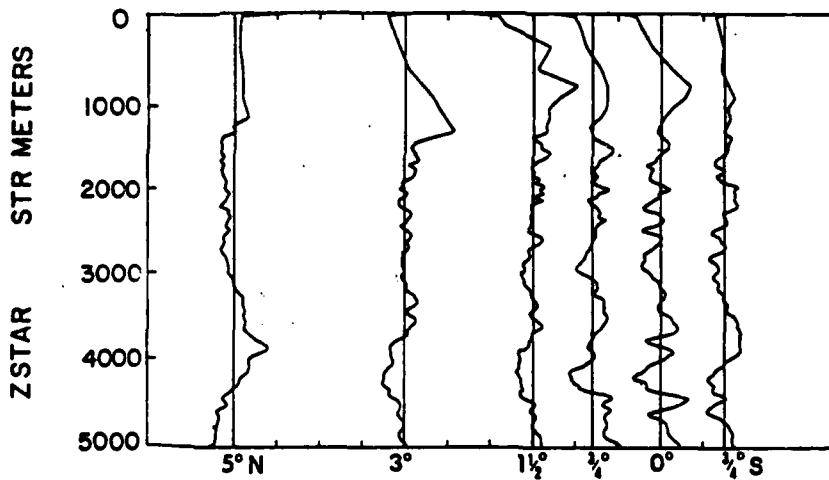


S

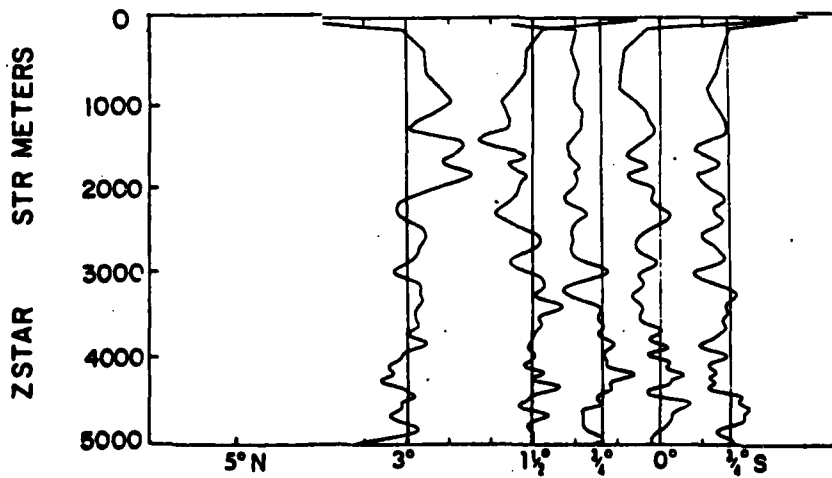
SECTION 5



$U^*$

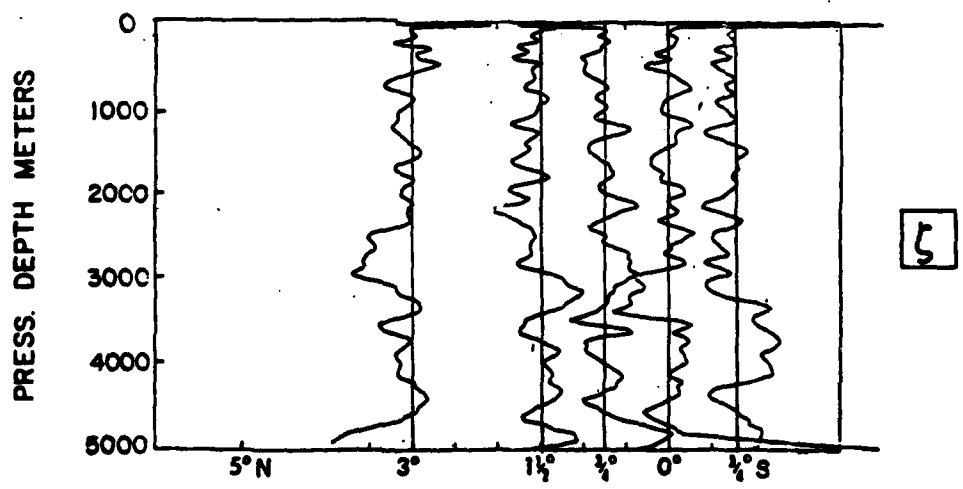
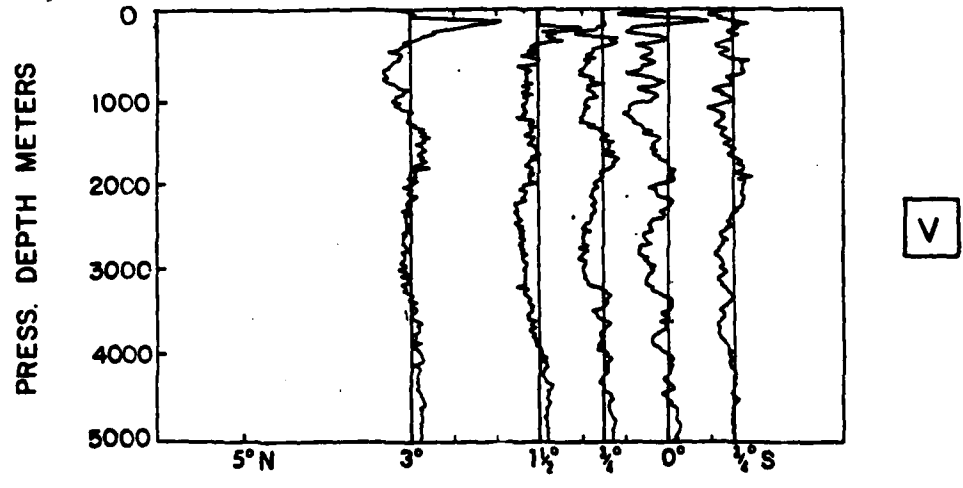
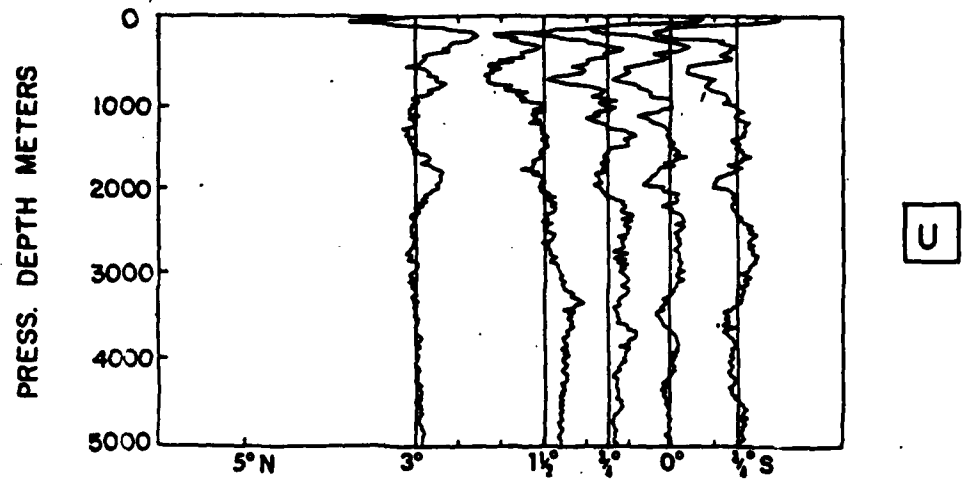


$V^*$

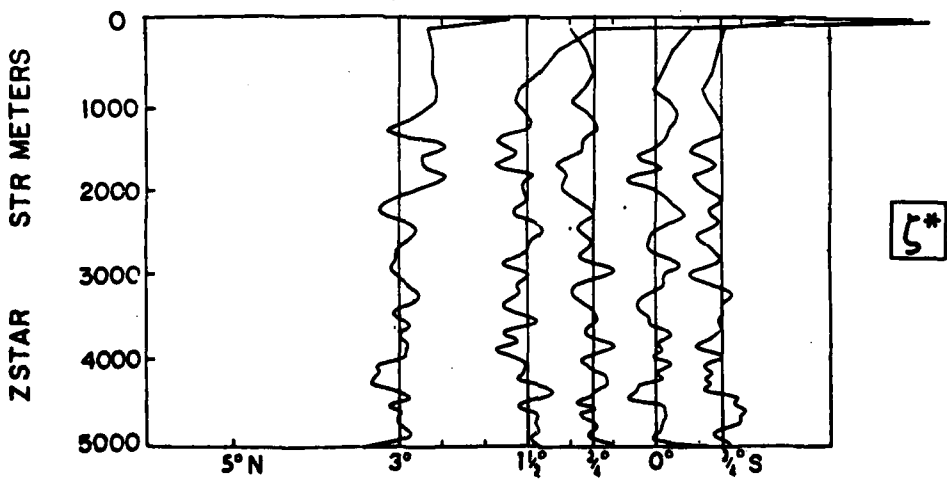
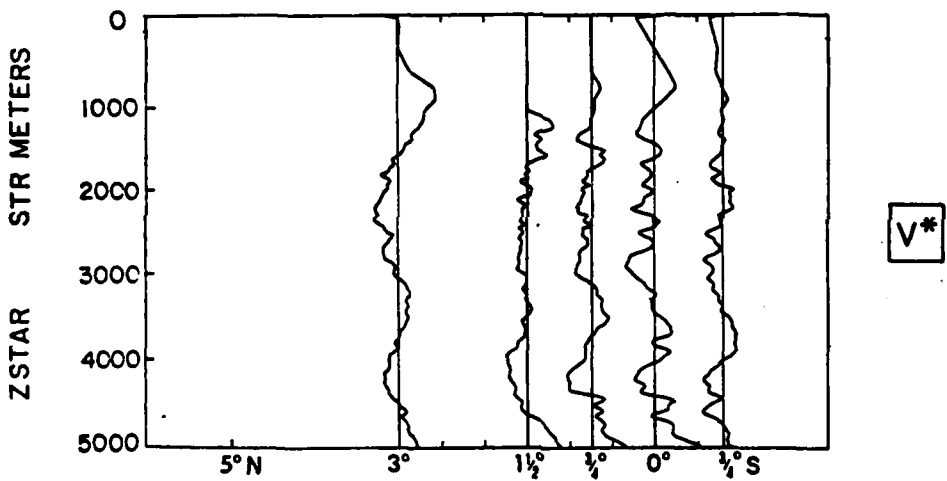
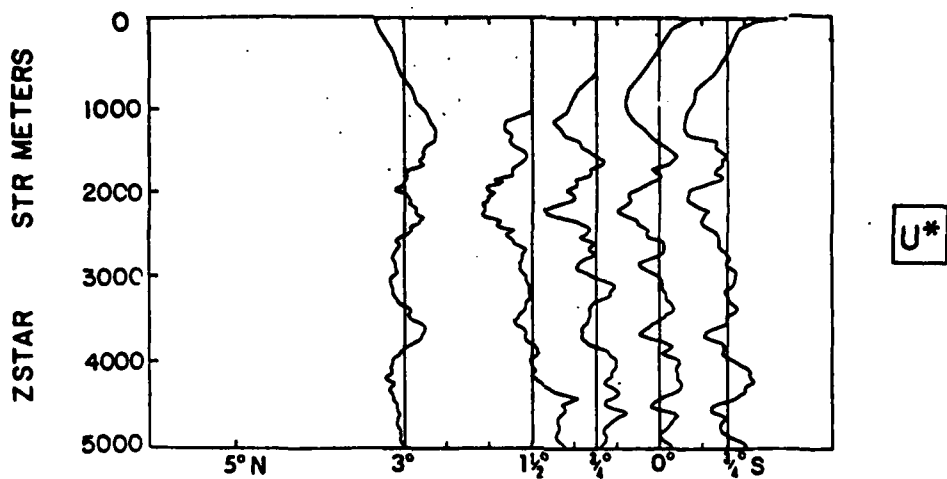


$\xi^*$

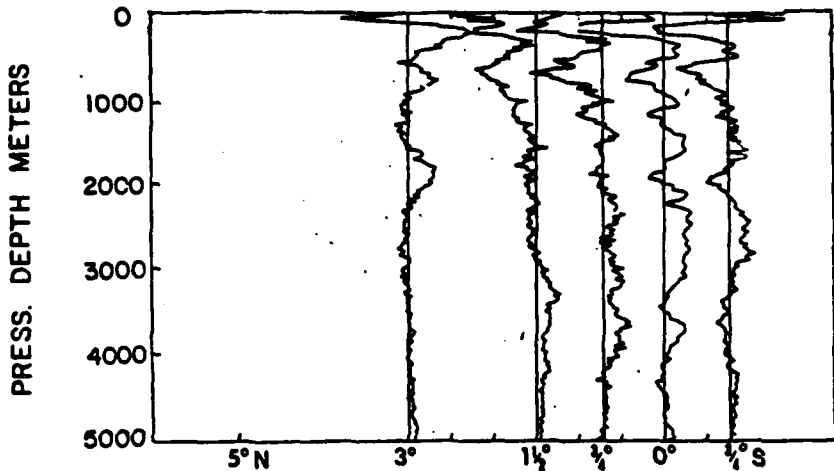
SECTION 6



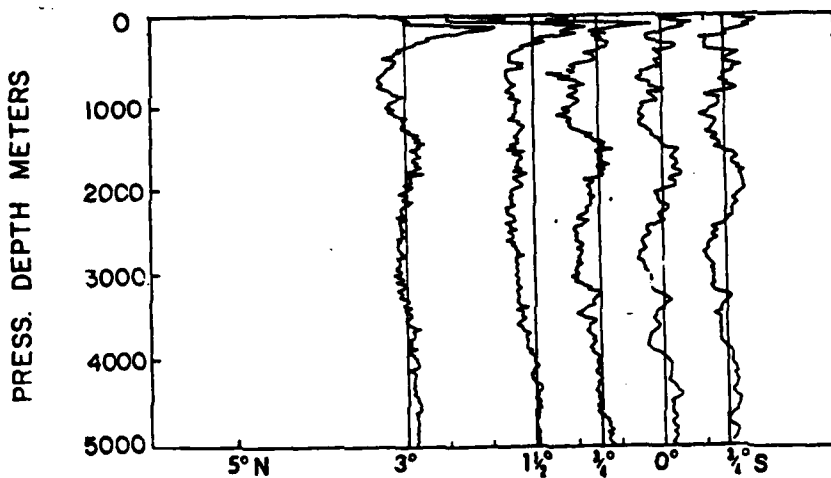
SECTION 6



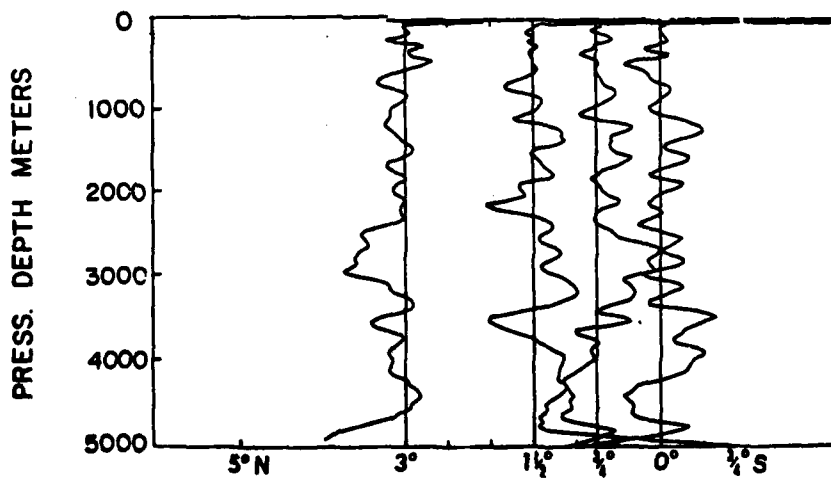
SECTION 7



U

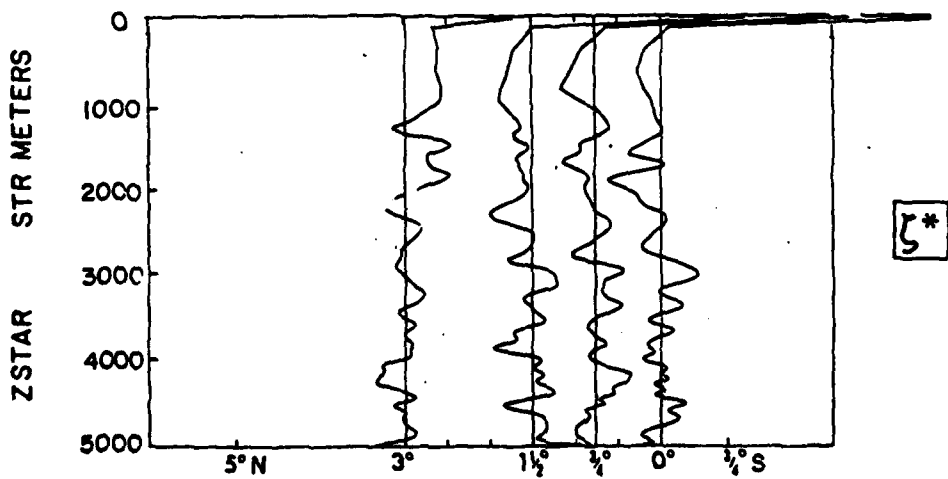
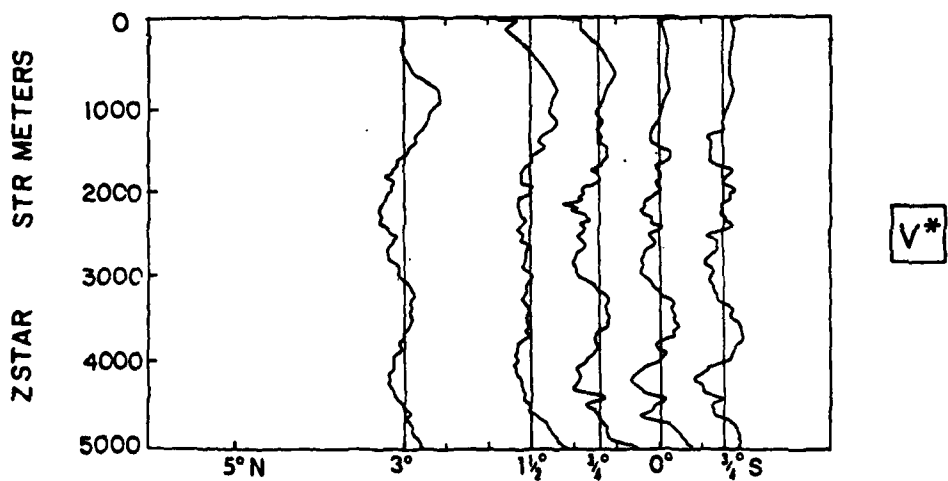
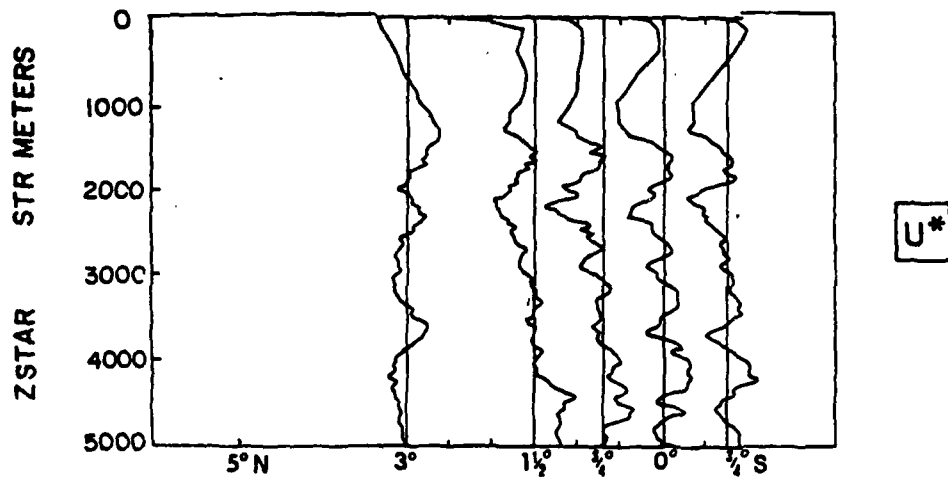


V

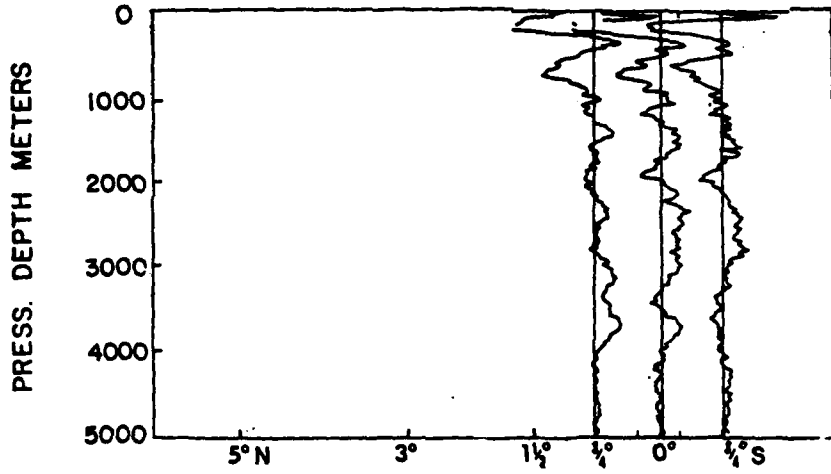


J

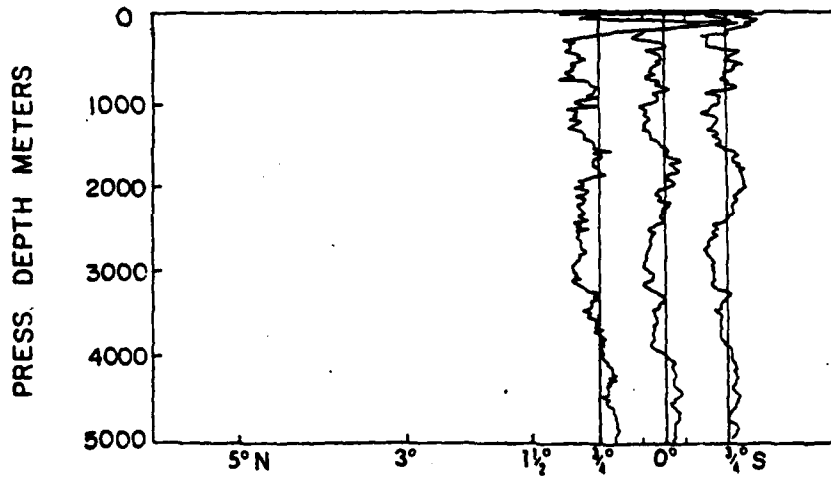
## SECTION 7



SECTION 8

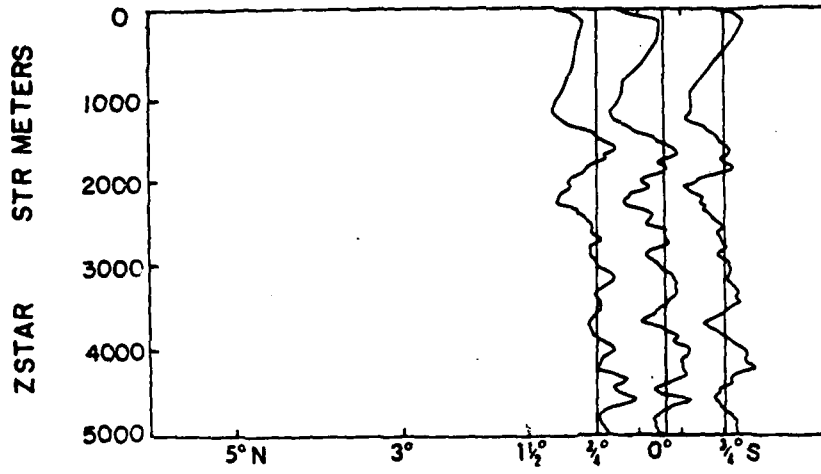


U

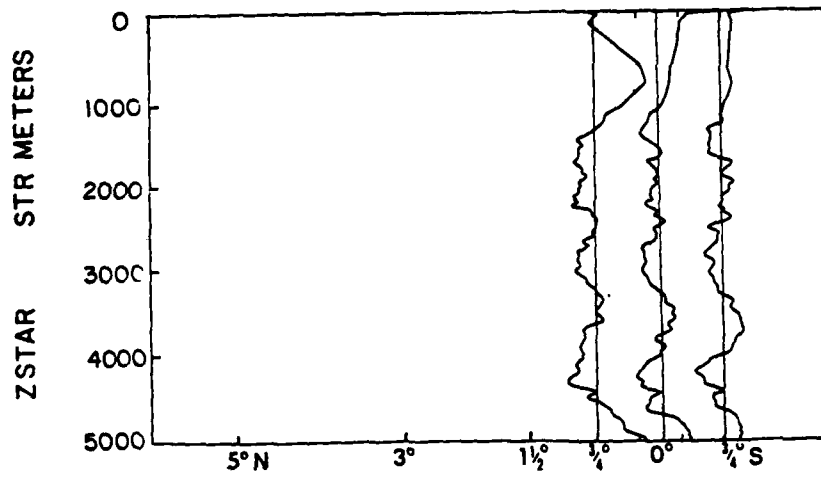


V

SECTION 8



$U^*$



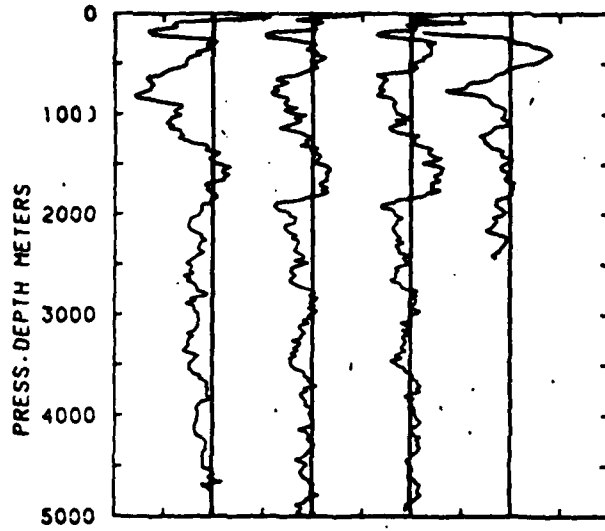
$V^*$



## APPENDIX B

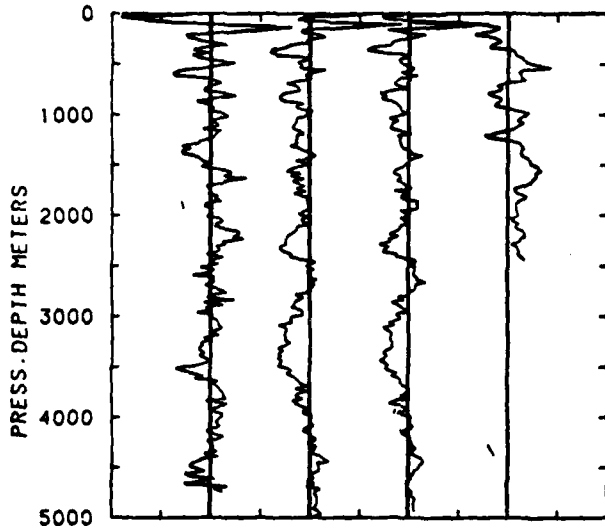
All profiles at each profiling site (i.e., temporal transects for each latitude):

- a)  $u, v, \int$  for each net
- b)  $u^*, v^*, \int^*$  for each net



501 502 503 504

U



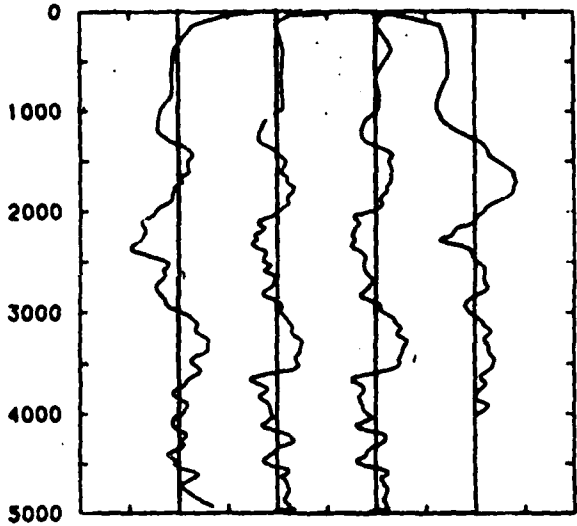
V

NET 5

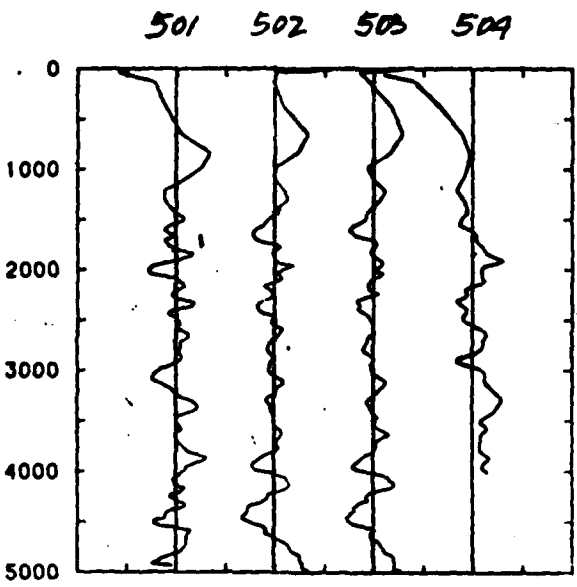
0° 50' 30" E

140

ZSTAR STR METERS



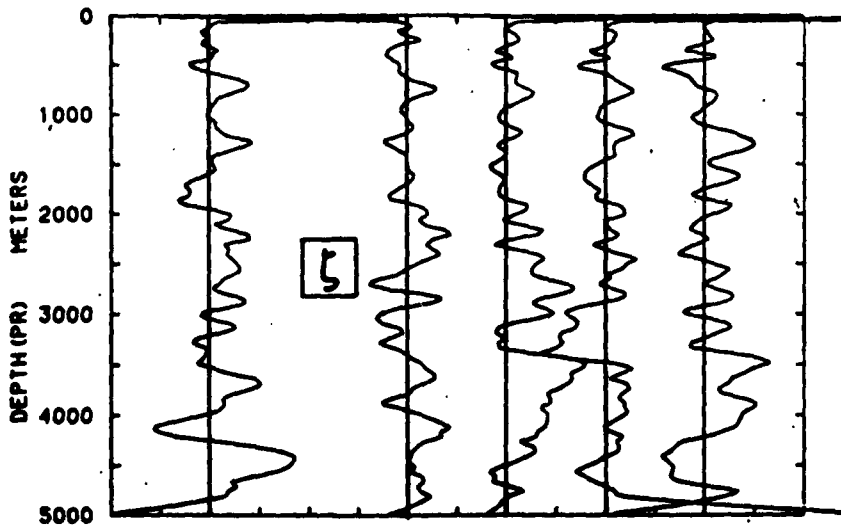
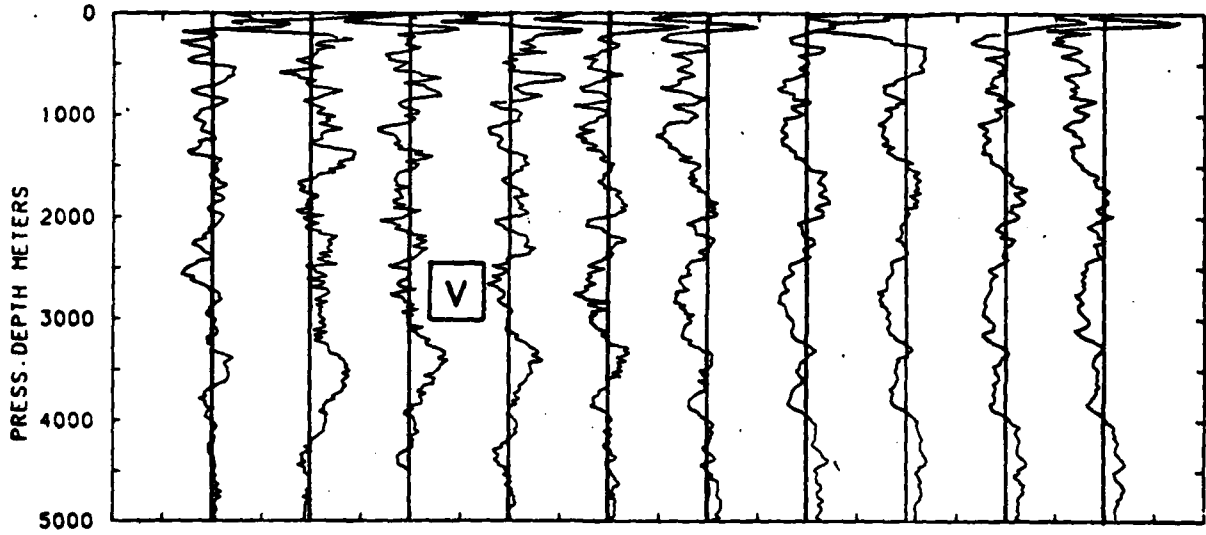
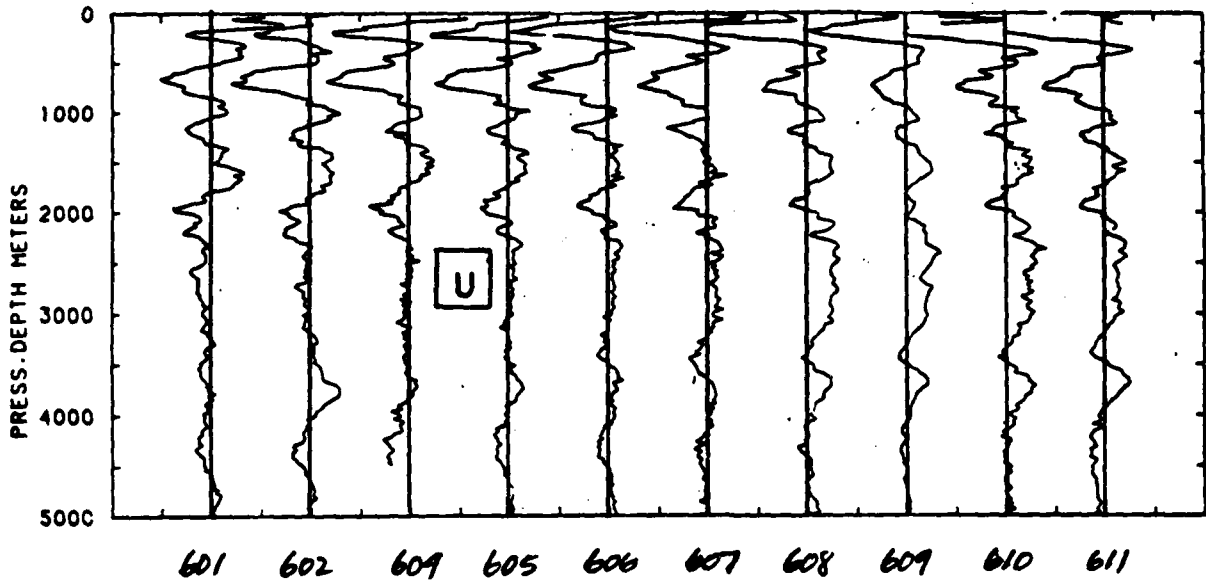
U\*



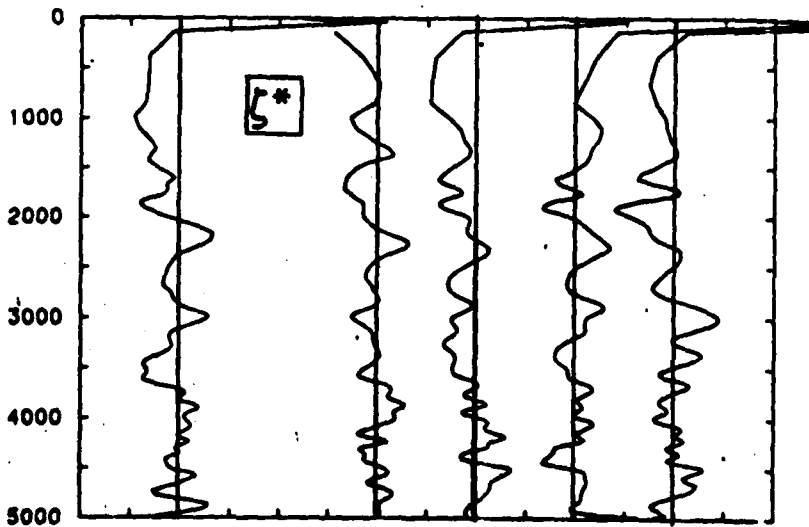
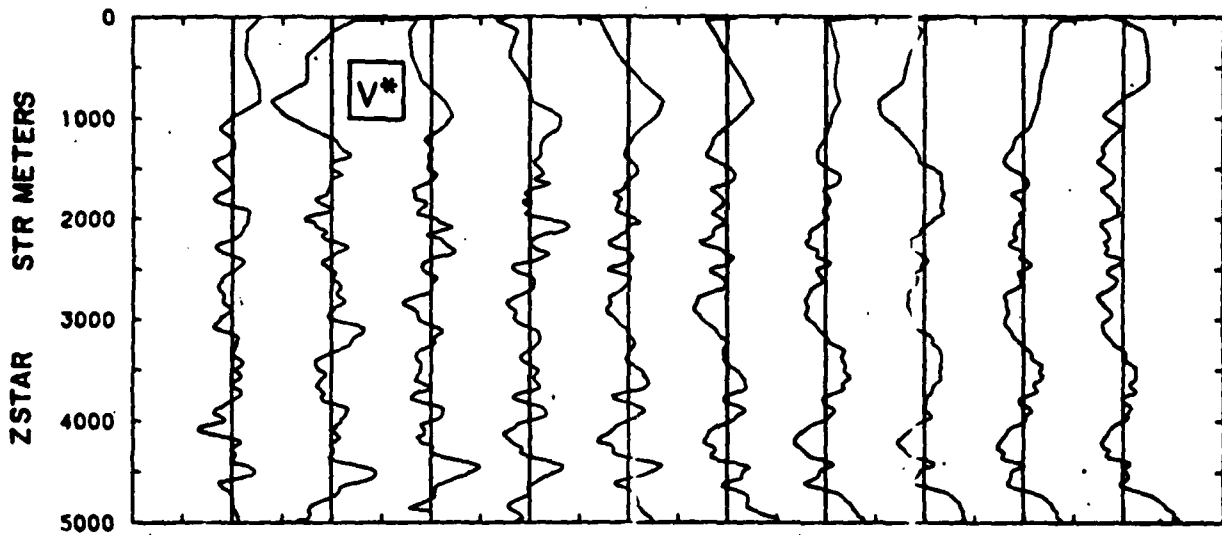
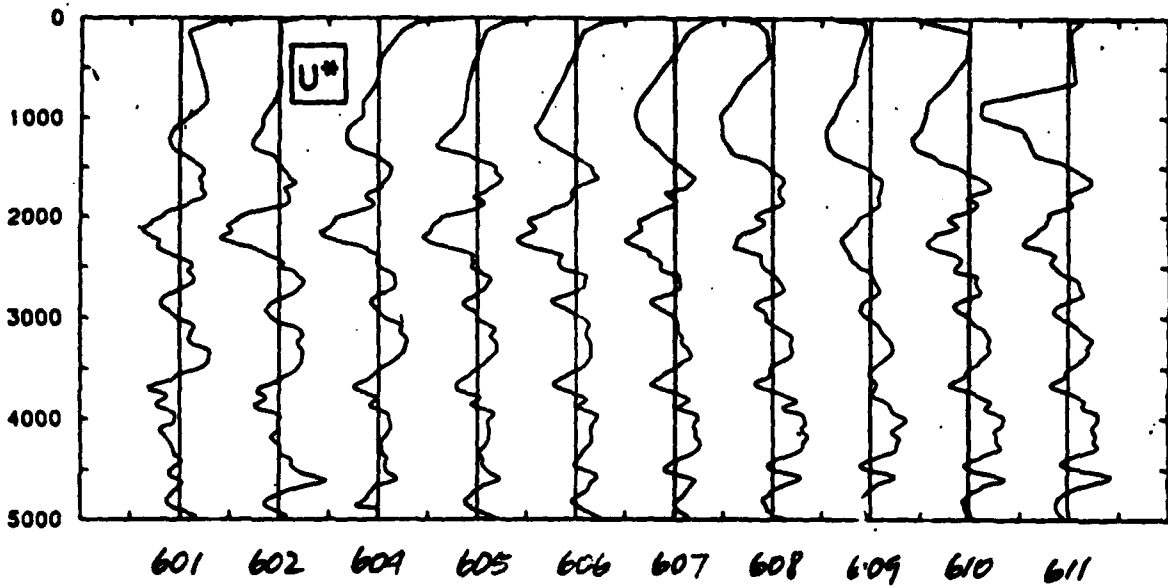
V\*

NET 5

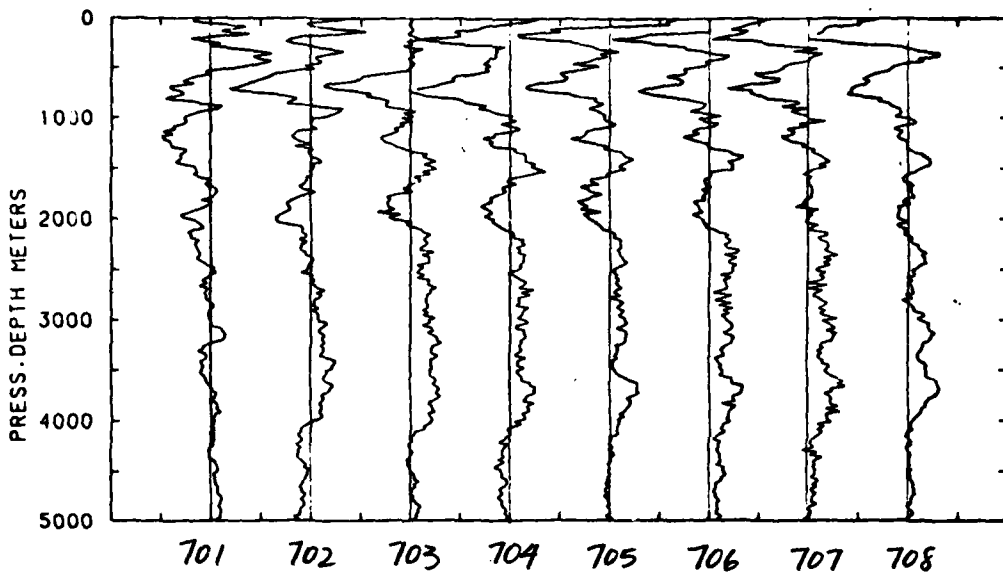
0°, 50° 30' E



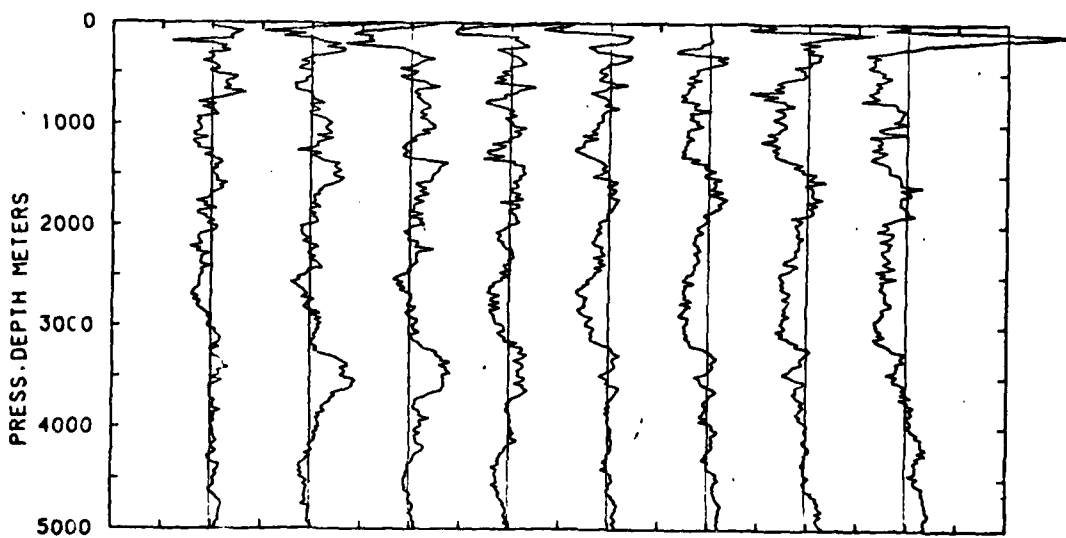
NET 6  
0°, 53°E



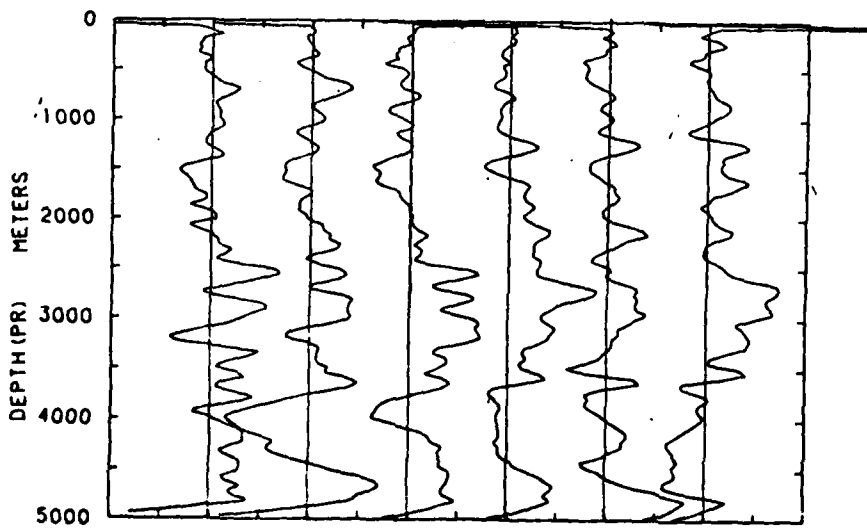
NET 6  
0°, 53°E



U



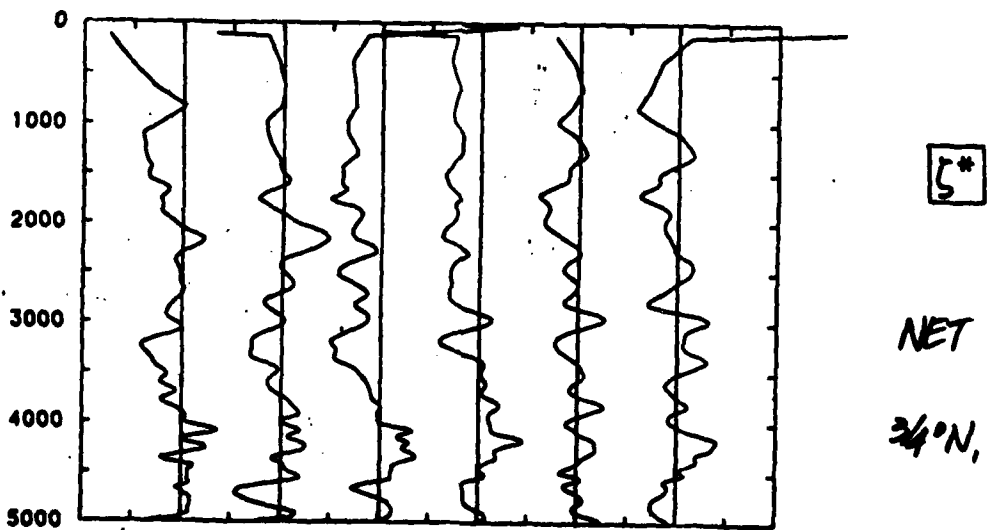
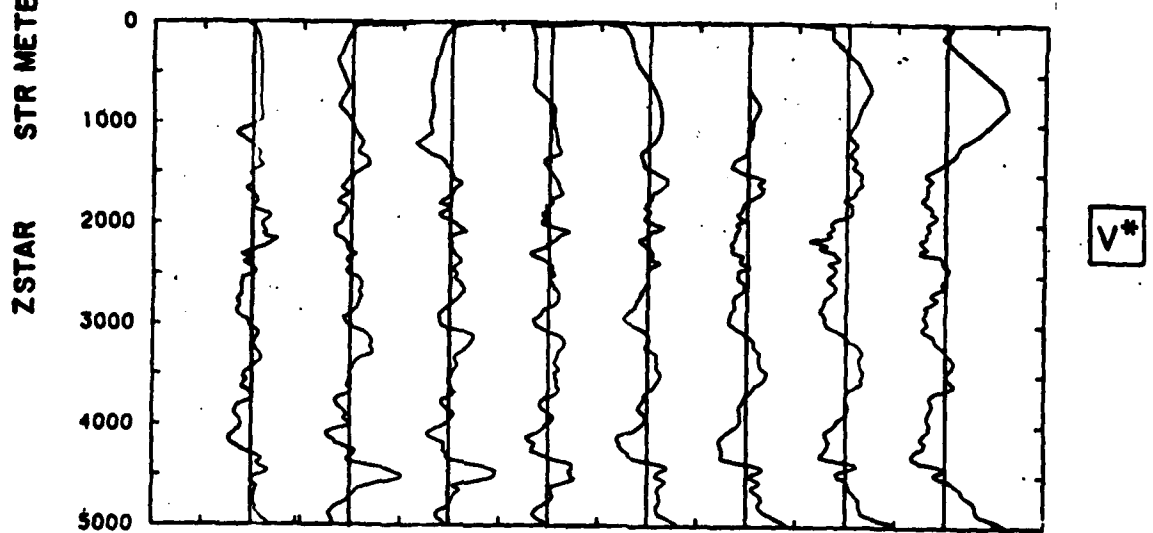
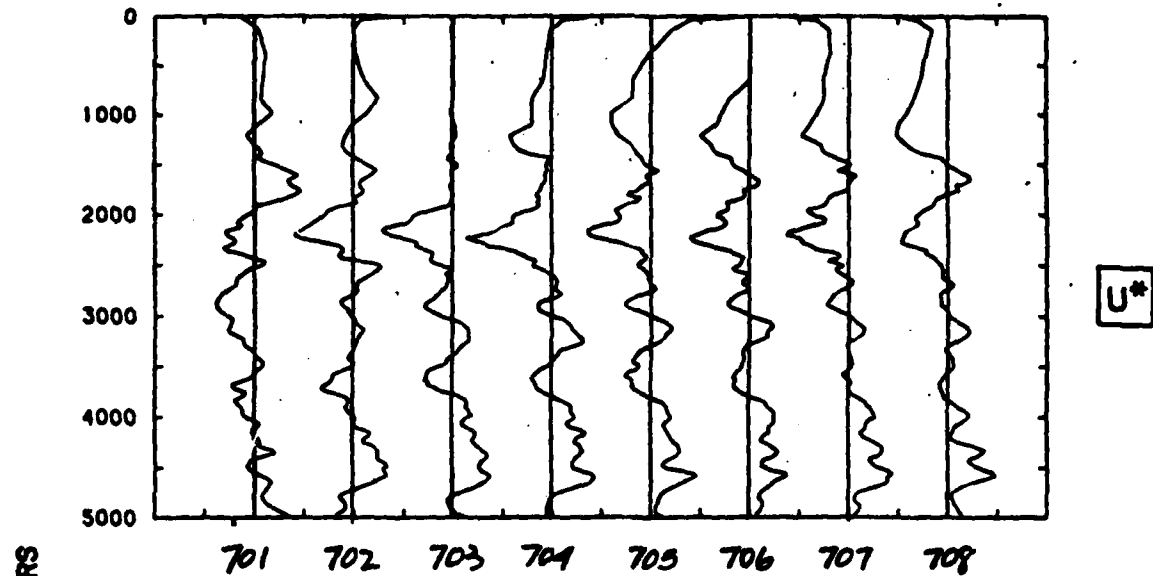
V



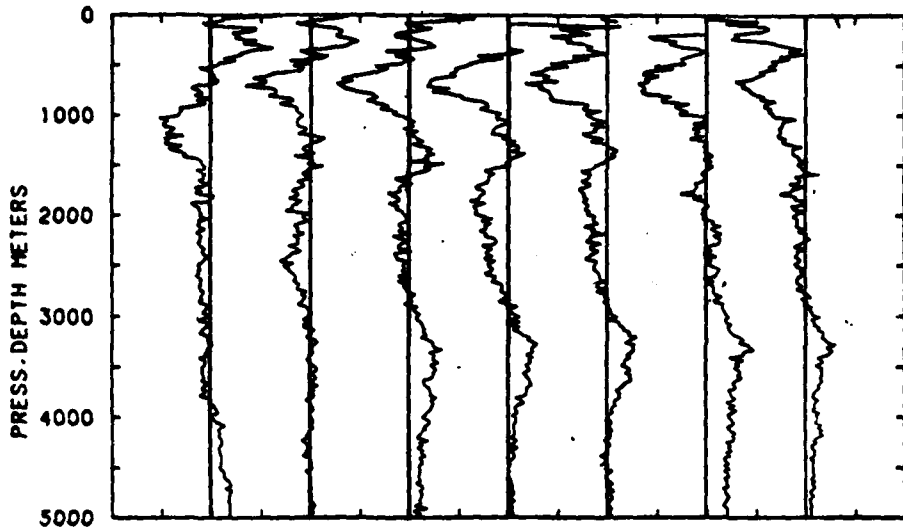
S

NET 7

34° N, 53° E

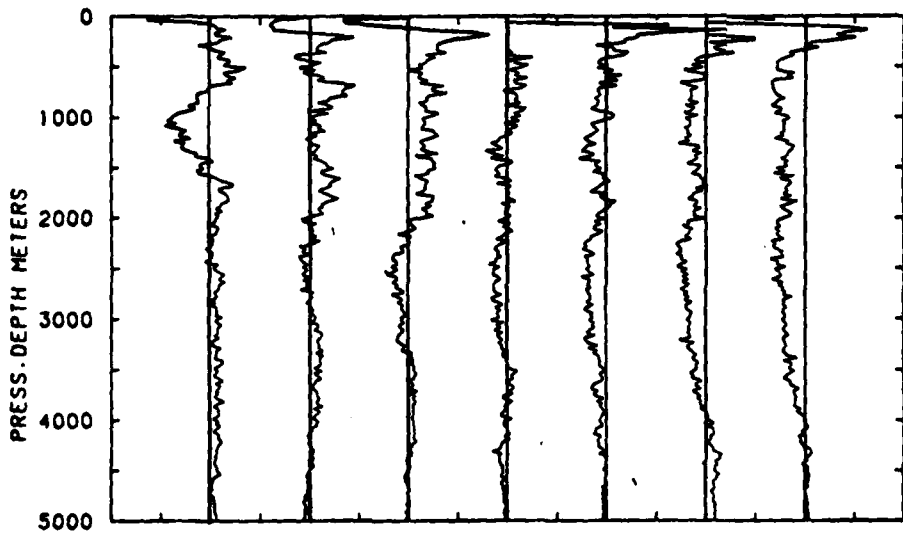


NET 7  
34°N, 53°E

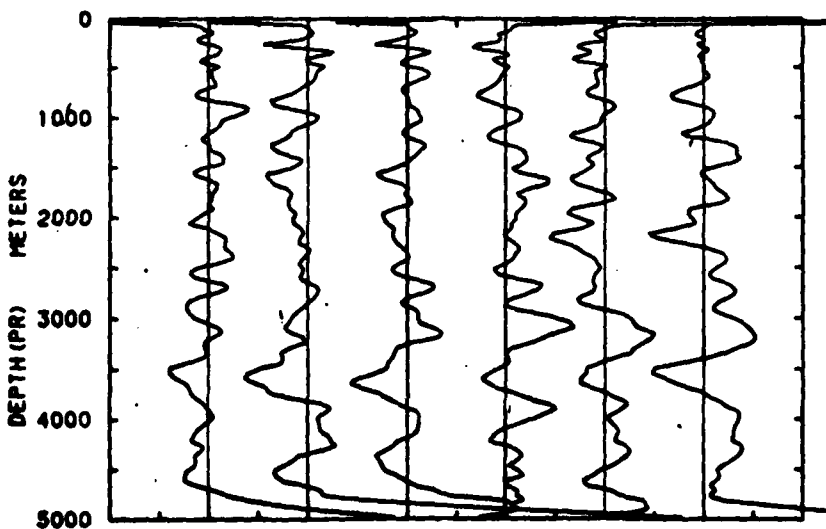


801 802 803 804 805 806 807

U



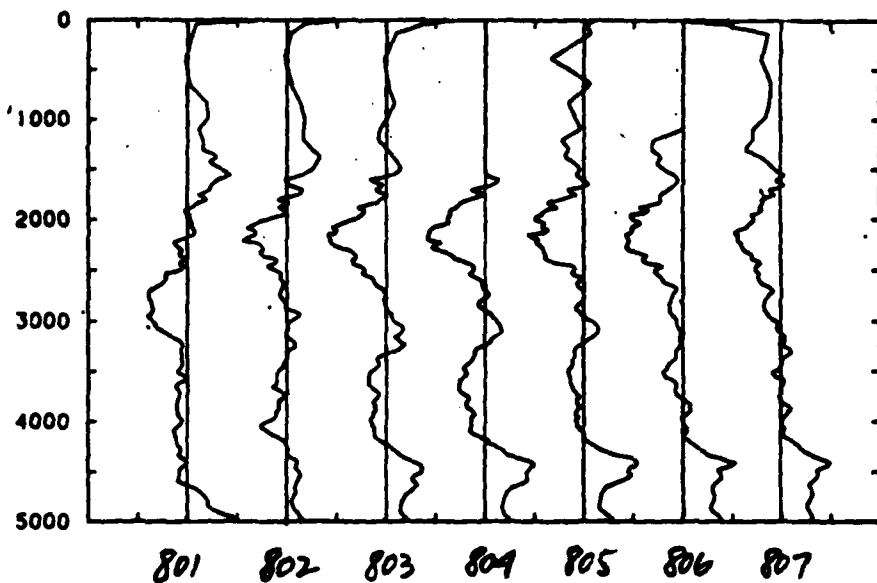
V



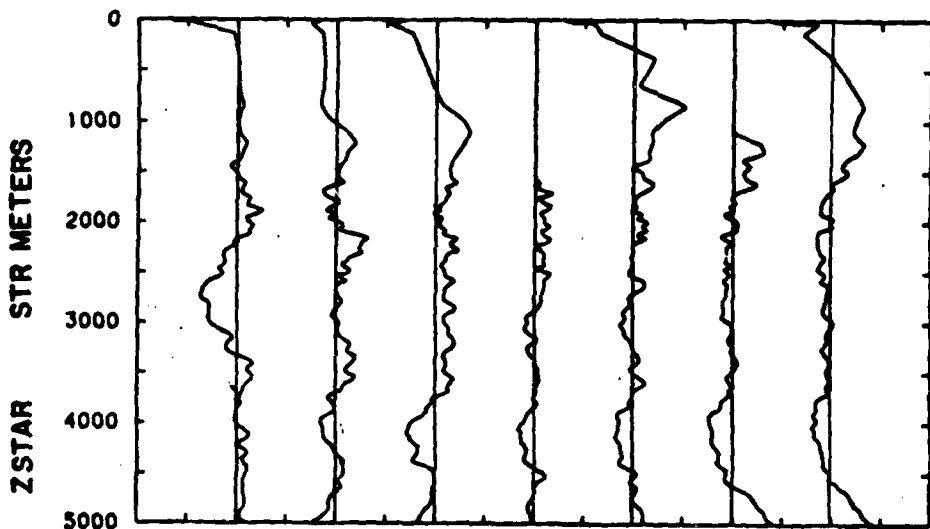
S

NET 8  
1 1/2° N, 53° E

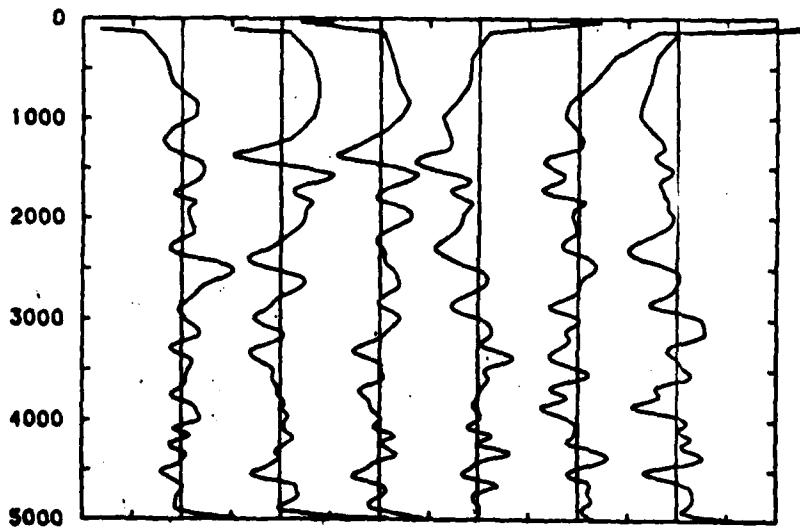




U\*



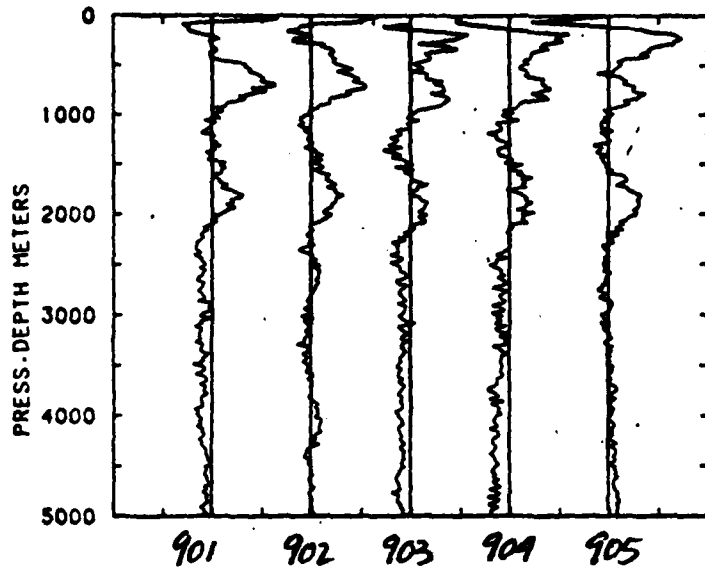
V\*



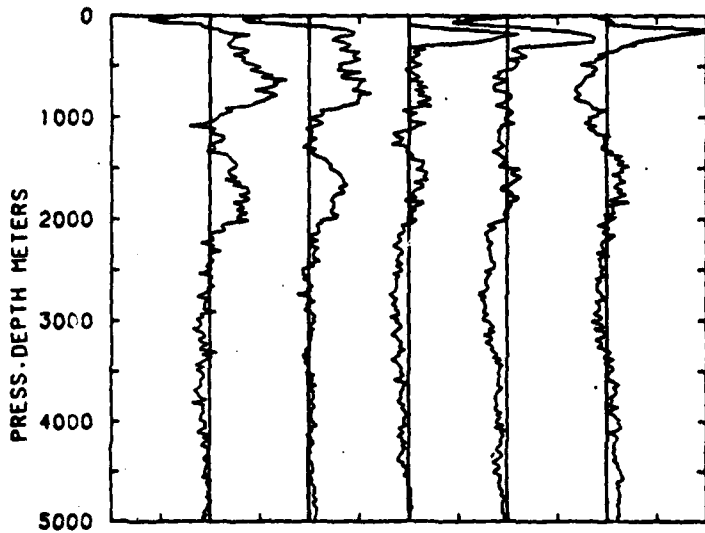
S\*

NET 8

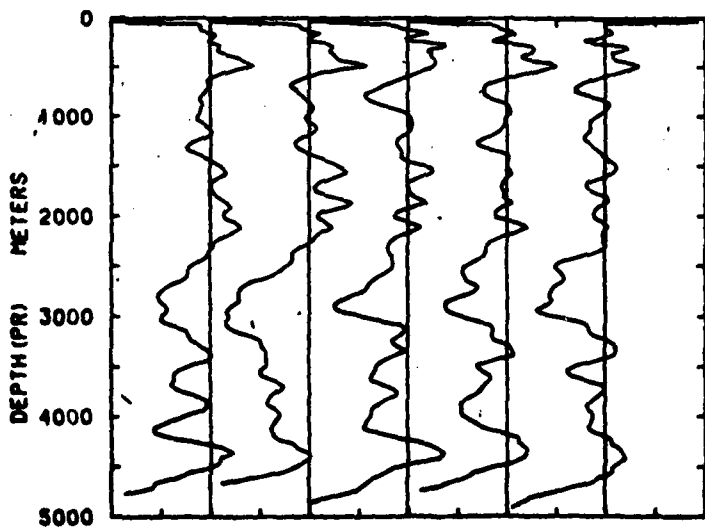
11/2°N, 53°E



U



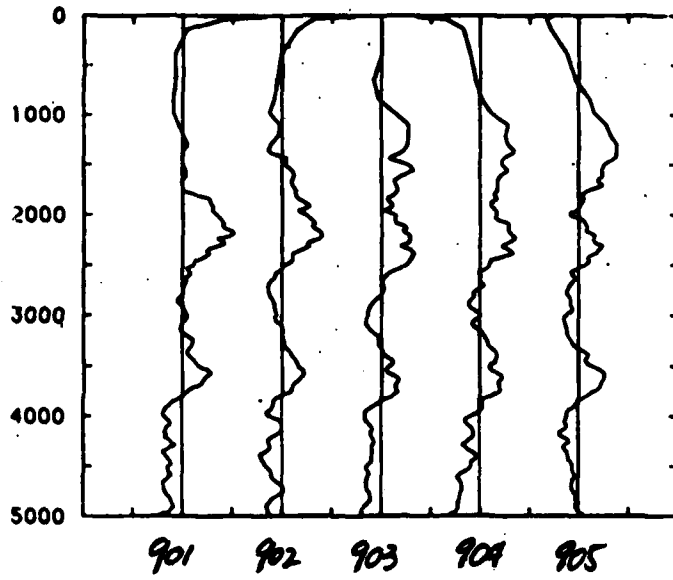
V



S

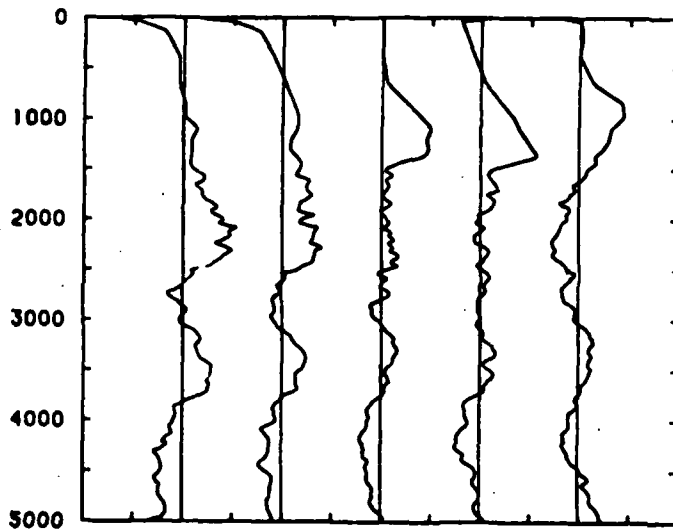
NET 9

3°N, 53°E

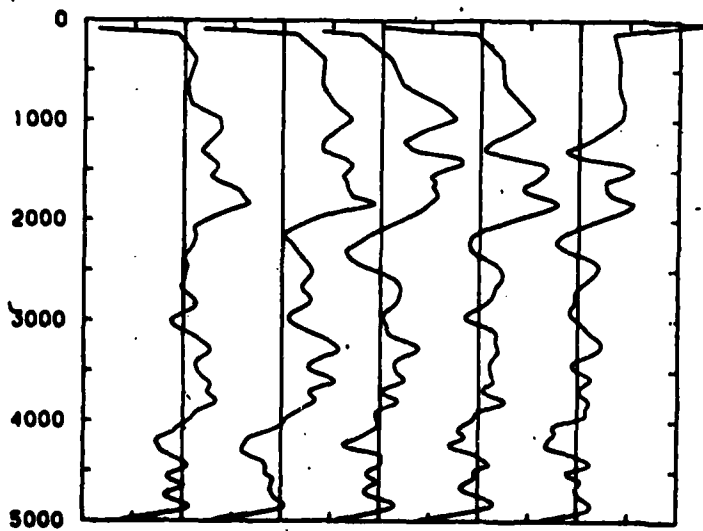


U\*

ZSTAR  
STR METERS



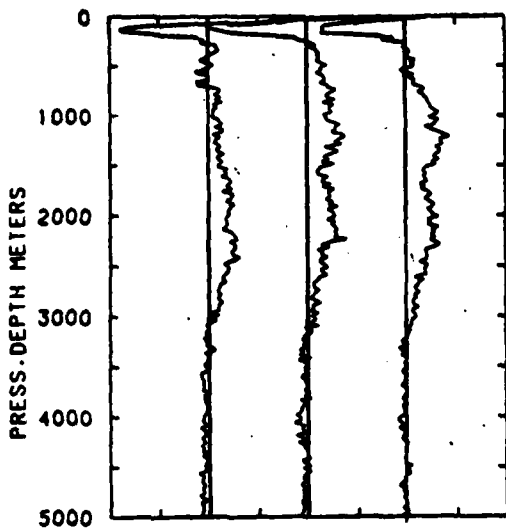
V\*



S\*

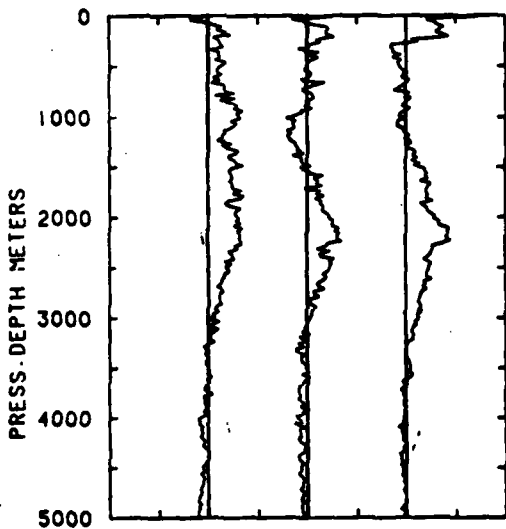
NET 9

3° N, 53° E

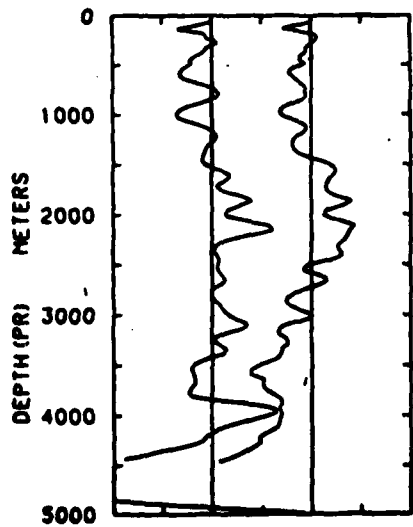


1001 1002 1003

U



V

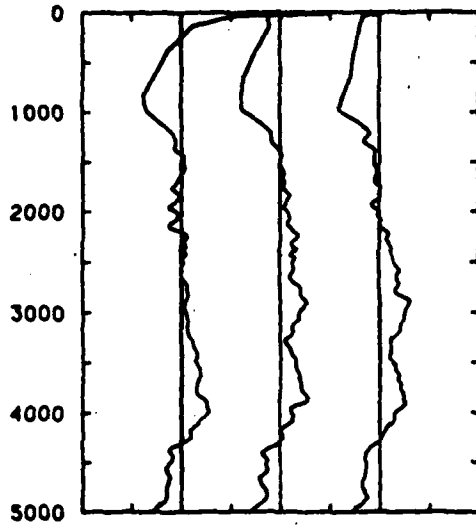


S

NET 10

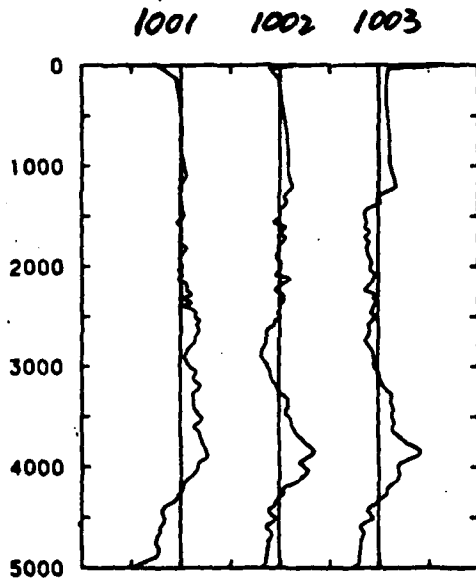
5°N, 53°E

150

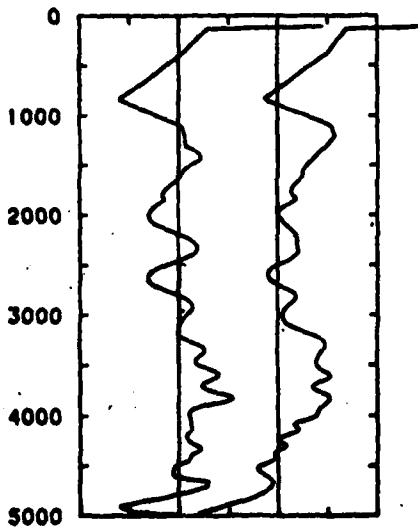


$U^*$

ZSTAR STR METERS



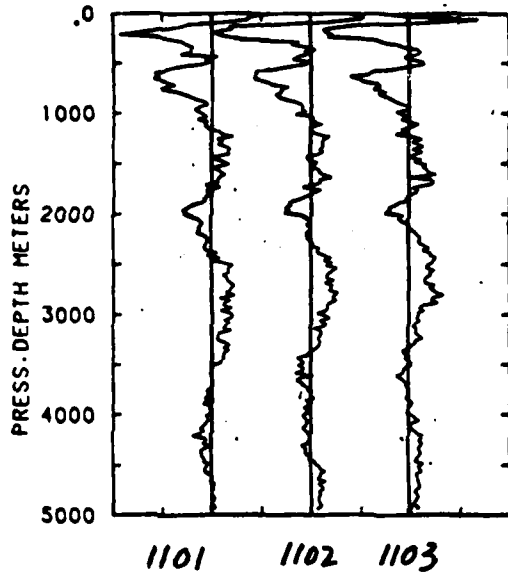
$V^*$



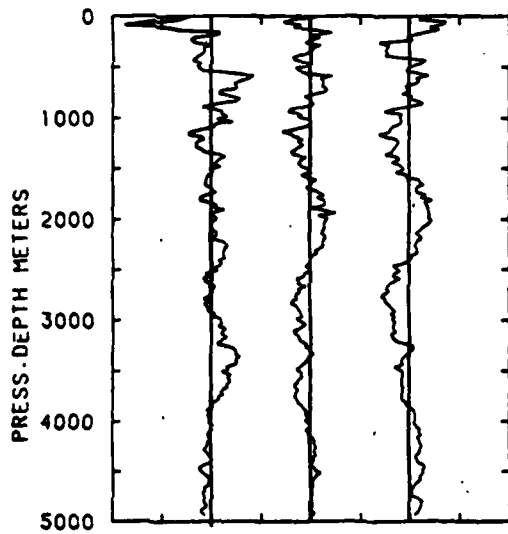
$S^*$

NET 10

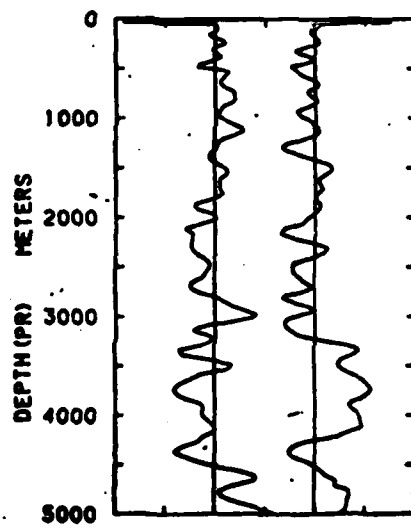
5°N, 53°E



U



V

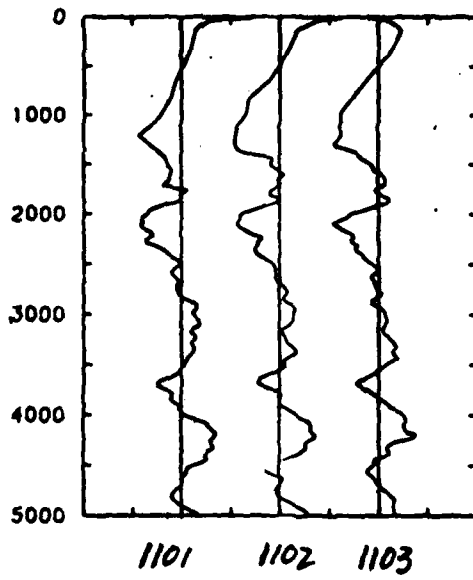


S

NET 11

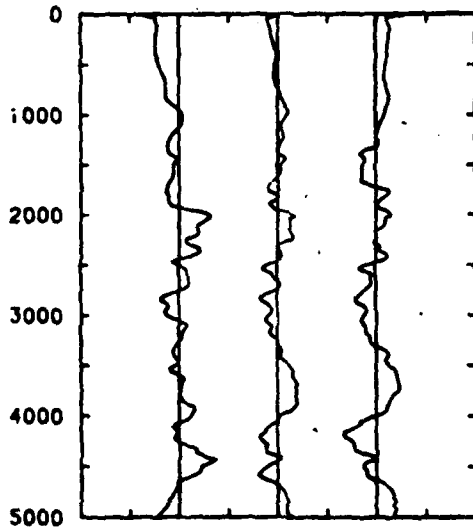
3/4°S, 53°E

152

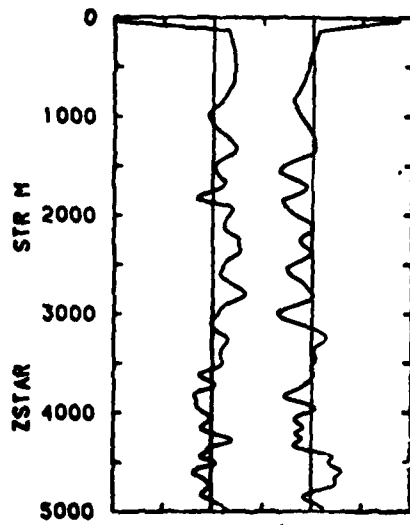


U\*

ZSTAR STR METERS



V\*



S\*

NET 11

$3/4^{\circ}S, 53^{\circ}E$

## APPENDIX C

Tables of Coherence Pairs  
At Each Latitude

Table 1. No wavenumber averaging

- a)  $u^*v$  [all profiles]
- b)  $\int^*u$  [subset for which vertical
- c)  $\int^*v$  displacement is available.]

Table 2. Averaged over two adjacent wavenumber bands

- a)  $u^*v$
- b)  $\int^*u$
- c)  $\int^*v$



TABLE C-1a

 $u \star v$ 

$\lambda_z$	<u>3/4°S</u>	<u>0°</u>	<u>3/4°N</u>	<u>1.5°N</u>	<u>3°N</u>	<u>5°N</u>
	<u>Coh. (Phase)</u>					
3600		.75(-40)			.76(-11)	
1800			.65(-34±42)		.74(37)	.89(-6)
1200		.84(166±22)	.75(-134±30)		.88(5)	.94(17)
900			.69(-28±37)	.76(-23)		.84(-34)
720		.63(57±45)	.75(34±30)			
600	None		.74(-54±31)			
514						
450						
400		.83(-133±23)	.71(-88±35)			
360						
327					.76(110)	
300		.60(119±50)				
277		.58(164±54)			.74(109)	
257						
240			.60(-34±50)			
225						
212						
200						
189						
180			.65(-13±42)			
171						
164						

TABLE C-1b

 $J^*u$ 

$\lambda_z$	<u>3/4°S</u>	<u>0°</u>	<u>3/4°N</u>	<u>1.5°N</u>	<u>3°N</u>	<u>5°N</u>
	<u>Coh. (Phase)</u>					
3600					.74(8)	.99(38)
1800			.82(-90±31)		.94(-43±17)	
1200					.74(178±48)	
900		.90(-148±23)	.72(-122±44)			
720		.89(-129±25)	.92(-173)	.79(134±33)	.76(151±44)	
600				.69(-56±48)		
514						.98(-54)
450						
400	1.00(168)		.79(-96±33)		.76(-81±44)	
360	.98(-152)		.77(-120±36)			
327						
300			.83(-114±28)			
277	.99(159)	.82(-131±35)		.77(-56±36)		
257						
240						
225			.87(-89±24)			
212						
200		.85(-143±30)				
189						
180						
171					.73(50)	
164		.84(-130±32)		.71(167)		

TABLE C-1c

 $J^*v$ 

$\lambda_z$	<u>3/4°S</u>	<u>0°</u>	<u>3/4°N</u>	<u>1.5°N</u>	<u>3°N</u>	<u>5°N</u>
	Coh. (Phase)					
3600	.98(109)					
1800						
1200					.82(-9±35)	
900			.70(-146±46)			
720		.80(-71±38)	.81(-130±31)			
600						
514						
450						
400			.84(-161±27)			
360						.98(123)
327						
300			.76(46±36)			
277						
257						
240						
225						
212		.76(-32±44)				
200			.70(-22±46)			
189				.70(28)		
180		.87(-5±27)				
171		.81(-102±36)				.94(-136)
164						

TABLE C-2. Coherence Pairs At Each Latitude,  
Averaged Over Two Wavenumber Bands.

$\lambda_z$	<u>3/4°S</u>	<u>0°</u>	<u>3/4°N</u>	<u>1.5°N</u>	<u>3°N</u>	<u>5°N</u>
	<u>Coh.(Phase)</u>		<u>J*u</u>			
1800			.52 (-52)		.72(-36)	
900		.84(-142)	.61(-141)			
600			.63(-169)		.63(134)	
450			.50(-106)			
360	.85(-173)		.71(-114)			None
300	.81(169)					
257		.57(-139)				
225			.54(-91)			
200		.59(-163)				
180						
164		.67(-140)		.50(166)		
			<u>J*v</u>			
1800						
900			.57(-150)		.69(-7)	
600						
450		.53(146)				
360	None			None		None
300						
257						
225						
200						
180						
164						
			<u>u*v</u>			
1800				.50(-105)	.76(19)	
900					.76(-11)	
600						
450	None	.55(58)	.56(2)			None
360					.65(93)	
300					.66(98)	
257						
225						
200						
180			.5 (-31)			
164						

## REFERENCES

- Bell, T. H., Jr. (1974). Processing vertical internal wave spectra. J. Phys. Oceanogr., 4, 669-670.
- Desaubies, Y. (1976). Analytical representation of internal wave spectra. J. Phys. Oceanogr., 6, 976-981.
- Eriksen, C. C. (1981). Deep Currents and their interpretation as equatorial waves in the Western Pacific Ocean. J. Phys. Oceanogr., 11, 48-70.
- Eriksen, C. C. (1982). Geostrophic equatorial deep jets. (to appear in J. Mar. Res.)
- Fofonoff, N. P. (1969). Spectral characteristics of internal waves in the ocean, Deep-Sea Res., Suppl to 16, 58-71.
- Gould, W. J., W. J. Schmitz Jr., and C. Wunsch (1974). Preliminary field results for a Mid-ocean Dynamics Experiment (MODE-0). Deep-Sea Res., 21, 911-931.
- Hayes, S. P. (1975). Preliminary measurements of the time-lagged coherence of vertical temperature profiles, J. Geophys. Res., 80, 307-311.
- Hayes, S. P. (1981). Vertical finestructure observations in the eastern equatorial Pacific. J. Geophys. Res., 86, 10983-10999.
- Hendricks, P. and M. Rodenbusch (1981). Interpretation of velocity profiles measured by freely sinking probes. Deep-Sea Res., 28A, 1199-1213.

- Knox, R. A. (1976). Results of a long series of measurements of Indian Ocean equatorial currents near Addu Atoll. Deep-Sea Res., 23, 211-221.
- Koopmans, L. H. (1974). The Spectral Analysis of Time Series, Academic Press, 366 pp.
- Leetmaa, A., and P. F. Spain (1981). Results from a velocity transect along the equator from 125 to 159°W. J. Phys. Oceanogr., 11, 1030-1033.
- Luyten, J. R. (1982). Equatorial current measurements, I. Moored observations. J. Mar. Res., in press.
- Luyten, J. R., M. Fieux and J. Gonella (1980). Equatorial currents in the western Indian Ocean. Science, 209 600-603.
- Luyten, J. R., G. Needell and J. Thomson (1982). An acoustic dropsonde - design, performance and evaluation. Deep-Sea Res., in press.
- Luyten, J. R., and D. Roemmich (1982). Equatorial currents at the semi-annual period in the Indian Ocean. J. Phys. Oceanogr., in press.
- Luyten, J. R., and J. C. Swallow (1976). Equatorial undercurrents, Deep-Sea Res., 23, 1005-1007.
- McPhaden, M. J. (1982). Variability in the central equatorial Indian Ocean. Part I. Ocean dynamics. (to appear in J. Phys. Oceanogr.)
- McPhaden M. J., and R. A. Knox (1979). Equatorial Kelvin and inertio-gravity waves in zonal shear flow. J. Phys. Oceanogr., 9, 263-277.
- Munk, D. W., and N. Phillips (1968). Coherence and band structure of inertial motion in the sea. Rev. Geophys., 6, 447-472.

- Munk, W. H., F. E. Snodgrass and M. J. Tucker (1959). Spectra of low-frequency ocean waves. Bull. Scripps Inst. Oc., 7, 283-362.
- Philander, S. G. H. (1978). Forced oceanic waves. Rev. Geophys. Space Phys., 16, 15-46.
- Philander, S. G. H. (1979). Equatorial waves in the presence of the equatorial undercurrent. J. Phys. Oceanogr., 9, 254-262.
- Rual, P. (1969). Courants equatoriaux profonds. Deep-Sea Res., 16, 387-391.
- Spencer, A. (1979). A compilation of moored current meter data, White Horse profiles and associated oceanographic observations, Volume XX (Rise Array, 1974). W.H.O.I. Reference No. 79-56.
- Spencer, A., K. O'Neill and J. R. Luyten (1980). A compilation of moored current meter data, White Horse profiles and associated oceanographic observations, Vol. XXIV (Indian Ocean array, 1976), W.H.O.I. Reference No. 80-41, 46 pp.
- Wunsch, C. (1977). Response of an equatorial ocean to a periodic monsoon, J. Phys. Oceanogr., 7, 497-511.

## VITA

Kathleen O'Neill was born Kathleen Barber on November 20, 1946. She graduated from Manhattanville College in 1967 with a B.A. in economics. After a two years of graduate study in Latin American economic development at the University of North Carolina at Chapel Hill, she worked for six years in the data processing field, progressing from systems programmer through senior systems analyst. Using a leave of absence, she enrolled as a special student in the Earth and Planetary Sciences Department at the Johns Hopkins University in October, 1975. She was accepted as a regular student in the physical oceanography section the following summer. After spending the summer of 1977 at Woods Hole working with the INDEX-76 data, she received an M.A. in physical oceanography from Johns Hopkins in May, 1978. She became a non-resident graduate student at Johns Hopkins and returned to Woods Hole in June, 1978, to research and write this dissertation.



MANDATORY DISTRIBUTION LIST

FOR UNCLASSIFIED TECHNICAL REPORTS, REPRINTS, AND FINAL REPORTS  
PUBLISHED BY OCEANOGRAPHIC CONTRACTORS  
OF THE OCEAN SCIENCE AND TECHNOLOGY DIVISION  
OF THE OFFICE OF NAVAL RESEARCH

(REVISED NOVEMBER 1978)

- 1 Deputy Under Secretary of Defense  
(Research and Advanced Technology)  
Military Assistant for Environmental Science  
Room 3D129  
Washington, D.C. 20301
- Office of Naval Research  
800 North Quincy Street  
Arlington, VA 22217
- 3 ATTN: Code 483  
1 ATTN: Code 460  
2 ATTN: 102B
- 1 CDR Joe Spigai, (USN)  
ONR Representative  
Woods Hole Oceanographic Inst.  
Woods Hole, MA 02543
- Commanding Officer  
Naval Research Laboratory  
Washington, D.C. 20375
- 6 ATTN: Library, Code 2627
- 12 Defense Technical Information Center  
Cameron Station  
Alexandria, VA 22314  
ATTN: DCA
- Commander  
Naval Oceanographic Office  
NSTL Station  
Bay St. Louis, MS 39522
- 1 ATTN: Code 8100  
1 ATTN: Code 6000  
1 ATTN: Code 3300
- 1 NODC/NOAA  
Code D781  
Wisconsin Avenue, N.W.  
Washington, D.C. 20235
- 1 Mr. Michael H. Kelly  
Administrative Contracting Officer  
Department of the Navy  
Office of Naval Research  
Eastern/Central Regional Office  
Building 114, Section D  
666 Summer Street  
Boston, MA 02210

